



Intermediate Temperature Stress Rupture of Woven SiC Fiber, BN Interphase, SiC Matrix Composites in Air

Gregory N. Morscher
Case Western Reserve University, Cleveland, Ohio

The NASA STI Program Office . . . in Profile

Since its founding, NASA has been dedicated to the advancement of aeronautics and space science. The NASA Scientific and Technical Information (STI) Program Office plays a key part in helping NASA maintain this important role.

The NASA STI Program Office is operated by Langley Research Center, the Lead Center for NASA's scientific and technical information. The NASA STI Program Office provides access to the NASA STI Database, the largest collection of aeronautical and space science STI in the world. The Program Office is also NASA's institutional mechanism for disseminating the results of its research and development activities. These results are published by NASA in the NASA STI Report Series, which includes the following report types:

- **TECHNICAL PUBLICATION.** Reports of completed research or a major significant phase of research that present the results of NASA programs and include extensive data or theoretical analysis. Includes compilations of significant scientific and technical data and information deemed to be of continuing reference value. NASA's counterpart of peer-reviewed formal professional papers but has less stringent limitations on manuscript length and extent of graphic presentations.
- **TECHNICAL MEMORANDUM.** Scientific and technical findings that are preliminary or of specialized interest, e.g., quick release reports, working papers, and bibliographies that contain minimal annotation. Does not contain extensive analysis.
- **CONTRACTOR REPORT.** Scientific and technical findings by NASA-sponsored contractors and grantees.

- **CONFERENCE PUBLICATION.** Collected papers from scientific and technical conferences, symposia, seminars, or other meetings sponsored or cosponsored by NASA.
- **SPECIAL PUBLICATION.** Scientific, technical, or historical information from NASA programs, projects, and missions, often concerned with subjects having substantial public interest.
- **TECHNICAL TRANSLATION.** English-language translations of foreign scientific and technical material pertinent to NASA's mission.

Specialized services that complement the STI Program Office's diverse offerings include creating custom thesauri, building customized data bases, organizing and publishing research results . . . even providing videos.

For more information about the NASA STI Program Office, see the following:

- Access the NASA STI Program Home Page at <http://www.sti.nasa.gov>
- E-mail your question via the Internet to help@sti.nasa.gov
- Fax your question to the NASA Access Help Desk at (301) 621-0134
- Telephone the NASA Access Help Desk at (301) 621-0390
- Write to:
NASA Access Help Desk
NASA Center for AeroSpace Information
7121 Standard Drive
Hanover, MD 21076



Intermediate Temperature Stress Rupture of Woven SiC Fiber, BN Interphase, SiC Matrix Composites in Air

Gregory N. Morscher
Case Western Reserve University, Cleveland, Ohio

Prepared under Contract NCC3-404

National Aeronautics and
Space Administration

Glenn Research Center

Trade names or manufacturers' names are used in this report for identification only. This usage does not constitute an official endorsement, either expressed or implied, by the National Aeronautics and Space Administration.

Available from

NASA Center for Aerospace Information
7121 Standard Drive
Hanover, MD 21076
Price Code: A07

National Technical Information Service
5285 Port Royal Road
Springfield, VA 22100
Price Code: A07

TABLE OF CONTENTS

1	Introduction 1	1
1.1	How CMC's Embrittle Under Stressed/Oxidation Conditions	1
1.1.1	Time Dependent Failure of Fibers	1
1.1.2	The SiC/C/SiC System.....	3
1.1.3	The SiC/BN/SiC System.....	6
1.2	Damage Accumulation in CMC's.....	11
1.2.1	Matrix Cracking: The Non-Linear Stress Strain Curve	11
1.2.2	Quantifying Damage Accumulation	13
1.2.3	Monitoring Damage Accumulation	16
1.3	Modeling Composite Rupture.....	20
1.4	Works Cited	22
2	Experimental Procedure.....	29
2.1	Mechanical Testing and Acoustic Emission	29
2.2	Matrix Crack Determination	31
2.3	Scanning Electron Microscopy	31
2.4	Works Cited	31
3	Results.....	33
3.1	Melt-Infiltrated Composite Rupture	33
3.1.1	Stress-Rupture Data	33
3.1.2	Acoustic Emission Data and Matrix Crack Spacing.....	36
3.1.3	Microscopy of Composite Fracture Surfaces.....	42
3.1.4	EDS Analysis	45
3.1.5	Fiber Fractography.....	47
3.1.6	Retained Strength of Rupture Specimens Which Had Not Failed.....	51
3.2	Chemical Vapor Infiltration Composite Rupture.....	54
3.2.1	Stress-Rupture Data	54
3.2.2	Acoustic Emission Data.....	56
3.2.3	Microscopy of Composite Fracture Surfaces	56
3.3	Works Cited	62
4	Modeling Composite Rupture.....	63
4.1	Factors Controlling Rupture	63
4.1.1	Oxidation of the BN Interphase	63
4.1.2	Fiber Weakening.....	65
4.1.3	Matrix Cracking.....	66

4.2	Fiber Failure Considerations.....	66
4.3	Modeling Rupture Behavior with Through Thickness Cracks	70
4.3.1	MI Matrix Composite Rupture.....	71
4.3.2	CVI Matrix Composite Rupture.....	75
4.3.3	CVI Matrix Minicomposite Rupture.....	78
4.4	Modelling With Progressive Non-Bridging Crack Propagation.....	79
4.5	Effect of Input Variables on Model	82
4.5.1	The Effect of σ_0	82
4.5.2	The Effect of Precracking (Crack Density)	84
4.6	Works Cited	85
5	Discussion.....	87
5.1	Matrix Cracking and Crack Opening During Rupture Testing.....	87
5.2	Modeling Stress-Rupture and the Role of Stress-Concentrators	90
5.2.1	Individual Fiber Failure and Stress Concentrators.....	90
5.2.2	The Assumptions	92
5.3	Implications for Woven SiC/SiC Composites	93
5.4	Implications for Oxide Composite Systems	96
5.5	Works Cited	96
6	Conclusions.....	99
Appendix A: Modal Acoustic Emission – AE Energy as a Means to Quantify Transverse Matrix Cracking		101
A.1	Matrix Cracking at Room (Low) Temperatures	101
A.2	Matrix Cracking at Elevated Temperatures	106
A.3	Works Cited	108
Appendix B: The Likelihood for Fiber Rupture Away from a Matrix Crack.....		109
B.1	Works Cited.....	111
Bibliography		113

1.0 INTRODUCTION

Continuous fiber-reinforced ceramic matrix composites (CMC's) have been an area of intense study for nearly twenty years^[1-4]. The CMC is made up of three principal constituents: fiber, interphase, and matrix. CMC's with all oxide constituents, nonoxide fibers reinforcing oxide matrices, and nonoxide fibers reinforcing nonoxide matrices have all been fabricated. The attraction of CMC's is that they offer high strength and high toughness combined with low density, high thermal conductivity (possibly), erosion resistance and refractoriness. However, due to the expense of these composites, their niche in the marketplace has been envisioned for high risk, high payoff applications such as aircraft engine combustor liners^[5] to replace current superalloy technology.

There are two major requirements of a CMC system which enable it to perform effectively, (1) strong, creep-resistant fibers and (2) an interphase (or interface) which is weak enough to allow crack deflection and sliding and which can withstand the environmental conditions imposed by a given application. The matrix provides dimensional stability, environmental durability, thermal conductivity, and does carry some load. However, successful composites are expected to be capable of continued service even after the matrix begins to accumulate damage. Matrix cracking causes fibers to carry a larger fraction of applied loads in the cracked regions and enables access of the environment to the interphase and fibers. If fibers and/or interphases are susceptible, for example, to stressed-oxidation degradation, the onset of matrix cracking will ultimately limit the working range of a composite.

Therefore, the focus of this research was aimed at measuring how the combination of stress, temperature, and environment in oxidizing atmospheres affect the composite constituents and eventually lead to high temperature, time dependent failure and developing an understanding of the governing relationships. The composite system chosen for study consists of SiC fibers, BN interphase, and SiC matrix. This system ranks as one of the strongest and most creep-resistant CMC system. It has been produced in sufficient quantity and for long enough time that the processing yields a relatively consistent product. There is also a sizeable database on this family of materials.

1.1 How CMC's Embrittle Under Stressed-Oxidation Conditions

1.1.1 Time Dependent Failure of Fibers

Most CMC testing, in general, and for the SiC/SiC system in particular, has been performed on systems with "ceramic grade" NicalonTM fibers as the fiber reinforcement. More recent fiber development has yielded two additional SiC fiber-types, Hi-NicalonTM and SylramicTM, which are more stable at elevated temperatures. Table 1.1 lists some pertinent details and properties of these three SiC fiber-types.

The mechanical properties of a good composite will ultimately be dictated by the mechanical properties of the reinforcing fibers. For the long time applications envisioned for these types of materials, creep and rupture properties of the fibers are expected to limit composite performance^[10]. The tensile creep and rupture properties of the three SiC fiber types of interest have been well characterized^[11-13]. Some fiber properties are listed in Table 1.1 for the three fiber types. Yun and DiCarlo^[12-13] have summarized all of the time dependent failure data on a Larson-Miller type plot which combines time and temperature and it is reproduced as Figure 1.1. Note that the Sylramic fiber is more rupture resistant than Hi-Nicalon at lower temperatures and less rupture resistant at higher temperatures. The improved creep resistance of

Sylramic and Hi-Nicalon fibers over the Nicalon fibers is due in part to the lower oxygen content of these fibers (Table 1.1). Even when the time to failure is longer, the creep strain of Sylramic fibers for a given stress-time-temperature condition is actually less than that of Hi-Nicalon which in turn is less than that of Nicalon.

The shallow slope at lower temperatures of the fiber rupture curves in Figure 1.1 is indicative of a slow crack growth type of mechanism; whereas, the steeper slope at higher temperatures more likely corresponds to a creep-rupture type of mechanism^[14]. The benefit of this type of plot is that all of the rupture behavior can be plotted over the entire temperature range. This will allow a comparative approach when analyzing composite performance, as will be discussed more fully in later sections. Comparing the properties of the fibers to that of the composites helps to reveal, the time-temperature ranges where mechanical properties are controlled by the fiber properties themselves versus some other embrittlement mechanism.

Table 1.1: Fiber Properties, Composition and Microstructure.

SiC Fiber	Avg. Fiber Diam. (μm)	No. Fibers per tow	Composition (w/o)	Microstructure	Fiber Modulus (GPa)	Fiber Strength (GPa)
Nicalon ^a	14	500	Si(31), C(58), O(12) ^[6]	~ 2 nm SiC grains in Si-O-C "matrix" ^[8]	200	3.1
Hi-Nicalon ^a	13	500	Si(35.8), C(63.7), O(0.5) ^[6]	~ 5 nm SiC grains in C "matrix" ^[9]	280	2.8
Sylramic ^b	10	800	Si(66.6), C(28.5), O(0.8), B(2.3), Ti(2.1), N(0.4) ^[7]	30 to 100 nm β-SiC grains with some TiB ₂ grains ^[7]	380	2.8

^aNippon Carbon, Japan

^bDow Corning, Midland, MI

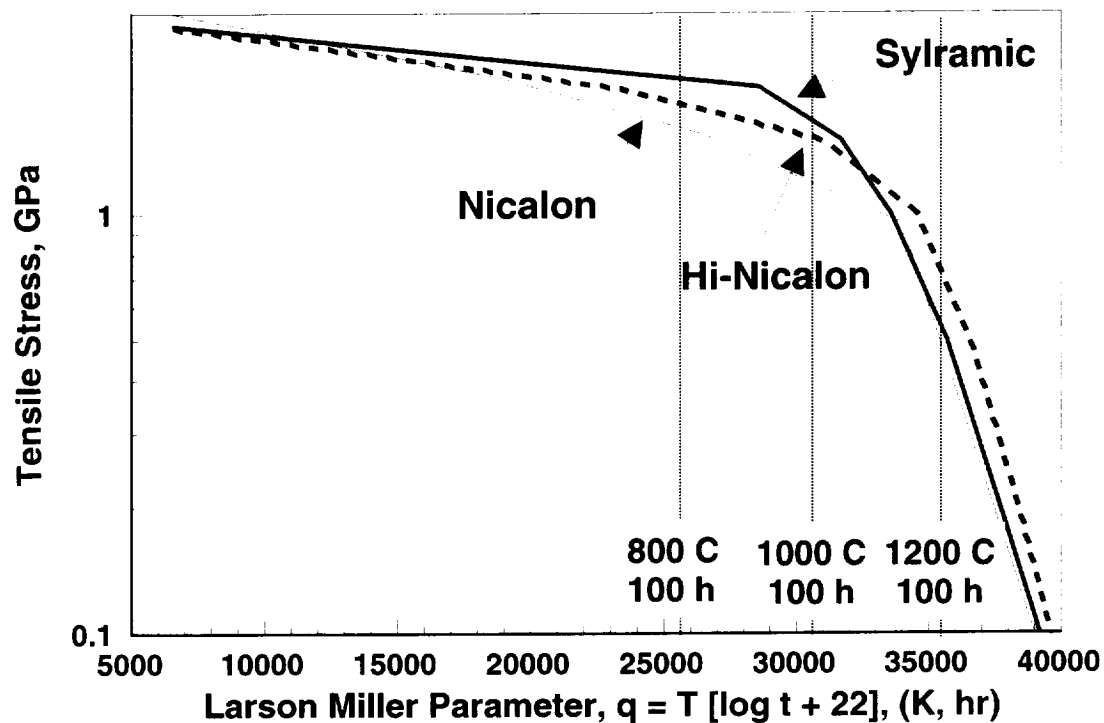


Figure 1.1: Larson Miller plot for the rupture properties of Hi-Nicalon and Sylramic fibers (from ref. 12 and 13).

1.1.2 The SiC/C/SiC System

Some rupture properties have been determined for composites of Nicalon fiber, with a carbon interphase and a CVI SiC matrix (Nic/C/SiC). For example, Heredia et al.^[15] performed stress rupture experiments in air at 800°C on 2D woven Nic/C/SiC composites and found a drastic reduction in rupture strength as a function of time. Analogous behavior was found for similar composites at 600 and 900°C by Lin et al.^[16], and at 700°C by Morscher^[17] for single tow minicomposites, at 425°C by Lara-Curzio^[18], at 950°C by Lara-Curzio^[19], and at 1000°C by Lipetzky et al.^[20]. Steyer et al.^[21] and Verilli et al.^[22] have also determined the stress rupture properties of a NiC/C/SiC which has an “enhanced” (B₄C-containing) CVI SiC matrix over similar temperature ranges. Most of the data for these studies are compiled in Figure 1.2 and on the Larson-Miller plot in Figure 1.3. In constructing this plot (Fig. 1.3), the stress on the fibers was determined by the composite stress divided by the volume fraction of fibers in the loading direction since failure is at the region immediately associated to a matrix crack. Such normalized data facilitates a direct comparison with single fiber rupture data (Fig. 1.3).

The data appear consistent with temperature, despite the fact that the tests performed by Lin et al.^[16] were in 4-pt flexure and the other tests were in tension. The lifetime of the flexure specimens must have been controlled by the behavior on the tensile face. It is clear from Figure 1.3 that the rupture behavior of these composites are far worse than would be expected for the as-produced fiber properties.

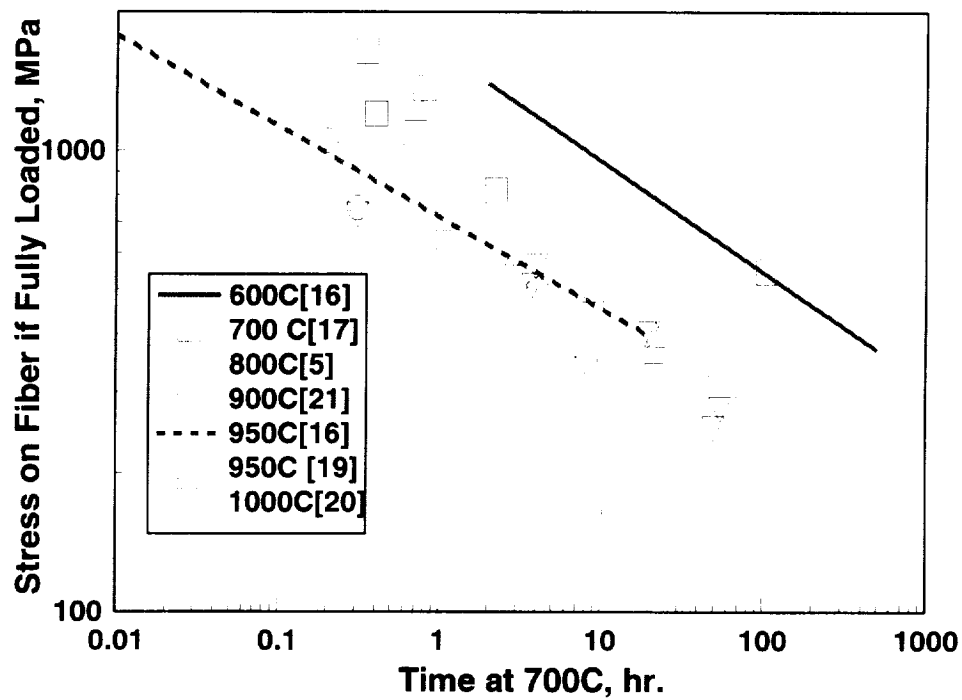


Figure 1.2: Stress rupture of Nic/C/SiC composites. Data from Lin et al. [16] are from 4-point flexure tests. The other data are from tensile tests.

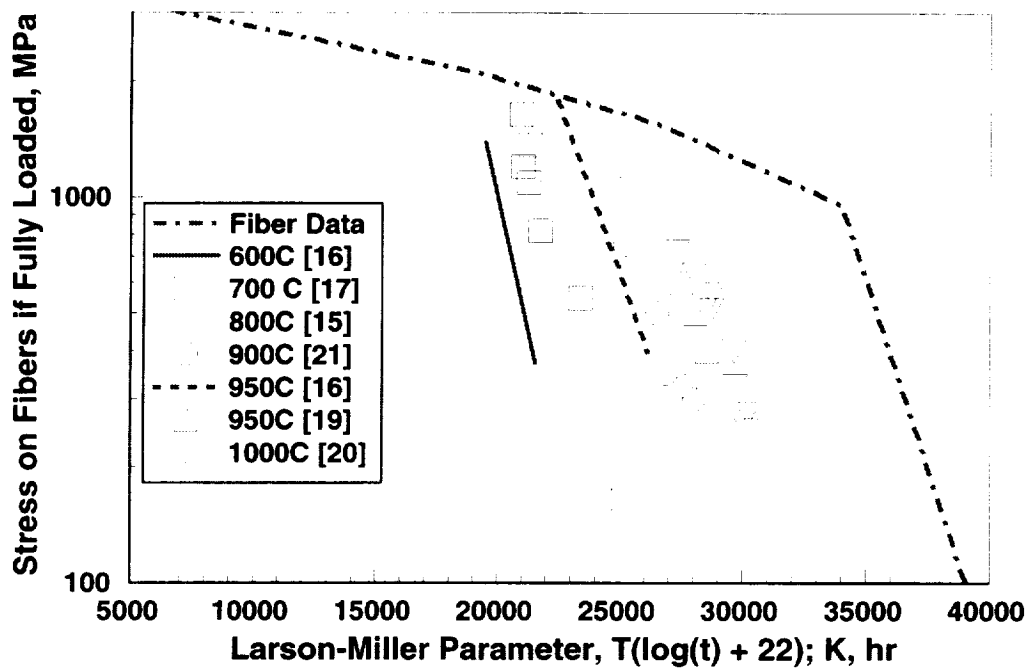


Figure 1.3: Larson-Miller plot for Nic/C/SiC data and as-produced Nicalon fiber data [12].

For all of these systems, the carbon interphase was oxidized and volatilized as CO or CO₂^[23-25] usually leaving a gap between the fiber and the matrix. The oxygen had access to the interphase via matrix cracks. An exception to this behavior was the “enhanced” SiC matrix^[21], where significant boron formation occurred in the matrix cracks and would sometimes fill in the gaps between fiber and matrix (especially for the outer bundles). From fracture mirror analysis of individual fibers on the minicomposite fracture surface, Morscher^[17] showed that the embrittlement phenomena of the single fiber tows was due to strength degradation of the fibers themselves. In other words, embrittlement was not due to a gage-length effect from carbon-interphase removal or strong bonding between the fibers and the matrix. Apparently, the change in the surface structure of the Nicalon fibers during composite processing resulted in a propensity to the creation of deleterious flaws when subsequently subjected to the stressed-oxidation condition.

Little work has been performed on SiC/C/SiC rupture behavior for Hi-Nicalon or Sylramic fiber reinforcement systems. Part of this is probably due to a growing lack of interest in C interphases, although it is mostly due to the relatively higher cost of these fibers compared to Nicalon. One study by Martinez-Fernandez and Morscher^[26] has determined the behavior of Hi-Nicalon, C interphase minicomposites for temperatures ranging from 700 to 1200°C in air. Figure 1.4 shows the Larson-Miller plot of stress rupture for these HN/C/SiC minicomposites. A minor amount of additional degradation occurs at 700°C for the HN/C/SiC minicomposites compared to the normal fiber degradation itself (the initial slope of the HN/SiC minicomposite is less than the fiber data). A greater amount of embrittlement occurs for longer times at 700°C and at higher temperatures. However, the degradation in composite rupture properties is not as severe as it is for Nic/C/SiC (Fig. 1.3). These fibers seem to be more stable to the CVI processing conditions, which apparently degraded the Nicalon fibers in Nic/C/SiC composites, which likely contributed to the increase in rupture resistance.

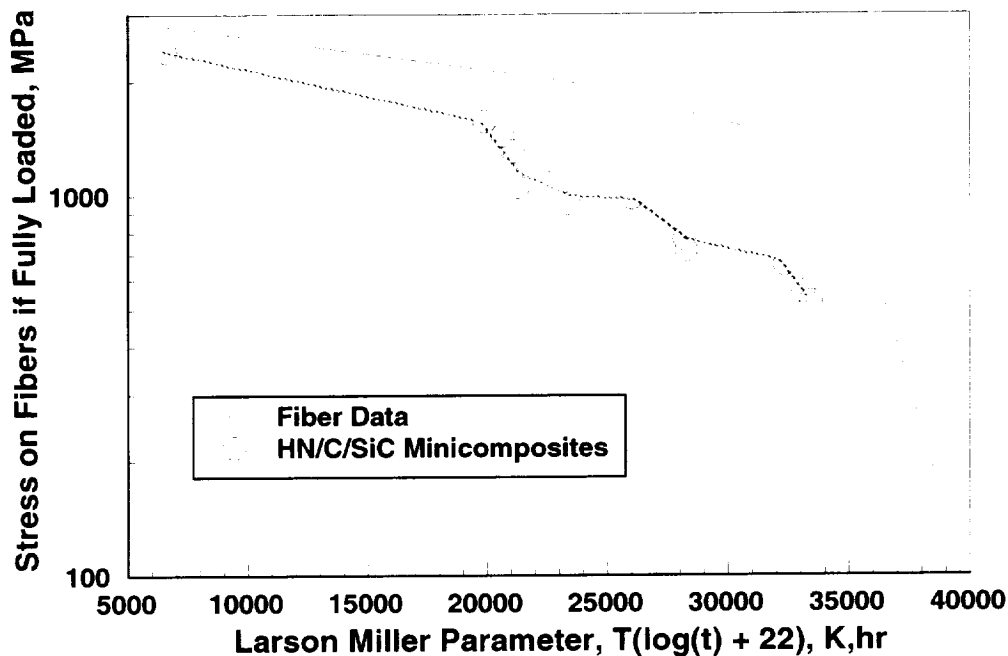


Figure 1.4: Larson Miller plot for HN/C/SiC minicomposite rupture and as-produced Hi-Nicalon fibers [26].

1.1.3 The SiC/BN/SiC System

BN is now considered the state of the art interface for SiC/SiC composites because it possesses similar debonding and sliding properties to C, yet it is more durable than C in oxidizing environments. To date, it appears, only a few studies have been published for Nic/BN/SiC^[17,27] and HN/BN/SiC^[17,28,29]. Morscher^[17,28] has determined the stress rupture behavior of Nic/BN and HN/BN CVI SiC matrix minicomposites in air between 600 and 1300°C. Morscher^[28] also determined the low-cycle fatigue behavior of HN/BN/SiC minicomposites. Some unpublished data has been made available from the High Speed Civil Transport Program* at NASA Glenn Research Center on HN/BN CVI SiC and MI SiC matrix woven composites^[29]. The stress-rupture data from these studies are compiled in Figures 1.5 and 1.6 for the Nic/BN/SiC and HN/BN/SiC minicomposite data respectively.

The Nic/BN and HN/BN SiC minicomposite rupture behavior is very similar to the as-produced fiber rupture behavior. There is little if any embrittlement up to 700°C for either system (the initial slope of the as-produced fiber data and minicomposite data is the same), i.e. the rupture properties of the minicomposite is controlled by the rupture properties of the fibers. This is true even though in specimens tested at 700°C the BN interphase was observed to have volatilized^[17,28].

At higher temperatures (~ 850 to 1050 °C), the minicomposite rupture data does decrease noticeably and some degree of embrittlement is evident, i.e. properties are degraded relative to the intrinsic rupture behavior of the fibers. Borosilicate glass formation occurred in this temperature range. When EDS analysis of the minicomposite fracture surface was performed, Si-O containing glass was observed to fuse many of the fibers together or at least locally "spot weld" the fibers to the matrix (Figure 1.7). Fracture mirrors always emanated from these fiber-fused regions of the individual fiber fracture surface. It was evident that minicomposite rupture properties in this regime were due to the combination of some fiber degradation and stress-concentrations placed on the fibers after the fibers were glued to the matrix^[30].

An interesting observation from this analysis was that no B could be detected, using EDS, in any of the glass formed at the fracture surface even though B was easily detected in BN. It is believed that B was leached out of the glass due to a reaction with water vapor resulting in a more viscous, higher SiO₂ content borosilicate** glass which eventually solidified at ~ 950 ± 100°C. Evidence for this has been shown by Jacobson et al^[31] for a borosilicate glass subjected to 900°C and water pressure less than 100 ppm. It is believed that this process takes less than two hours and is the reason why the most significant decrease in rupture properties for static and cyclic loads occurs between 1 and 2 hours (Figure 1.6). It should also be noted that the severe embrittlement due to low cycle fatigue for HN/BN/SiC minicomposites was not due to loss in fiber strength (Figure 1.6). Fracture mirror analysis of the fiber fracture surfaces showed that the average individual fiber strength corresponded to the as-produced rupture strength for the given time/temperature condition, about twice the stress corresponding to the applied load. The stress-concentration mechanism is considered to be much more severe for the externally changing load condition.

The High Speed Civil Transport (HSCT) Program was a program sponsored by NASA towards building a HSCT aircraft for the 21st century. A sub-element of this program towards engine development is entitled Enabling Propulsion Materials (EPM) which is a joint venture between NASA Glenn Research Center, Pratt and Whitney, and General Electric. The materials discussed here were tested in the EPM program and are materials which could potentially be used in the combustor liner of the aircraft engine.

** On a minicomposite ruptured fracture surface, no B is detectable from EDS analysis. EDS is not the most sensitive technique for detecting B so it is assumed that only a small amount of B is present in the glass.

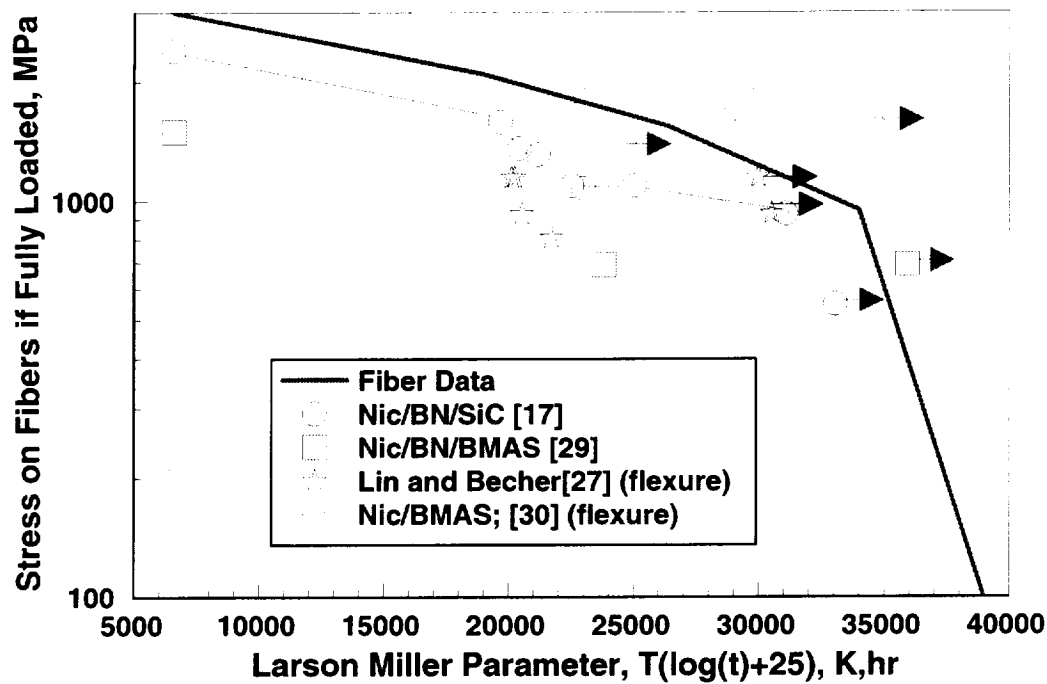


Figure 1.5: Larson Miller plot for Nic/BN/SiC minicomposites and as-produced Nicalon fibers.

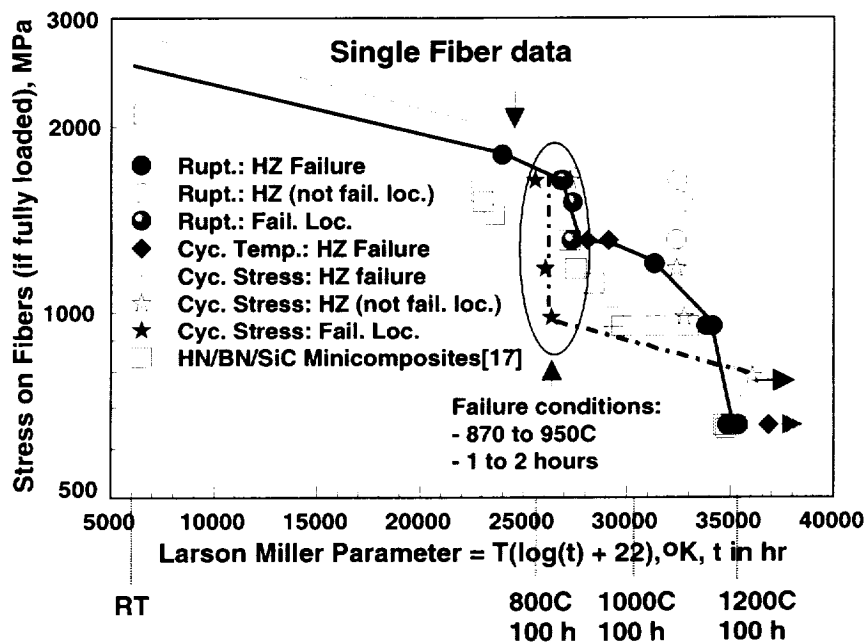


Figure 1.6: Larson Miller plot of HN/BN/SiC minicomposites and as-produced HN fibers in air. All of the data is from ref. 28 except where noted.



Figure 1.7: Portion of a HN/BN/SiC minicomposite fracture surface after 900°C rupture^[23]. Note gap between fiber and matrix and glass fusing fibers together or fiber and matrix together.

Flexural data from Lin and Becher^[27] is plotted in Figure 1.5 for Nic/BN/SiC. Similar embrittlement to the tensile data was observed for low temperature (600°C) conditions and short-time higher temperature (950°C) conditions. For longer times at 950°C, run-out occurred due to matrix crack sealing.

Also plotted on Figure 1.5 is data from Brennan^[32] for two tensile stress-rupture tests performed on a Nicalon fiber, BN interphase, BMAS glass ceramic composite. Even though this is a different matrix system, it is interesting to note that the rupture behavior of the intermediate temperature rupture condition (900°C; 6269 hrs) was what would be expected from the minicomposite results (i.e. if the rupture strength data for both the BMAS and minicomposites were normalized by the room temperature strength they would fall on the same curve). In what might at first be surprising, the higher temperature rupture condition (1200°C for ~ 1.6 years) never failed. But, although the temperature is increased, favoring kinetics, the system became isolated from the environment because the matrix undergoes a phase transformation at the higher temperature that results in any matrix cracks being sealed. At 900°C, sealing did not occur and the environment had access to the fiber and interphase.

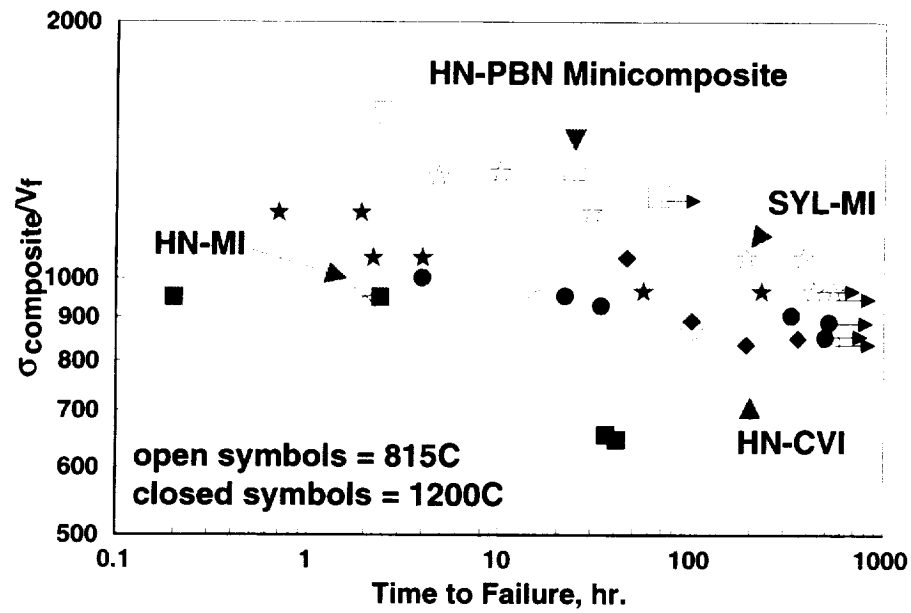
Flexural stress-rupture data is also plotted on Figure 1.5 from Sun et al^[33] for the same system as ref. 30. There was a decrease in rupture strength; however, not as severe as for the tensile stress-rupture condition.

A question arises as to why the Nic/BN/SiC minicomposites did not undergo the same embrittlement as Nic/C/SiC if the CVI processing conditions were the same. For the Nicalon fibers with BN interphases, a thin uniform glass layer forms on the fiber surface after interphase volatilization which protects the fibers from the environment^[17]. For the Nicalon fibers with C interphases, no such glass layer was observed due to the lack of a fluxing agent, exposing the fiber surface to the environment. Boria formation must have enhanced the oxidation of SiC as has been observed for similar conditions on bulk SiC^[31].

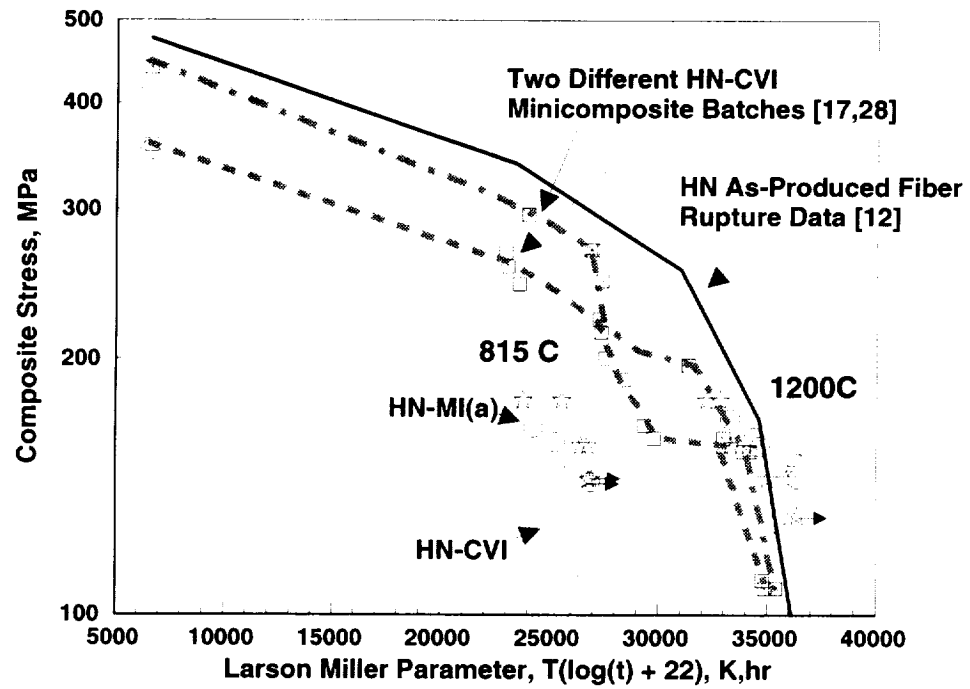
Figures 1.8 a and b show data for the HN/BN CVI SiC (15 v_{fo}) macrocomposites, MI SiC (17 v_{fo}) macrocomposites, SYL/BN MI SiC (15 v_{fo}) macrocomposites, and the HN/BN/SiC (16 v_{fo}) minicomposites as fiber stress versus time and on a Larson-Miller plot as composite stress, respectively. The composites were tested at 815°C and 1200°C. The macrocomposite experiments were not true stress-rupture experiments (constant load). Instead, the load was constant for two hours and then was cycled from the rupture load to zero to the rupture load and held at the original rupture load for two more hours. This low-cycle fatigue (LCF) pattern was repeated until failure. Four observations can be made from these results:

- (1) The composite rupture behavior at 815°C was much worse than the minicomposite rupture behavior whereas at 1200°C there was not much difference for the rupture behavior of macrocomposites, minicomposites, and as-produced fibers. This implies that the higher temperature rupture behavior is dominated by the fiber rupture properties. At the intermediate temperatures, an even more severe degradation phenomenon is occurring for the composites than for minicomposites.
- (2) The 815°C and 1200°C rupture times for the macrocomposites are nearly identical with stress in comparison to minicomposites.
- (3) The MI SiC matrix composite rupture behavior was slightly better than the CVI SiC matrix composite rupture behavior at intermediate temperatures.
- (4) SYL reinforced composites are superior in rupture to HN reinforced composites at intermediate temperatures.

The reasons for the first three observations were not obvious. SYL fiber composites would be expected to be more rupture resistant than HN fibers based on their fiber rupture properties at 815°C. Understanding the severe intermediate temperature embrittlement of the HN macrocomposites is the main objective of this thesis. It is obvious that there can be a difference between minicomposite and macrocomposite rupture behavior (even though for the carbon interphase systems this was not the case). Undoubtedly, these differences must be attributed to the nature of damage accumulation in these systems, the processing history, and the nature of crack growth at elevated temperatures in an oxidizing atmosphere. Therefore, the literature on damage accumulation in CMC's and elevated temperature embrittlement models was explored.



(a)



(b)

Figure 1.8: Fiber stress vs. time (a) and Larson Miller plot (b) of SiC/BN/SiC.

1.2 Damage Accumulation in CMC's

1.2.1 Matrix Cracking: The Non-Linear Stress Strain Curve

The reason for the non-linear stress-strain behavior in CMC's is because of damage accumulation in the composite (matrix cracking). The classic work describing the non-linearity of the stress-strain curve was by Aveston, Cooper, and Kelly (ACK)^[34]. ACK showed that if the fiber elongation is greater than that of the matrix and if the fibers are able to sustain the extra load applied when the matrix fails, non-linear stress-strain behavior will result. Figure 1.9 is a representation of the ACK theory.

Region 1: The composite is undamaged, the elastic modulus of the composite, E_c , can be represented by the rule of mixtures of the constituents of the composite:

$$E_c = v_f E_f + (1 - v_f) E_m \quad (1.1)$$

and the stress on the fiber and matrix is simply:

$$\sigma_f = \epsilon_f / E_f = \epsilon_c / E_f \quad (1.2a)$$

$$\sigma_m = \epsilon_m / E_m = \epsilon_c / E_m \quad (1.2b)$$

since $\epsilon_c = \epsilon_m = \epsilon_f$ (subscripts c, m, and f refer to composite, matrix, and fiber, respectively).

Region 2: When the stress reaches the matrix cracking stress, σ_{mc} ,

$$\sigma_{mc} = \{ (6 E_f v_f^2 \tau E_c^2 \Gamma_m) / [E_m^2 (1 - f) R_f] \}^{1/3} \quad (1.3)$$

where Γ_m = matrix fracture energy

R_f = fiber radius

τ = interfacial shear stress

the matrix fractures into multiple segments. The segment size or saturation crack spacing, l_s , was predicted by ACK to be bounded by:

$$l_d < l_s < 2l_d \quad (1.4)$$

where l_d is the slip length as defined by:

$$l_d = \sigma R_f E_m (1 - f) / [2 \tau E_f] \quad (1.5)$$

The saturation crack spacing, l_s , was later derived^[35] from statistical models to be $\sim 1.34l_d$.

For the ACK theory, the matrix is assumed to have an infinite Weibull modulus. This implies that all of the matrix cracks are formed at the same time and the stress in the matrix never exceeds a particular value σ_{mc} .

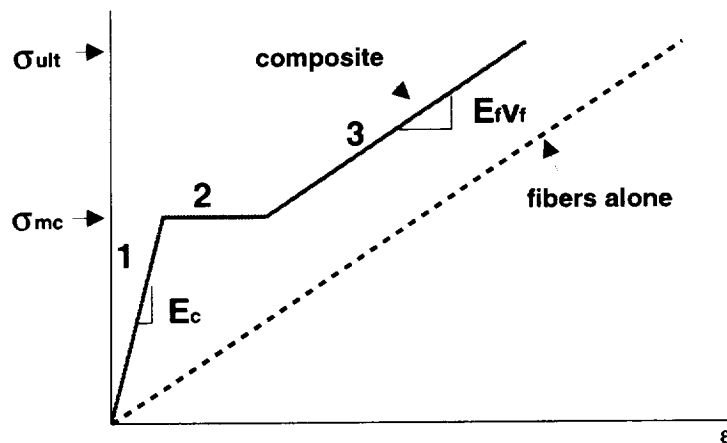


Figure 1.9: Stress-strain curve of a unidirectional composite based on ACK^[28] theory.

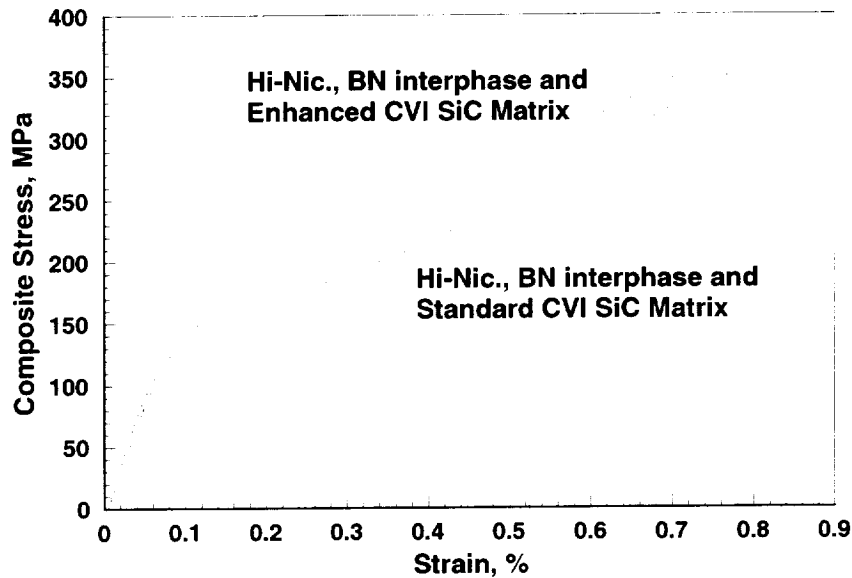


Figure 1.11: Comparison of woven Hi-Nicalon, CVI SiC matrix composites. The enhanced matrix contained some B_4C particles. The composites were processed by DuPont Lanxide and the tensile tests were performed by the author.

1.2.2 Quantifying Damage Accumulation

The “standard” CVD SiC composite rupture behavior (Figure 1.8) corresponds to the portion of the stress-strain curve just prior to and after the “knee” in the curve (Figure 1.11). Obviously, the amount of damage accumulated depends on the kinetics of the embrittlement processes. In order to model elevated-temperature stress-rupture behavior, the amount and nature of the damage accumulated over the stress-strain curve needs to be quantified.

The amount of damage accumulation can be understood from the stress-strain curve itself by performing unload-reload iterations (hysteresis loops) during the tensile test^[42-44]. The hysteresis loop moduli, hysteresis loop width, and permanent deformation at zero stress are indicative of the amount of damage which occurred in the composite. Alternatively, damage accumulation can be measured by polishing samples which had been subjected to different tensile loads to determine the number of cracks for a given length.

For the SiC/SiC system, the fibers tows are woven (usually 0/90 fiber tow orientation) into a cloth. Pieces of the woven cloth are stacked and then the woven laminate architecture is composited with the matrix. A woven architecture introduces several types of flaws and different matrix regions for cracking. Several studies^[45-47] have quantified the progression of cracking behavior for a Nicalon/SiC matrix composite. It was found that at low stresses initially non-fiber bridged microcracks emanate from macropores between different fiber plies and form in transverse (90°) bundles and dense matrix regions. With increasing stress (strain), these “tunnel” cracks^[48] propagate into the 0° fiber bundles. In addition, new cracks are formed in the 0° bundles. Eventually, cracks would coalesce to form through-thickness cracks across the composite. The onset of 0° cracks occurred somewhere between 0.06 and 0.085% strain for the material in Reference 45.

Since cracking in woven SiC/SiC composites occurs over a stress range and microcracks emanate at different flaw sites that eventually link up at higher stresses, it is reasonable to assume that the amount that cracks are linked up would control the degree to which the environment has access to the load-bearing fibers. Therefore, crack growth may have to be modeled based on the starting crack conditions and embrittlement of load bearing tows that the environment has access to.

One step towards understanding the amount of 0° bundle cracking for different SiC/SiC materials is to determine the onset stress or strain for 0° bundle cracking using the hysteresis loop technique (Figure 1.12) ^[49]. The hysteresis loop width can be plotted versus stress or strain (Figure 1.13) and extrapolated to zero loop width. The stress or strain for zero loop width would then correspond to the onset stress and onset strain for 0° cracking, respectively. From Figure 1.13 it is evident that the onset of 0° cracking occurs at a lower stress condition for CVI-SiC matrix composites compared to MI-SiC matrix composites. Also, 0° cracking occurs at a lower stress condition for Hi-Nicalon fiber composites than for SYL reinforced composites. Surprisingly, the onset strain condition is approximately the same for all the SiC/SiC systems, $\sim 0.075 \pm 0.005\%$.

This onset of 0° cracking can be related to the stress-rupture or LCF properties for SiC/SiC composites. Figure 1.14 shows the 0° onset-stress for several systems and the LCF data at 815 and 1200°C plotted on a Larson-Miller plot. It is evident that the run-out condition for LCF (500 hours) corresponds to the 0° crack-onset stress. The implication is that in order for these composites to fail, the 0° fiber bundles must be accessed by the environment through the matrix cracks.

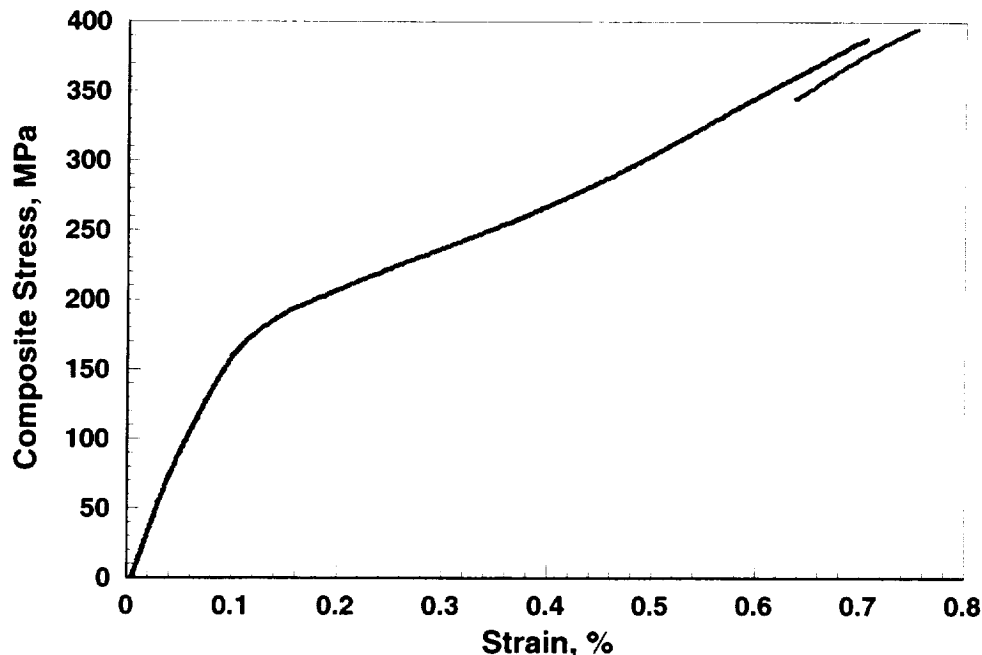
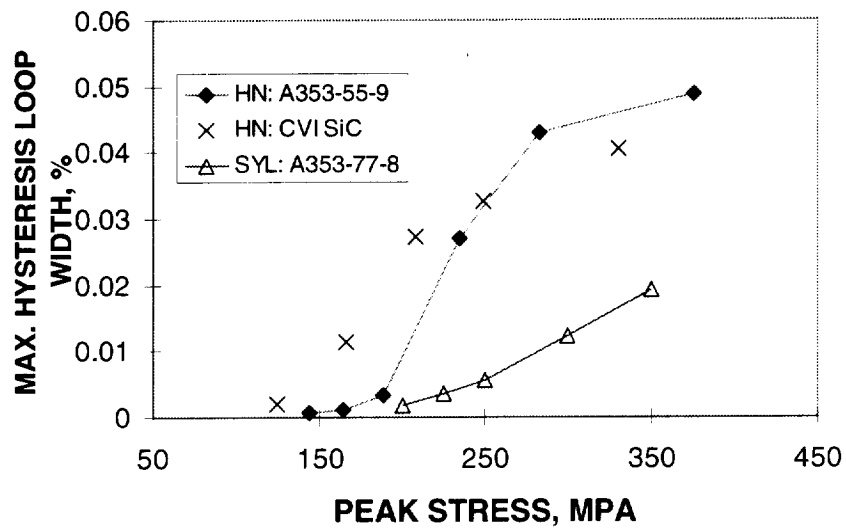
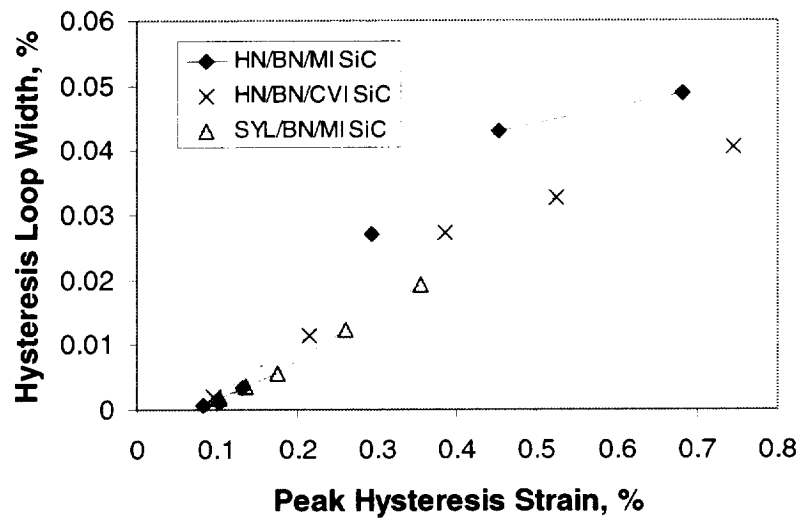


Figure 1.12: Monotonic and hysteresis loop performed on two different samples from the same HN/BN/MI composite.



(a)



(b)

Figure 1.13: Maximum hysteresis loop width versus (a) peak stress and (b) peak strain for several SiC/SiC composites.

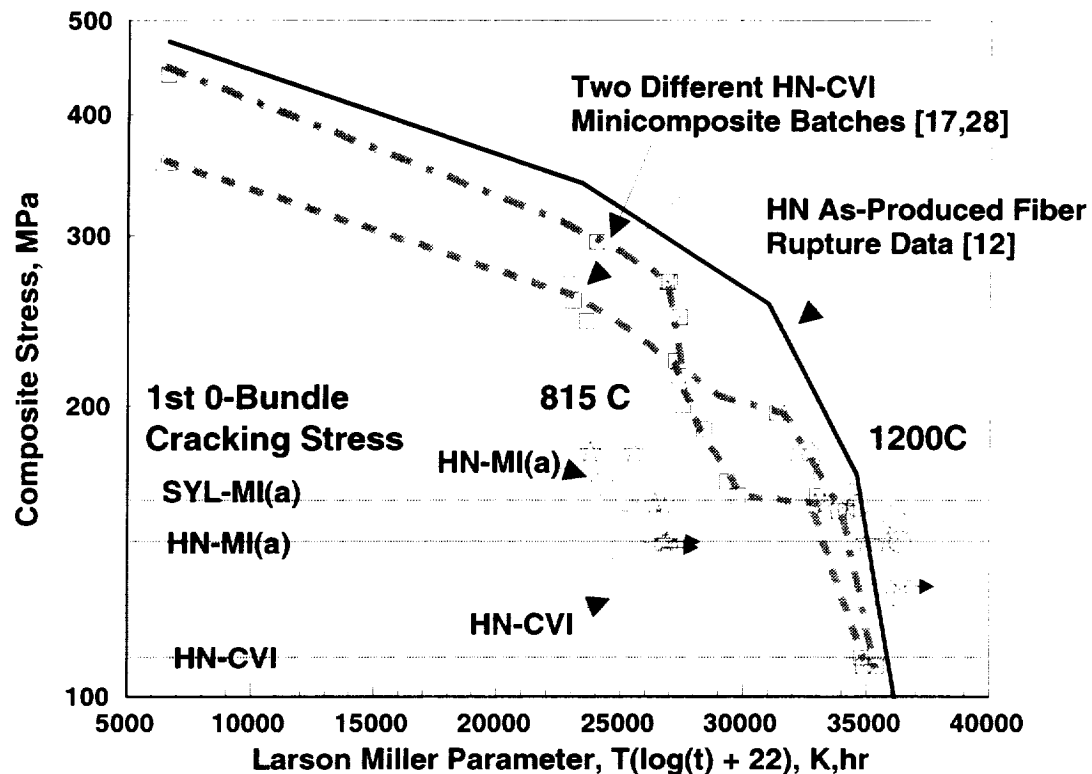


Figure 1.14: Larson Miller plot showing rupture properties of fibers and minicomposites, LCF properties of macrocomposites, and the 0° onset-cracking stress for macrocomposites.

1.2.3 Monitoring Damage Accumulation

Unfortunately, the process of quantifying the damage accumulation for a given CMC system can be destructive and very time intensive. An in-situ, or at least simpler method of monitoring damage accumulation for the stress-strain curve as well as for the stress-rupture test would be a tremendous achievement. Many nondestructive techniques such as x-ray and radiographic techniques have been developed for determining defects in materials. However, the cracks created during CMC deformation are usually too small for these techniques to be effective. One technique that holds the promise of monitoring damage during a tensile test is acoustic emission (AE).

Few studies exist on the use of AE for CMC's^[50-54], however, much work has been performed on the use of AE in graphite fiber reinforced epoxy composites^[e.g. 55-59]. For most AE studies, the AE activity corresponds to the nonlinearity in the stress strain curve; however, the interpretation of what is being heard can be difficult. For example, a recent study performed on SiC (Tyrrano) reinforced BMAS composites used traditional AE to deduce when matrix microcracking, matrix macrocracking accompanied by interface debonding, and delamination cracking were occurring during a monotonic stress-strain test^[51]. The reason for suspicion (at least on this author's part) of their interpretations centers around the fact that AE parameters (i.e. counts, amplitude, duration, energy, etc.) are derived on faulty sound waveform assumptions which lead to questionable results. Some attention will now be given to describe the shortcomings of "traditional AE" and the potential of modal AE analysis.

There are two fundamental weaknesses in the approach of traditional AE^[60,61]. First, traditional AE parameters base the determination of rise time, duration, amplitude, number of counts exceeding a threshold voltage... on a single frequency damped sine wave. Second, traditional AE sensors use resonant frequency transducers, i.e., they only resonate at narrow frequency ranges. The resulting fundamental problem is that what is being analyzed is physically different than the analysis assumptions.

Recent advancements in computer technology, sensor technology, and the incorporation of plate wave theory into AE systems has enabled AE waveforms to be captured digitally and analyzed based on their "modes"^[60-62]. A typical AE waveform from a pencil lead break on the standard CVI SiC composite is shown in Figure 1.15 as received by two wide-band frequency sensors. There are several features of real waveforms in CMC's which are important to recognize from Figure 1.15:

1. There are two characteristic "modes" or pure parts of the waveform. The first arriving part is the extensional (longitudinal) mode the second arriving part is the flexural mode. These different modes of the waveform travel at different velocities and at a range of frequencies. The extensional component travels at a faster velocity than the flexural component. This is why the time frame for the extensional component is larger for channel 2, which is farther away from the lead source, than channel 1. Traditional resonant AE sensors cannot detect the entire frequency ranges of the waveform. The frequency range of the extensional component of the waveform for the SiC/SiC composites of interest in this study is between 600 and 1500 kHz. Resonant frequency sensors usually resonate below 500 kHz, missing the extensional component altogether. The extensional component, as will be argued below, is the most important portion of the waveform for source location and perhaps source identification. In addition, the waveforms produced by unwanted noise, e.g., from the grips, is always of lower frequency content and thus easily separable. However, AE parameters determined by resonant frequency transducers for grip noise events may not be very different from that of the fracture events in the gage section. It is very easy to distinguish between unwanted grip or EMF noises with modal AE analysis^[62].
2. The waveform, after the first few peaks, is a superimposition of the true extensional, true flexural, and reflective components of both parts of the true sound wave modes produced from the fracture event. The waveform could be modeled as a damped sine wave. However, due to the waveguide nature of most tensile specimens, most of the waveform is dominated by the reflections which are a function of the sample dimensions not the material properties. When using traditional AE parameters such as duration, rise-time, counts, and energy, one is not measuring the true waveform but a narrow frequency range of a waveform modified by reflections.

3. The relationship between the extensional and flexural components of the waveform are indicative of where the event occurred through the thickness of a test specimen^[63]. For example, events which occur near the surface or which occur in shear will produce larger flexural component waveforms. Mode I type fracture events occurring internally in a sample will produce larger extensional component waveforms. This type of information may be used to discern the type of source event.
4. Location of AE source events is crucial to understanding what is happening in the gage section of the composite. Since sensors are usually attached outside of the gage section, reliable methods need to be employed to ascertain the location of events. If the speed of sound of the wave is known, then the difference in time of arrival (Δt_x in Figure 1.15) can be used to determine the location. The modes of the waveforms are dispersive, i.e. they travel at different velocities as a function of frequency (Figure 1.16). For traditional AE, which employ resonant frequency (< 500 kHz) transducers, the flexural component of the waveform could possibly be monitored. Unfortunately, the speed of sound of the flexural mode can vary significantly with frequency. The extensional component varies only little with frequency up to 1000 kHz. Therefore, even if different frequencies are recorded for different events, the extensional mode will result in much more accurate source location.

The use of modal AE may enable in-situ determination of source events in the gage section for CMC's. Part of the research documented in this thesis was aimed at monitoring the damage accumulation over the stress strain curve and during rupture testing using modal AE. The approach will be to analyze the frequency content, waveform energy, and location for different AE events to deduce the respective sources occurring over the stress strain curve.

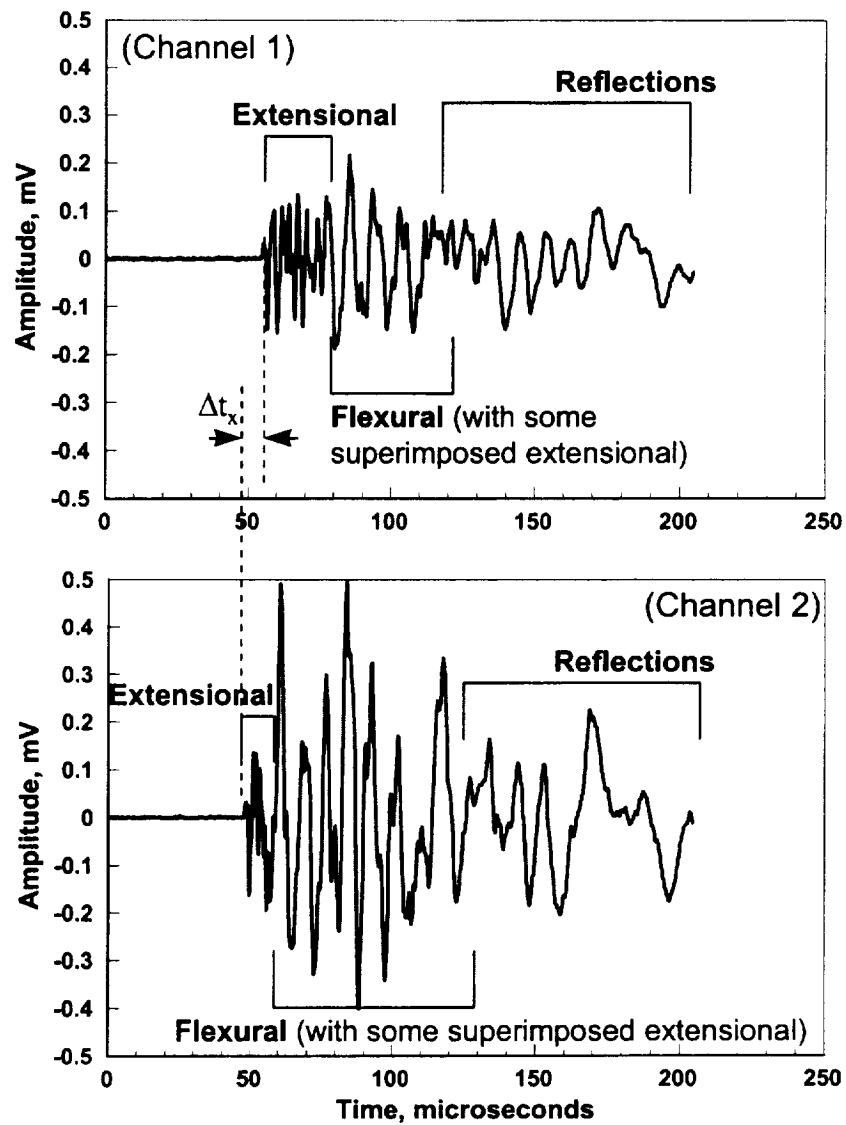


Figure 1.15: AE waveforms received on two channels (sensors) 65 mm apart from a lead break performed outside of both sensors on a Hi-Nicalon reinforced, standard CVI SiC matrix composite.

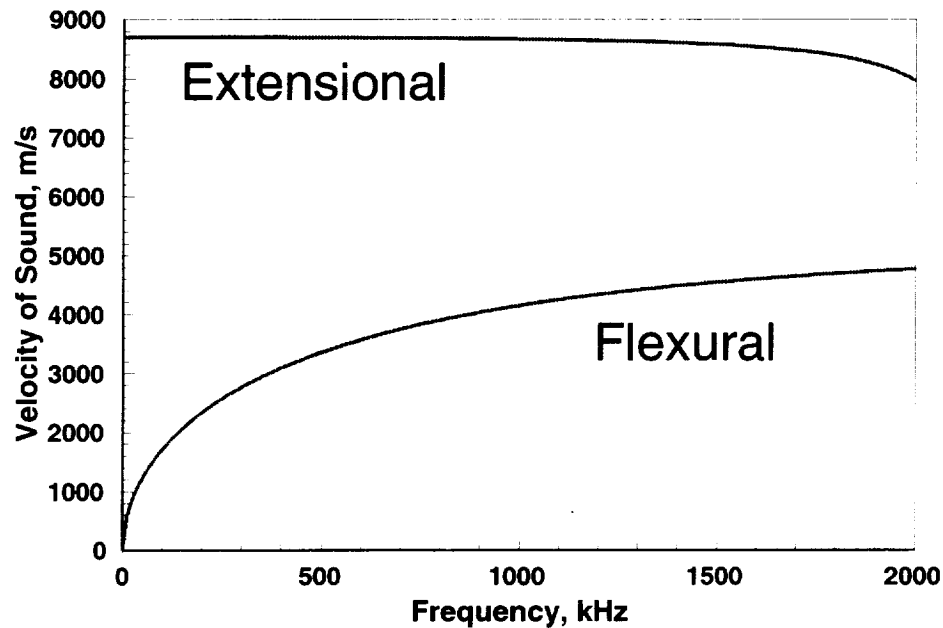


Figure 1.16: Dispersion curve of the phase velocity for the different modes of a waveform calculated from isotropic plate theory ($E = 200$ GPa and $\nu = 0.15$).

1.3 Modeling Composite Rupture

Modeling intermediate temperature composite-rupture must encompass the onset and degree of matrix cracking, rate of environmental access, reaction rate of environment with composite constituents, pertinent embrittlement mechanism of the load-bearing fibers, and crack propagation (if the composite is not fully saturated with cracks).

Several studies have been performed on one or more aspects of composite embrittlement. Henager and Jones^[64] have measured the subcritical crack growth in a CVI SiC CMC reinforced with Nicalon fibers at 1100°C in argon and argon with 2000 ppm O₂. The increase in stress intensity of the crack tip occurs in inert environments due to the intrinsic creep properties of the fibers (relaxation of bridging zone stresses). A definite increase in crack velocity was observed for the oxygen environment. The increased crack growth velocities in the oxygen-containing environment was due to loss of interface, reducing the load carrying capability of the matrix and increasing the stress-intensity of the crack tip.

Lara-Curzio et al.^[18] have modeled the stress-rupture properties of Nicalon reinforced CVI SiC composites with C interphases at 425°C in the presence of oxygen. In this model, the matrix is assumed to be cracked and the oxygen containing environment oxidizes the interphase, increasing the gage length of fully loaded fibers. A statistical approach is applied corresponding to the probability of fiber failure with increasing gage length (Weibull) based on the rate (depth) of carbon interphase recession. The strain versus time behavior was then modeled for different applied stress experiments with good agreement.

In another study, Lara-Curzio^[19] tested and modeled the rupture behavior of Nic/C/SiC composites tested at 950°C in air. They found that the rupture behavior followed a time exponent, n , of $-1/4$ ($\sigma = t^n$) which would be appropriate parabolic SiO₂-scale (flaw) growth. Assuming the strength-limiting flaw was the oxide scale, they determined a time-dependent fiber

strength. This time-dependent strength was then incorporated into the same probabilistic analysis of ref. 18 and used in this study to model the strain versus time behavior at different applied loads.

The most comprehensive approach to modeling composite embrittlement is that put forward by Evans et al.^[65]. Their model is based on the observed rupture behavior of a unidirectional Nicalon reinforced, C interphase, MAS glass ceramic composite in air at 750°C. Their model includes crack growth based on the weakening of the fibers due to oxide scale growth. They model three principal phenomena: (1) the reduction in fiber strength with oxide scale growth, (2) the stress concentration in the fibers at the perimeters of the unbridged crack segments, and (3) the oxygen concentration within the matrix cracks. According to this model, the initial narrow matrix crack opening inhibits the ingress of oxygen and egress of reaction products so that oxidation gradients develop. The outermost fibers oxidize and degrade most rapidly resulting in further fiber degradation that progresses into the composite. Eventually, the crack openings are wide enough and/or the crack propagation is slow enough, the oxygen concentration in the crack is uniform and all of the fibers are expected to fail simultaneously when the oxide scale thickness grows to a critical value. The crack then grows and the processes continue until the load on the remaining portion of pristine composite causes failure.

In this thesis, the modeling of stress-rupture for the HN/BN/MI-SiC composite system will be extended. Two important considerations will be incorporated into this model which are not accounted for in the earlier models: (1) the matrix damage state and (2) the “intrinsic” strength degradation of the load-bearing fibers.

As described in section 1.2, the damage accumulation of these composites does not result in planar through-thickness cracks at lower stresses. For C-interphase systems this is probably not a critical issue. For woven SiC/C/SiC it is likely that interphase volatilization at intermediate temperatures in a non-through-thickness cracked composite will cause crack opening and through-thickness crack growth in relatively short times (minutes to hours). For BN interphase systems the recession distances are very small (microns) and microcracks would not be expected to grow significantly or as quickly.

The intrinsic strength degradation under constant-load rupture conditions (Figure 1.1) may also be an issue for these systems. The rupture behavior of composites in the BN-interphase systems (Figures 1.5 and 1.8) is more similar to the individual fiber data than those of the Nic, C-interphase system (Figures 1.3). It appears that the BN coated fibers do not degrade in strength as fast as the Nic-C system. Therefore, the oxide scale growth mechanism^[19,65] for fiber strength degradation probably does not apply. It is interesting to note that thicker oxide scales are observed on the stronger fibers in BN-interphase composites than C-interphase composites for similar time, temperature, environment exposures^[17]. Also, the individual fiber tests performed to determine Figure 1.1 were in air, therefore, any oxide scale effect would already be incorporated into the fiber-weakening results. It is for these reasons that this author does not believe that an oxide scale-growth mechanism causes time-dependent degradation of fiber strength.

Ultimately, the failure of the composite will be when the applied load can no longer be supported by the remaining load-bearing fibers. This will be dependent on the fiber strength after the time, temperature, stress exposure and the number of fibers still carrying load in the eventual failure crack region. Knowing the time-dependent strength of the remaining fibers is therefore necessary for modeling the ultimate failure condition of the composite.

1.4 Works Cited

1. K. M. Prewo and J.J. Brennan, "High Strength Silicon Carbide Fiber Reinforced Glass Matrix Composites," *J. Mater. Sci.*, **15** [2] 463-68
2. K.M. Prewo and J.J. Brennan, "Silicon Carbide Yarn Reinforced Glass Matrix Composites," *J. Mater. Sci.*, **17** [4] 1201-1206 (1982)
3. J.J. Brennan and K.M. Prewo, "Silicon Carbide Fiber Reinforced Glass-Ceramic Matrix Composites Exhibiting High Strength and Toughness," *J. Mater. Sci.*, **17** [8] 2371-83 (1982)
4. D.B. Marshall and A.G. Evans, "Failure Mechanisms in Ceramic-Fiber/Ceramic-Matrix Composites," *J. Am. Ceram. Soc.*, **68** [5] 225-31 (1985)
5. A.M. Johnson, B.J. Batlett, and W.A. Troha, "Material Changes and Progress Toward Meeting the High Speed Civil Transport Propulsion Design Requirements," ISABE 97-7179, American Institute of Aeronautics and Astronautics, pp. 1321-1328 (1997)
6. M. Takeda, Y. Imai, H. Ichikawa, T. Ishikawa, N. Kasai, T. Seguchi, and K. Okamura, "Thermomechanical Analysis of the Low Oxygen Silicon Carbide Fibers Derived from Polycarbosilane," *Ceram. Eng. Sci. Proc.*, **14** [7-8] 540-547 (1993)
7. J. Lipowitz, J.A. Rabe, A. Zangvil, and Y. Xu, "Structure and Properties of Sylramic Silicon Carbide Fiber – A Polycrystalline, Stoichiometric β -SiC Composition," *Ceram. Eng. Sci. Proc.*, **18** [3] 147-157 (1997)
8. P. Le Coustumer, M. Monthieux, and A. Oberlin, "Understanding Nicalon Fibre," *J. European Ceram. Soc.*, **11** 95-103 (1993)
9. G. Chollon, R. Pailler, R. Naslain, F. Laanani, M. Monthieux, and P. Olry, "Thermal Stability of a PCS-derived SiC fibre with a Low Oxygen Content (Hi-Nicalon)," *J. Mater. Sci.*, **32** 327-347 (1997)
10. J. A. DiCarlo, "Creep Limitations of Current Polycrystalline Ceramic Fibers," *Comp. Sci. Tech.* **51** 213-222 (1994)
11. R. Bodet, X. Bourat, J. Lamon, and R. Naslain, "Tensile Creep Behavior of a Silicon Carbide-Based Fibre with a Low Oxygen Content," *J. Mater. Sci.*, **30** 661-77 (1995)
12. H.M. Yun and J. A. DiCarlo, "Time/Temperature Dependent Tensile Strength of SiC and Al₂O₃-Based Fibers," pp. 17-26 in Ceramic Transactions, vol. 74, Advances in Ceramic-Matrix Composites III. Edited by N.P. Bansal and J.P. Singh. American Ceramic Society, Westerville, OH, 1996

13. Yun and DiCarlo, unpublished data.
14. S.M. Wiederhorn, J.D. French, and W.E. Luecke, "A Comparison of Fracture Mechanism Maps with the Larson-Miller Method of Predicting Life-time," *Ceram. Eng. Sci. Proc.*, **16** [5] 691-98 (1995)
15. F.E. Heredia, J.C. McNulty, F.W. Zok, and A.G. Evans, "Oxidation Embrittlement Probe for Ceramic-Matrix Composites," *J. Am. Ceram. Soc.*, **78** [8] 2097-100 (1995)
16. H.T. Lin and P.F. Becher, "Stress-Temperature-Lifetime Response of Nicalon Fiber-Reinforced SiC Composites in Air,"; pp. 128-41 in *ASTM Symposium of Thermal and Mechanical Test Methods and Behavior of Continuous-Fiber Ceramic Composites*, ASTM STP 1309, Eds. M.G. Jenkins, S.T. Gonczy, E. Lara-Curzio, N.E. Ashbaugh, and L.P. Zawada (1997)
17. G.N. Morscher, "Tensile Stress Rupture of SiC_f/SiC_m Minicomposites with Carbon and Boron Nitride Interphases at Elevated Temperatures in Air," *J. Am. Ceram. Soc.*, **80** [8] 2029-42 (1997)
18. E. Lara-Curzio, M.K. Ferber, and P.F. Tortorelli, "Interface Oxidation and Stress-Rupture of NicalonTM/SiC CVCCs at Intermediate Temperatures," Key Engineering Materials Vols. 127-131, Trans Tech Publications, Switzerland, pp. 1069-1082 (1997)
19. E. Lara-Curzio, "Stress-Rupture of Nicalon/SiC Continuous Fiber Ceramic Matrix Composites in Air at 950oC," *J. Am. Ceram. Soc.*, **80** [12] 3268-72 (1997)
20. P. Lipetzky, N.S. Stoloff, and G.J. Dvorak, "Atmospheric Effects on High-Temperature Lifetime of Ceramic Composites," *Ceram. Eng. Sci. Proc.*, **18** [4] 355-362 (1997)
21. T.E. Steyer, F.W. Zok, and D.P. Walls, "Stress Rupture of an Enhanced NicalonTM/SiC Composite at Intermediate Temperatures," *J. Am. Ceram. Soc.* **81** [8] 2140-46 (1998)
22. M.J. Verilli, A.M. Calomino, and D.N. Brewer, "Creep-rupture Behavior of a Nicalon/SiC Composite," Thermal and Mechanical Test Methods and Behavior of Continuous-Fiber Ceramic Composites, ASTM STP 1309, eds. M.G. Jenkins, S.T. Gonczy, E. Lara-Curzio, N.E. Ashbaugh, and L. Zawada, ASTM pp. 158-175 (1997)
23. L. Filipuzzi, G. Camus, R. Naslain, and J. Thebault, "Oxidation Mechanisms and Kinetics of 1D-SiC/C/SiC Composite Materials: I, An Experimental Approach," *J. Am. Ceram. Soc.*, **77** [2] 459-466 (1994)
24. A.J. Eckel, J.D. Cawley, and T.A. Parthasarthy, "Oxidation Kinetics of a Continuous Carbon Phase in a Nonreactive Matrix," *J. Am. Ceram. Soc.*, **78** [4] 972-80 (1995)

25. J.D. Cawley, "Effect of Interphase Carbon Thickness on Environmental Resistance of Continuous Fiber-Reinforced Ceramic Matrix Composites," pp. 377-84 in *Ceramic Transactions*, Vol. 58, *High-Temperature Ceramic-Matrix Composites II*, Edited by A.G. Evans and R. Naslain. American Ceramic Society, Westerville, OH, (1995)
26. J. Martinez-Fernandez and G.N. Morscher, "Stress Rupture of Hi-Nicalon, Carbon Interphase, CVI SiC Matrix Minicomposites in Air," unpublished results
27. H.T. Lin and P.F. Becher, "Effect of Coating on Lifetime of Nicalon Fiber-Silicon Carbide Composites in Air," *Mater. Sci. Eng.* A231 143-150 (1997)
28. G.N. Morscher, "The Effect of Static and Cyclic Tensile Stress and Temperature on Failure for Precracked Hi-Nicalon/BN/CVD SiC Minicomposites in Air," *Ceram. Eng. Sci. Proc.*, (1997)
29. D. Brewer, A. Calomino, and M. Verilli, Unpublished data from the Enabling Propulsion Materials Program at NASA Glenn Research Center.
30. W. H. Glime and J.D. Cawley, "Stress Concentration Due to Fiber-Matrix Fusion in Ceramic Matrix Composites," *J. Am. Ceram. Soc.* **81** [10] 2597-604 (1998)
31. N.S. Jacobson, G.N. Morscher, D.R. Bryant, and R.E. Tressler, "High Temperature Oxidation of Boron Nitride Part II: BN Layers in Composites," *J. Am. Ceram. Soc.* **82** [6] 1473-82 (1999)
32. J.J. Brennan, private communication; E.Y. Sun, S.R. Nutt, and J.J. Brennan, "Interfacial Microstructure and Chemistry of SiC/BN Dual-Coated Nicalon-Fiber-Reinforced Glass-Ceramic Matrix Composites," *J. Am. Ceram. Soc.*, **77** [5] 1329-39 (1994)
33. E.Y. Sun, H.T. Lin, and J.J. Brennan, "Intermediate-Temperature Environmental Effects on Boron Nitride-Coated Silicon Carbide-Fiber-Reinforced Glass-Ceramic Composites," *J. Am. Ceram. Soc.*, **80** [3] 609-14 (1997)
34. J. Aveston, G.A. Cooper, and A. Kelly, "Single and Multiple Fracture," The Properties of Fibre Composites; IPC Science and Technology Press, Ltd, p. 15-24 (1971)
35. A.C. Kimber and J.G. Keer, "On the Theoretical Average Crack Spacing in Brittle Matrix Composites Containing Continuous Aligned Fibers," *J. Mater. Sci. Letters* **1** 353-354 (1982)
36. D.B. Marshall, B.N. Cox, and A.G. Evans., "The Mechanics of Matrix Cracking in Brittle Matrix Fiber Composites," *Acta Metall.*, **33** [11] 2013-21 (1985)
37. W.A. Curtin, "Multiple Matrix Crack Spacing in Brittle Matrix Composites," *Acta. Metall. Mater.* **41** [5] 1369-1377 (1993)

38. N. Lissart and Lamon, "Damage and Failure in Ceramic Matrix Minicomposites: Experimental Study and Model," *Acta. Mater.* **45** [3] 1025-1044 (1997)
39. S.M. Spearing, F.W. Zok, and A.G. Evans, "Stress Corrosion Cracking in a Unidirectional Ceramic-Matrix Composite," *J. Am. Ceram. Soc.*, **77** [2] 562-70 (1994)
40. F.W. Zok and S.M. Spearing, "Matrix Crack Spacing in Brittle Matrix Composites," *Acta Metall. Mater.* **40** [8] 2033-2043 (1992)
41. B. Budiansky, J.W. Hutchinson, and A.G. Evans, "Matrix Fracture in Fiber-Reinforced Ceramics," *J. Mech. Phys. Solids* **34**, 167-189 (1986)
42. E. Vagaggini, J-M. Domergue, and A.E. Evans, "Relationships between Hysteresis Measurements and the Constituent Properties of Ceramic Matrix Composites: I, Theory," *J. Am. Ceram. Soc.*, **78** [10] 2709-20 (1995)
43. J-M. Domergue, E. Vagaggini, and A.G. Evans, "Relationships between Hysteresis Measurements and the Constituent Properties of Ceramic Matrix Composites: II, Experimental Studies on Unidirectional Materials," *J. Am. Ceram. Soc.*, **78** [10] 2721-31 (1995)
44. J.M. Domergue, F.E. Heredia, and A.G. Evans, "Hysteresis Loops and the Inelastic Deformation of 0/90 Ceramic Matrix Composites," *J. Am. Ceram. Soc.*, **79** [1] 161-70 (1996)
45. L. Guillaumat and J. Lamon, "Multi-fissuration de Composites SiC/SiC," in Revue des Composites et des Materiaux Advances, vol. 3, pp. 159-171 (1993)
46. L. Guillaumat and J. Lamon, "Probabilistic-Statistical Simulation of the Non-Linear Mechanical Behavior of a Woven SiC/SiC Composite," *Comp. Sci. Tech.*, **56** pp. 803-808 (1996)
47. P. Pluvinage, A. Parvizi-Majidi, and T.W. Chou, "Damage Characterization of Two-Dimensional woven and Three-Dimensional Braided SiC-SiC Composites," *J. Mater. Sci.*, **31** 232-241 (1996)
48. B.N. Cox and D.B. Marshall, "Crack Initiation in Fiber-Reinforced Brittle Laminates," *J. Am. Ceram. Soc.*, **79** [5] 1181-88 (1996)
49. G.N. Morscher, J.Z. Gyekenesi, and R.T. Bhatt, "Damage Accumulation in Woven SiC/SiC Composites," , submitted to *Environmental, Mechanical, and Thermal Properties and Performance of Continuous Fiber Ceramic Composite (CFCC) Materials and Components, ASTM STP 1392*

50. A. Chulya and J.P. Gyekenyesi, "In-situ NDE Monitoring of Crack Bridging in Ceramic Composites via Crack Opening Displacement," Presented at International Gas Turbine and Aeroengine Congress, The Hague, Netherlands; June 13-16, 1994. ASME publication 94-GT-444
51. G.N. Morscher and J. Martinez-Fernandez, "Determination of Interfacial Properties Using a Single-Fiber Microcomposite Test," *J. Am. Ceram. Soc.*, **79** [4] 1083-91 (1996)
52. M. Surgeon, E. Vanswijghoven, M. Wevers, and O. Van Der Biest, "Acoustic Emission During Tensile Testing of SiC-Fibre-Reinforced BMAS Glass-Ceramic Composites," *Composites Part A*, **28A**, pp. 473-480 (1997)
53. N. Lissart and J. Lamon, "Damage and Failure in Ceramic Matrix Minicomposites: Experimental Study and Model," *Acta Mater.* **45** [3] 1025-44 (1997)
54. G.N. Morscher and J. Martinez-Fernandez, "The Interfacial and Ultimate Strength Properties for Several Single Tow SiC-Fiber, CVI SiC Matrix Minicomposites at Room Temperature," *J. Am. Ceram. Soc.* **82** [1] 145-55 (1999)
55. D. Valentin, P. Bonniau, and A.R. Bunsell, "Failure Mechanism Discrimination in Carbon Fibre-Reinforced Epoxy Composites," *Composites*, **14** [4] 345-351 (1983)
56. D.J. Buttle and C.B. Seruby, "Acoustic Emission Source Location in Fiber Reinforced Plastic Composites," *J. Acoustic Emission*, **7** [4] 211-223 (1988)
57. S.M. Ziola and M.R. Gorman, "Transverse Cracking and Longitudinal Splitting in Graphite/Epoxy Tensile Coupons as Determined by Acoustic Emission," *J. Acoustic Emission*, **8** [3] 51-60 (1989)
58. J.P. Favre and J.C. Laizet, "Amplitude and Counts per Event Analysis of the Acoustic Emission Generated by the Transverse Cracking of Cross-ply CFRP," *Comp. Sci. Tech.*, **36** pp. 27-43 (1989)
59. K. Kawamoto and K. Ono, "Pattern Recognition Analysis of Acoustic Emission Signals from Carbon Fiber/Epoxy Composites," AECM-3 Third International Symposium On Acoustic Emission from Composite Materials, Paris France, July 17-21, 1989. Published by American Society for Nondestructive Testing, Inc., Columbus, OH, pp. 230-239 (1989)
60. M. R. Gorman, "Plate Wave Acoustic Emission," *J. Acoust. Soc. Am.*, **90** [1] 358-364
61. M. R. Gorman, "New Technology for Wave Based Acoustic Emission and Acousto-Ultrasonics," AMD-Vol. 188, Wave Propagation and Emerging Technologies, ASME, pp. 47-59 (1994)

62. W.H. Prosser, K.E. Jackson, S. Kellas, B.T. Smith, J. McKeon, and A. Friedman, "Advanced, Waveform Based Acoustic Emission Detection of Matrix Cracking in Composites," *Mater. Evaluation* 53 [9] 1052-8 (1995)
63. M.R. Gorman and W.H. Prosser, "AE Source Orientation by Plate Wave Analysis," *J. Acoustic Emission*, 9[4] 283-288 (1991)
64. C.H. Henager Jr. and R.H. Jones, "Subcritical Crack Growth in CVI Silicon Carbide Reinforced with Nicalon Fibers: Experiment and Model," *J. Am. Ceram. Soc.*, 77 [9] 2381-94 (1994)
65. A.G. Evans, F.W. Zok, R.M. McMeeking, and Z.Z. Du, "Models of High-Temperature, Environmentally Assisted Embrittlement in Ceramic-Matrix Composites," *J. Am. Ceram. Soc.*, 79 [9] 2345-52 (1996)

2.0 EXPERIMENTAL PROCEDURE

Several properties of the constituents for the two SiC/SiC composites evaluated in this study are described in Table 2.1. The material consists of eight plies of woven Hi-Nicalon, a $\sim 0.5 \mu\text{m}$ boron nitride interphase, and a melt infiltrated (MI) or chemically vapor infiltrated (CVI) SiC matrix. The MI matrix was processed in several steps. First a thin ($\sim 2 \mu\text{m}$) layer of SiC was applied by CVI to the BN coated woven preform. A SiC particle containing slurry was infiltrated into the porous network. This was followed by infiltration of molten Si that nearly filled the porous network. Therefore the matrix is predominantly SiC with some Si. It should be noted that the Si in the MI portion of the matrix is interconnected.

2.1 Mechanical Testing and Acoustic Emission

The tensile test set-up is shown in Figure 2.1. Most tensile tests were performed using a screw-driven universal testing machine^{*}. One test was performed on a hydraulic universal testing machine^{*}. The MI-matrix test specimens were flat with dimensions of 2.1 mm thickness, 12.5 mm width and 150 mm length. The CVI-matrix test specimens were dogbones with dimensions of 2.35 mm thickness, 10.3 mm width and 150 mm length. High temperature graphite-epoxy tabs (0.08" thick) were glued to the ends of the bars. The test specimens were gripped with hydraulic grips in the tabbed region. Wide band (50 kHz to 2 MHz) acoustic emission sensors^{**} were attached to the ends of the tensile specimens within the grips with quick setting epoxy. This was done to insure that the temperature the sensors experienced was maintained at approximately 25°C. A resistance-heated furnace (MoSi₂ elements) was used to heat the center section of the specimens. The furnace dimension in the tensile direction was 75 mm; however, the hot zone was only approximately 15 mm.

AE monitoring was performed with a Digital Wave Fracture Wave Detector^{**}. The signal was amplified 20 dB on the preamplifier and 9 dB on the signal processor. The trigger was amplified 21 dB. The digitization rate was set at 10 MHz and the memory length was set at 1024 points; therefore, the time frame for each event was 102.4 microseconds. It is important to note that the location of the events could be determined from the speed of sound of the damaged material, which was determined experimentally, and the difference in times of arrival of the waveforms corresponding to the same event on the two AE sensors.

The experimental test procedure was as follows:

1. Samples were mounted in the machine and pencil lead breaks were performed at an edge and on the face at a known distance from one of the edges in order to determine the speed of sound in the undamaged state.
2. The furnace was heated up to the desired set temperature. Acoustic emission was monitored at the beginning of the heating cycle and was continued until the final failure of the material. A constant tensile load of 100 N (3.8 MPa) was applied, under load control during heating to account for the thermal expansion of the material.
3. SiC contact extensometers were applied to the edge of the tensile bar.
4. The sample was loaded to the predetermined tensile load at 0.25 mm/min. The sample was then held at the predetermined load until failure.

^{*} Instron 4502, Instron, Canton, MA.

^{*} Instron 8500, For this test, an induction heated SiC element furnace was used.

^{**} Digital Wave Corp., Englewood, CO

Table 2.1: Composite constituent properties.

Constituent	Material	Volume Fraction	Elastic Modulus, GPa	Details
<i>MI-matrix Composite</i>				
Fiber	Hi-Nicalon ^a	0.34	270	5 Harness Satin (17 epi)
Interphase	Boron Nitride	0.10	Unknown	~ 0.5 μm thick
	CVI ^b SiC and	0.18	425	~ 2 mm thickness
Matrix	MI SiC + Si Porosity	0.34 0.04	345	Process Temp. ~ 1400°C
<i>CVI-Matrix Composites</i>				
Fiber	Hi-Nicalon ^a	0.30	270	8 Harness Satin (17 epi)
Interphase	Boron Nitride	0.10	Unknown	~ 0.5 μm thick
	CVI ^b SiC	~ 0.40	425	
Matrix	Porosity	~ 0.20		Continuous porosity

^a Nippon Carbon, Tokyo, Japan

^b Chemical Vapor Deposition Process

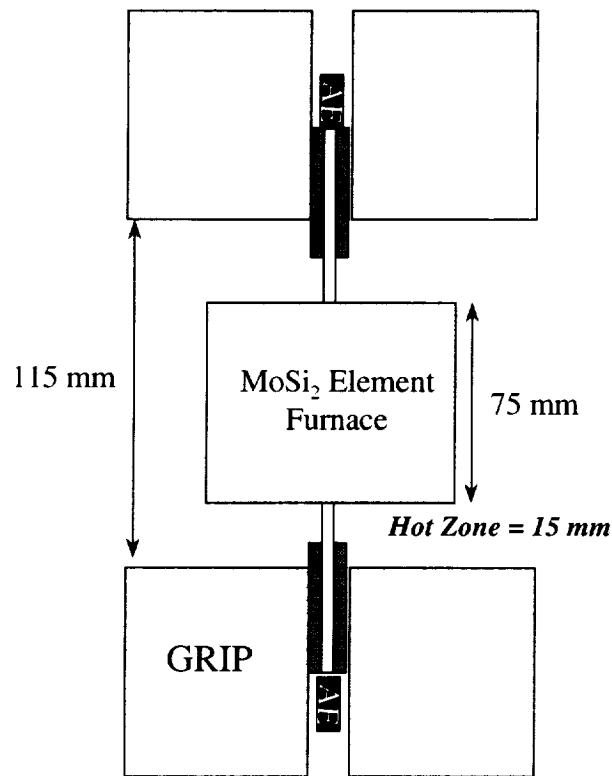


Figure 2.1: Schematic representation of the tensile test set-up.

5. Post-test analysis of the AE events was then performed. The energy of each waveform and the location along the test bar length were determined [1].
6. Some samples were cut and polished lengthwise in order to determine the extent of transverse cracking along the length.

2.2 Matrix Crack Determination

In order to determine the damage accumulation, several of the ruptured composites were cut and polished along the length of the tensile bar using standard metallographic techniques. Composite lengths of ~ 40 mm on one side or the other of the fracture surface were mounted and polished. These polished portions included the length of composite exposed to the hot zone region as well as regions exposed to lower temperatures. The polished samples were plasma etched with gaseous HF in order to enhance the matrix cracks.

Plasma etching severely etches the Si in the MI matrix which sometimes made it difficult to observe cracks which were through several plies or through the thickness of the composite. However, the cracks through the CVI SiC surrounding the tows always were easily observed. Therefore, the crack density in the CVI SiC was determined for an interior ply and an exterior ply. The crack density was determined over ~ 10 mm lengths of the tensile bar.

2.3 Scanning Electron Microscopy

The fracture surfaces were examined with a conventional* (SEM) and/or field emission** (FESEM) scanning electron microscope. For the FESEM, a low voltage of 5 kV was used which thus required no conductive coating on the specimen. General observations were made on the fracture surfaces. Individual fiber fracture surfaces were also obtained from various regions of the fracture surface in order to perform fiber fractography analysis. Electron dispersive spectroscopy (EDS)*** was performed on matrix, interphase, and fiber surfaces to determine the extent of oxidation. Microscopy was performed on samples tested in this study as well as on two fracture surfaces of specimens that were obtained from Brewer et al. [2]

2.4 Works Cited

1. G.N. Morscher, "Modal Acoustic Emission of Damage Accumulation in a Woven SiC/SiC Composite," *Comp. Sci. Tech.* **59** 687-697 (1999).
2. D. Brewer, A. Calomino, and M. Verilli, unpublished research.

* Jeol JSM 840A, Tokyo, Japan

** Hitachi S4500, Tokyo, Japan

*** Kevex 4460 Pulse Processor with Quantum Ultrathin Window and IXRF Systems, Inc. Software.

3.0 RESULTS

3.1 Melt-Infiltration Composite Rupture

In this study most of the data was taken from and microstructural analysis performed on MI-matrix composites. However, a smaller number of CVI-matrix composite rupture tests have been performed by Brewer et al. [1] and in this study. These are discussed in section 3.2 and compared to the MI matrix data.

3.1.1 Stress-Rupture Data

The stress-rupture results versus time are shown in Figure 3.1. The experiments were initially performed with a furnace hot zone temperature thought to be 815°C in order to compare this study with the data of Brewer et al. [1]. Both sets of data are listed in Table 3.1. The first two specimens failed outside of the hot zone. Therefore, the furnace profile was determined with a thermocouple that was translated through the furnace at 1 mm increments. The hot zone temperature for the conditions of the first two experiments was found to be 960°C (Figure 3.2). The temperature where the first two rupture specimens failed was ~ 880°C. The hot zone temperature for the next four rupture specimens was truly at 815°C. Three of those samples failed in the hot zone and two of those samples did not fail for the allotted time of the experiment (138 hours).

The 815°C fast fracture strength is also plotted on Figure 3.1 [1]. Combining the two sets of data, there appears to be two rupture regimes: a more severe rate of rupture occurs at higher stresses whereas a less severe rate of rupture occurs at lower stresses. There is a slight difference in the transition stress between these two regimes for the two sets of data. The data from Brewer et al. having better rupture properties and a higher transition stress (~ 165 MPa) compared to the material tested in this study which had a transition stress of ~ 150 MPa. The high stress regime will be referred to as Regime I and the low stress regime will be referred to as Regime II.

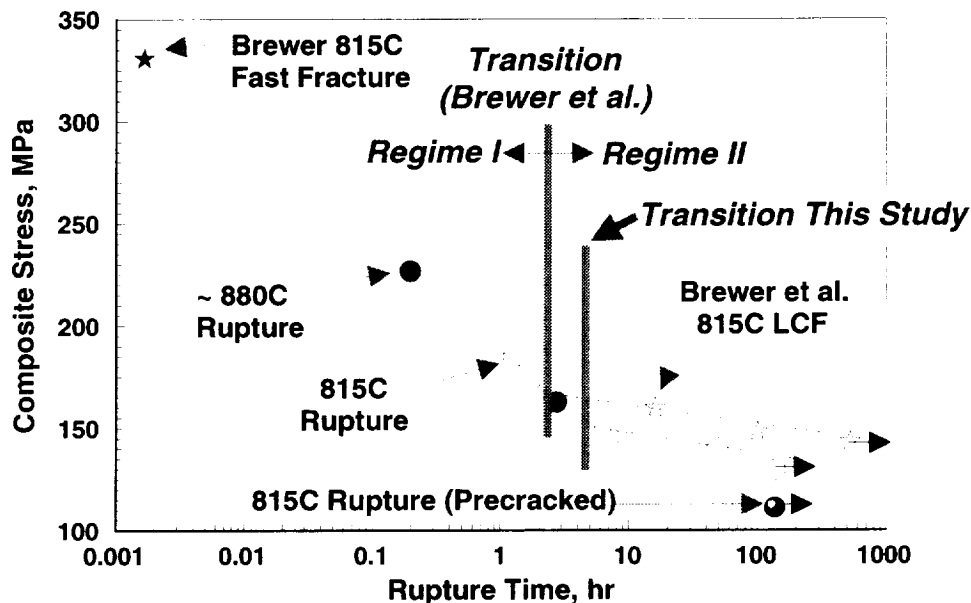


Figure 3.1: MI matrix composite stress-rupture data from this study and LCF data from ref. 1 plotted versus time. Also plotted is the 815°C fast fracture strength of the composite tested in ref. 1.

Table 3.1: MI-Matrix Stress-Rupture, LCF, and Fast Fracture Data.

Applied Stress, MPa	Hot Zone Temperature, °C	Time to Failure, hr	Failure Temperature, °C	Applied Load, kN
<i>Stress-Rupture Results</i>				
227	960	0.2	~ 880	6
185	815	1.3	815	5
163	960	2.8	~ 880	4.4
148	815	8.8	815	4
140	815	49	815	3.8
129	815	138	Did not fail	3.5
111*	815	138	Did not fail	3.0
> 344	25	Fast Fracture (did not fail in gage section)		
<i>LCF and Fast Fracture Results From Reference 1</i>				
166	815	2	815	
160	815	18.1	815	
148	815	114	815	
143	815	527	Did not fail	
331	815	Fast fracture	815	
351	25	Fast fracture	25	

* Precracked to 227 MPa at room test prior to the rupture condition.

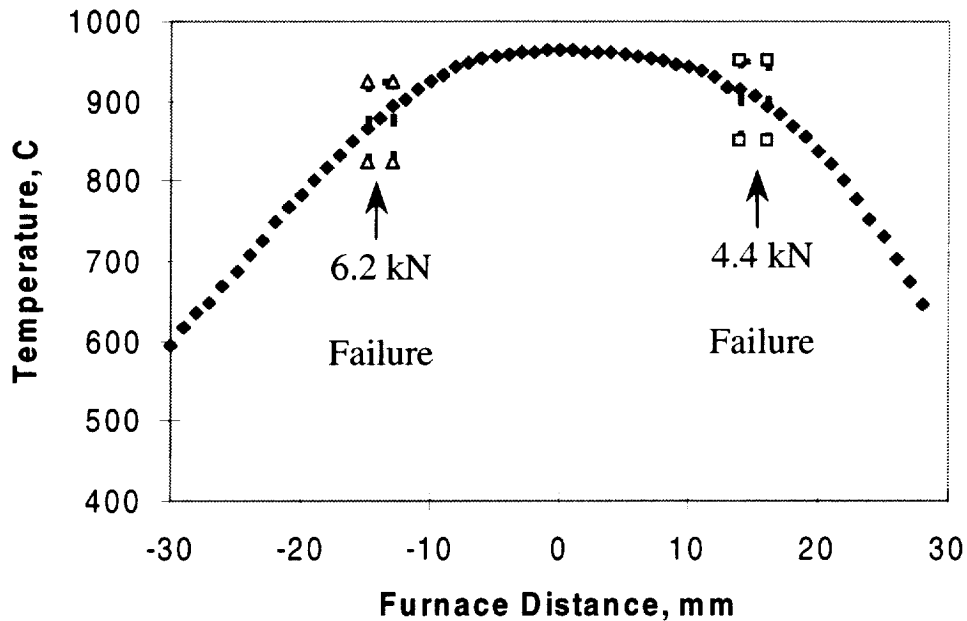


Figure 3.2: Furnace profile and location of failure for first two stress-rupture experiments.

The stress-strain curves for several stress-rupture experiments and for a room temperature fast fracture test of a specimen from the same panel are shown in Figure 3.3. The initial loading of the stress-rupture experiment is identical to that of the room temperature stress-strain curve up to the rupture stress, except for the precracked specimen, after which additional strain is accumulated with time. The precracked specimen would have been damaged significantly. It is expected that the modulus would be reduced for this specimen and for the stress-strain response after precracking to be parabolic. Note that the transition stress between the two rupture regimes is at the beginning of the “knee” in the stress-strain curve.

The “knee” is associated with increased damage in the matrix in the form of through thickness cracking. The room temperature stress-strain behavior obtained for the ref. 1 material and the room temperature stress strain behavior of the samples tested in this study are plotted together with the intermediate rupture behavior in Figure 3.4. The room temperature stress-strain curves are very similar except that the “knee” in the curve occurs at a lower stress for the material tested in this study compared to the material tested by Brewer et al.[1]. In fact for both materials, the transition stress corresponds to the beginning of the “knee” in the stress-strain curve, i.e. through thickness cracking. Therefore, the higher stress rupture rate appears to occur for a matrix state of through thickness cracking; whereas the low stress rupture rate appears to occur for a matrix damage state of non-through thickness microcracks. This was confirmed by other results presented below. Because of this correlation, an additional experiment was performed where the composite was precracked at 227 MPa at room temperature and tested at 815C at 111 MPa (Figure 3.1). It was thought that this rupture condition could result in a failure time corresponding to the rupture rate for Regime I (~ 30 hours). However, the specimen lasted much longer than expected and after 138 hours the experiment was stopped.

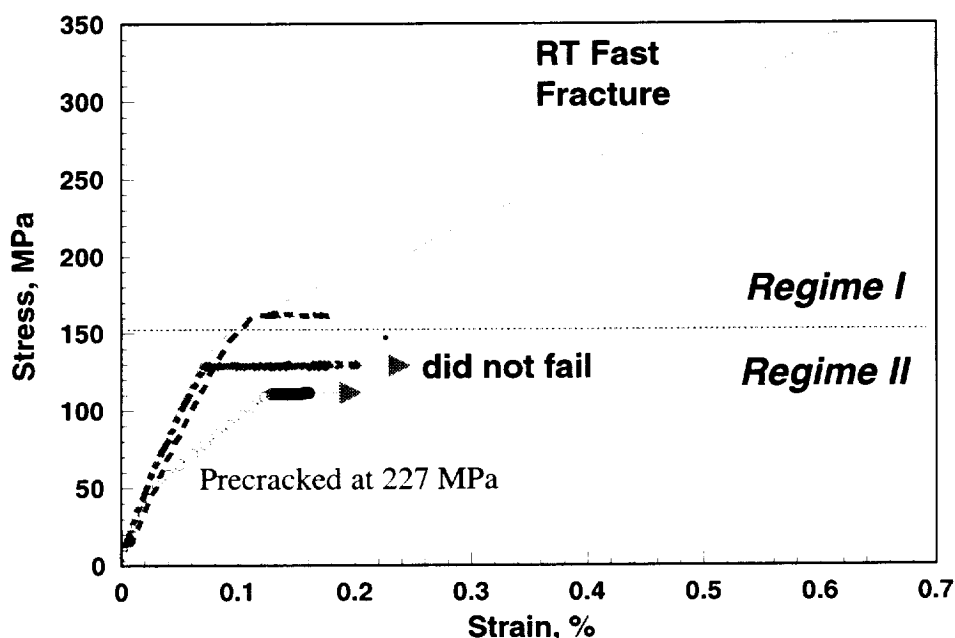


Figure 3.3: Stress-strain behavior of material tested at room temperature fast fracture and for several rupture tests. Note that the apparent load drops in the RT fast fracture curve are actually associated with unload/reload hysteresis loops which have been removed from the stress-strain curve for clarity. Also, the failure location of the RT fast fracture specimen occurred in the grips; therefore, the ultimate strength is greater than the failure stress shown in this figure.

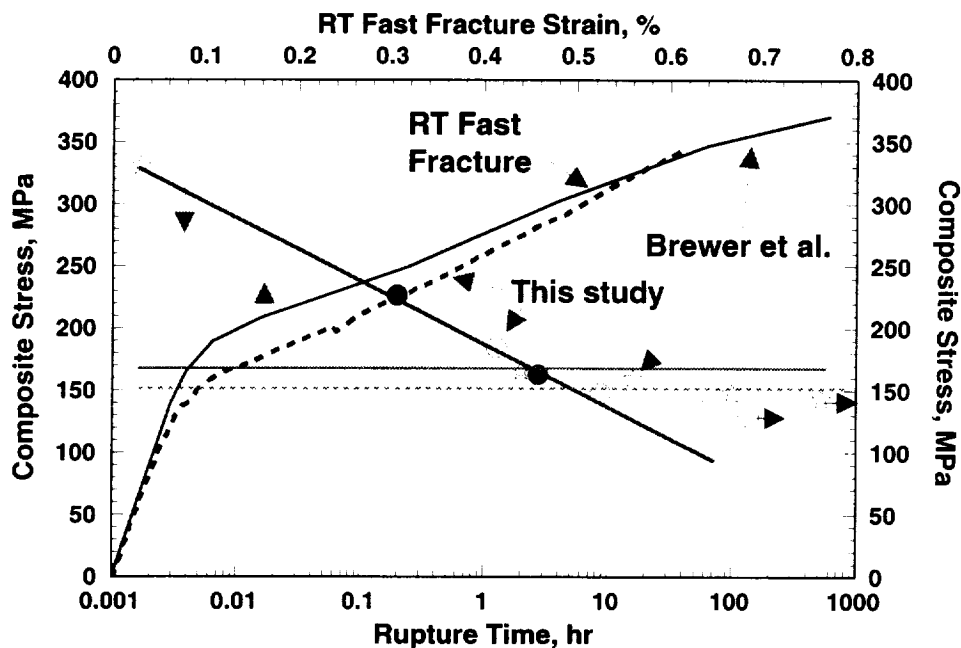


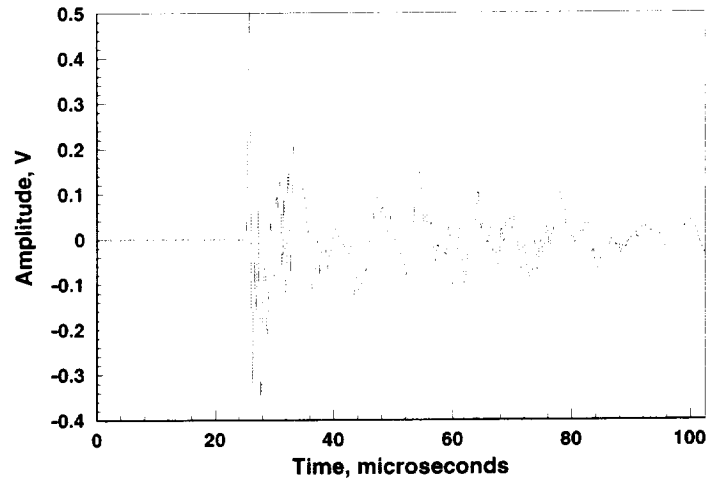
Figure 3.4: Room temperature and time dependent stress-rupture behavior of the two different Hi-Nicalon, BN interphase, MI SiC composites. For both samples tested at room temperature, failure occurred in the grips and not in the gage section. There is actually little difference in the ultimate properties of these two composites.

3.1.2 Acoustic Emission Data and Matrix Crack Spacing

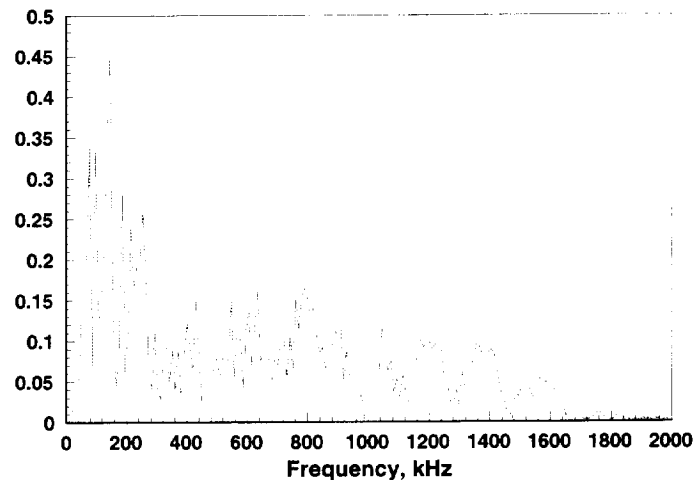
Modal AE was used to monitor the damage occurring along the length of the rupture specimens during the experiment. A typical waveform obtained during the stress-rupture test is shown in Figure 3.5. There are two unique characteristics to this waveform as compared to waveforms obtained during room temperature testing (Figure 1.2.4 and references 2 and 3). First, the waveform is extensional. This is not surprising since the sensors are attached "ends-on", i.e. not on the face, and the specimen is "clamped" in the grips and the specimen is unable to flex. Second, the waveform is not "symmetrical" about the abscissa after the first peak. This was surprising. It is surmised that this was due to interference of the front of the waveform with the rest of the waveform after the front of the wave reflected back from the edge. All of the waveforms possessed these two characteristics whether they were high or low energy events.

Two examples are shown in Figure 3.6 of the AE source locations plotted versus time for an experiment performed at 960°C and one performed at 815°C. The location was determined by the difference in times of arrival of the initial extensional wave portion of the AE waveform based on the accumulated damage (reduction in elastic modulus) [3].

For example, the location for Figure 3.6a was determined using a speed of sound 91% of that for the undamaged material based on the change in the speed of sound (difference in times of arrival) for the material subjected to the same applied stress at room temperature [2]. The speed of sound decreases with the square root of modulus as damage in the matrix is accumulated [3]. The speed of sound for the undamaged material and the approximated speed of sound used in the location determination were 9600 and 8740 m/sec, respectively. After the test, the speed of sound was determined along the length of the ruptured composite and was found to range from 8570 to 8820 m/sec, confirming the speed of sound approximation.



(a)



(b)

Figure 3.5: Typical (a) waveform and (b) fast Fourier transform (FFT) plot received with edge-on mounted sensors from fracture in furnace region of composite during rupture experiment.

The data was sorted out so that only events which occurred in the ± 30 mm region of the sample were analyzed. The data was also sorted out according to the energy of each AE event. The events with the two highest decades of AE energy are plotted separately and the events with the three lowest decades of AE energy are combined in Figures 3.6a and 3.6b. The load plotted in Figures 3.6a and 3.6b are the loads recorded by the AE computer when an event occurs. The apparent load fluctuations are not real but are the result of signal noise from the universal testing machine received by the AE computer through the analog input*.

* The AE computer was connected to the Instron through the connector for analog output. The load output that was conditioned, digitized, and received on a different computer showed no load fluctuations (see Figure 3.3). Therefore, an oscilloscope was tied into the same output from the Instron to the AE computer. It was found that a periodic, low frequency noise always occurred even when no load was applied. The peak amplitudes of this low frequency noise corresponded to the largest load fluctuations plotted in Figures 3.6a and 3.6b. This noise had no effect on the AE signals, which were received through different channels.

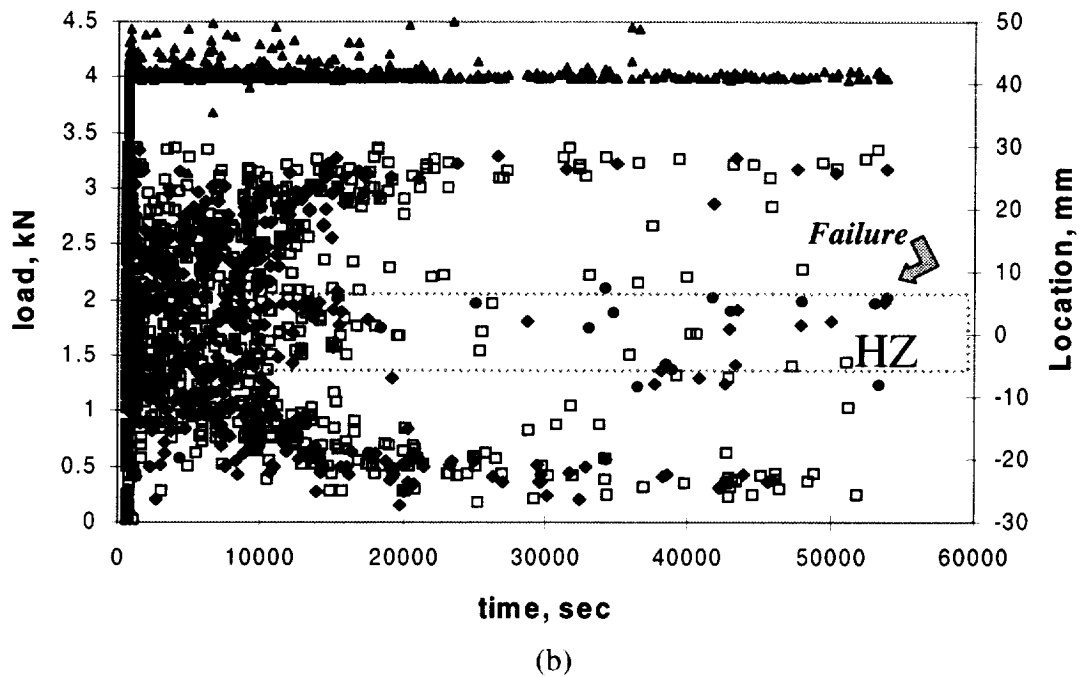
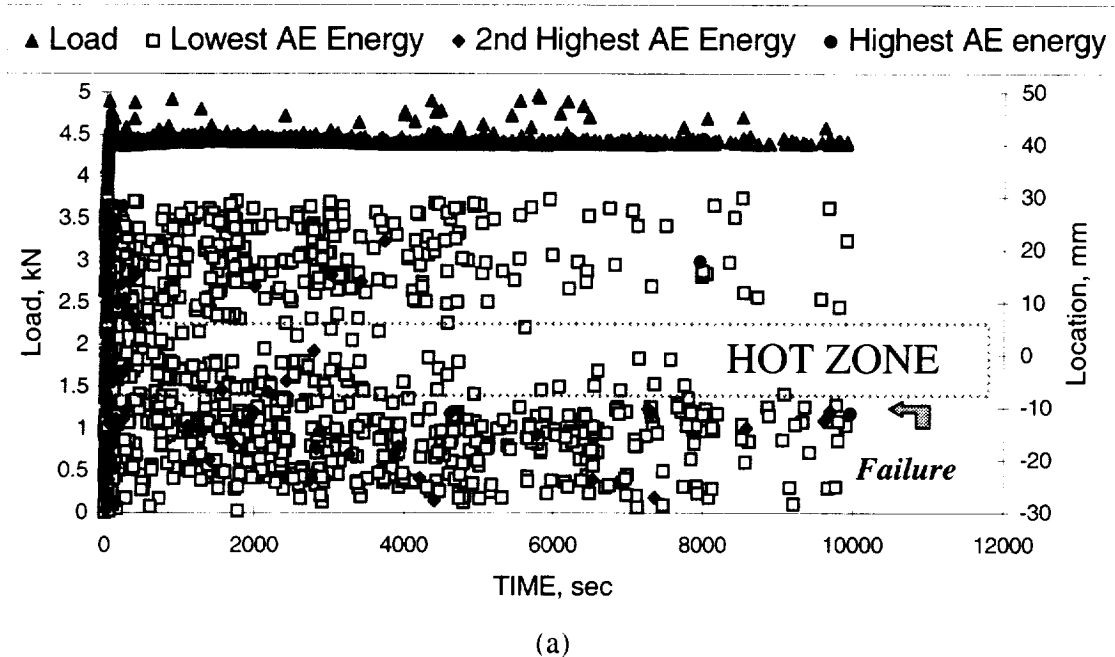


Figure 3.6: Load and AE event location versus time for (a) an applied load of 4.4 kN (160 MPa) at 960°C hot zone temperature and (b) an applied load of 4 kN (148 MPa) at 815°C hot zone temperature.

Several details are worth noting from the AE studies. For example, Figure 3.7 shows the cumulative number of events and cumulative AE energy from each event versus time for three different rupture experiments. For the lowest stress (Regime II) specimen, most of the AE events and the AE energy occurred after reaching the rupture load. For the highest stress (Regime I) specimen, most of the events and most of the AE energy occurred during loading. For the middle stress specimen (Regime I), most of the events occurred after loading whereas most of the energy occurred during loading. It is shown in Appendix A that matrix cracking correlates well with the largest energy events and not necessarily the number of events. Therefore, Regime I material was fairly well cracked prior to the set-load and some additional microcracking or fiber breaks occurred after loading whereas most of the cracking in the Regime II material occurred after the set-load was reached.

Second, the failure location was accurately predicted from the location analysis (final AE event) for both specimens as shown in Figure 3.6. In fact, the location of all four rupture specimens determined by the AE method were within ± 1 mm of the actual measured location. This confirms the accuracy of the AE source locations as pertaining to real physical phenomena. It is also clear that there were a number of high energy events for both specimens occurring at approximately the same location as the final failure event prior to the failure time. These high energy AE events are attributed to the formation of large cracks or the growth of existing cracks at that location.

Third, the location of damage is apparently temperature dependent based on the AE activity as a function of location, i.e. temperature profile. In Figure 3.6a, AE activity is significantly less in the hot zone (960°C) region after ~ 1000 seconds compared to the regions just outside the hot zone. Conversely, in Figure 3.6b, more AE activity occurs in the hot zone (815°C) region. Since both of the specimens tested at 960°C failed at $\sim 880^\circ\text{C}$, it can be concluded that this is the most severe embrittlement temperature for these composites when tested in air.

The crack density was determined for several ruptured composites. Figure 3.8 shows the temperature dependence of crack density as a function of length of two specimens tested at 960°C. It is evident that more cracking occurred in the 700 to 900°C exposed region of the composites than at regions exposed to higher or lower temperatures. The lower stress condition resulted in twice as many cracks in this region compared to the hot zone temperature region whereas the higher stress condition resulted in 50% more cracks in the 700 to 900°C exposed region compared to the hot zone exposed region. For specimens tested at 815°C, most matrix cracking occurred in the hot zone region (Figure 3.9). The matrix crack spacing is also shown in Appendix A to correlate well with the cumulated AE energy along the length of the specimen.

The matrix crack saturation density from a sample failed at room temperature was found to be 2.4 mm^{-1} . For 815°C tested specimens (Figure 3.9), this is the value reached by the specimen precracked at a high stress and the specimen tested at 185 MPa. The specimens tested at 148 and 140 MPa had more cracks in the hot zone regions of the furnace, but significantly fewer than the crack saturation limit. Very few cracks were observed for the 140 and 148 MPa samples at distances greater than $\pm 20 \text{ mm}$ on the specimen length. In fact for this region, no interior cracks were observed, cracks are only observed in the outer two plies. No cracks were observed at all for the 148 MPa specimen in the 35 to 45 mm range along the length. Perhaps no cracks existed in this section of polished composites. It is also possible that cracks could not be easily observed because they were not opened up due to the low applied stress condition, little time at temperature, and the low temperature for that region.

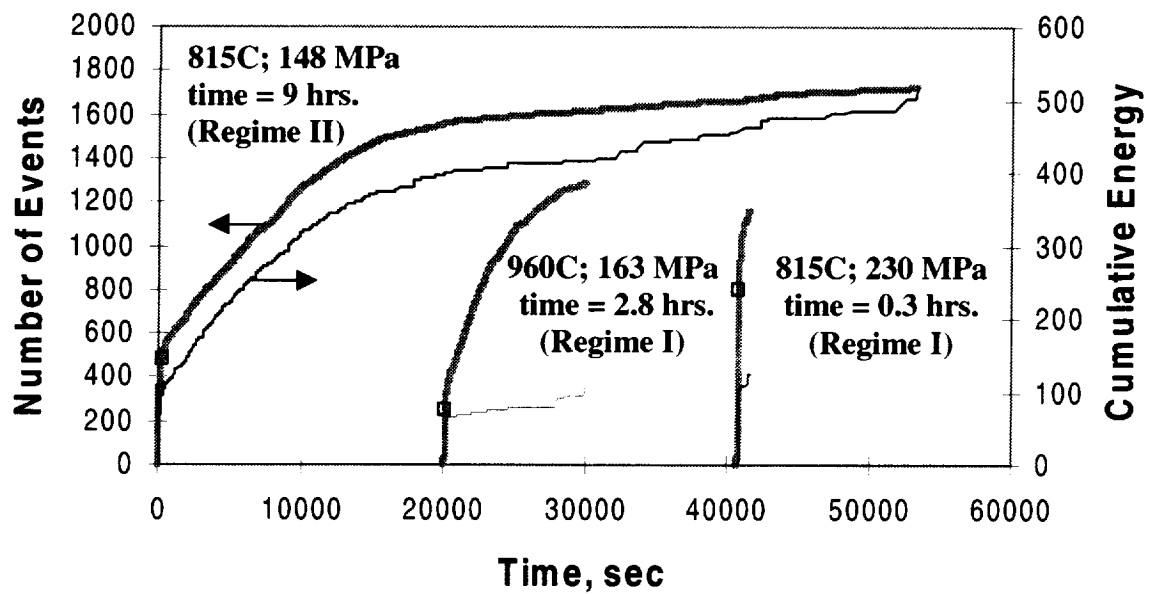


Figure 3.7: The cumulative number of AE events and cumulative AE energy as a function of time for three rupture specimens. The square on the “number of events” curves indicates the time at which the load reached the set-load for the rupture experiment. The two shorter time experiment data sets are offset on the time scale for clarity.

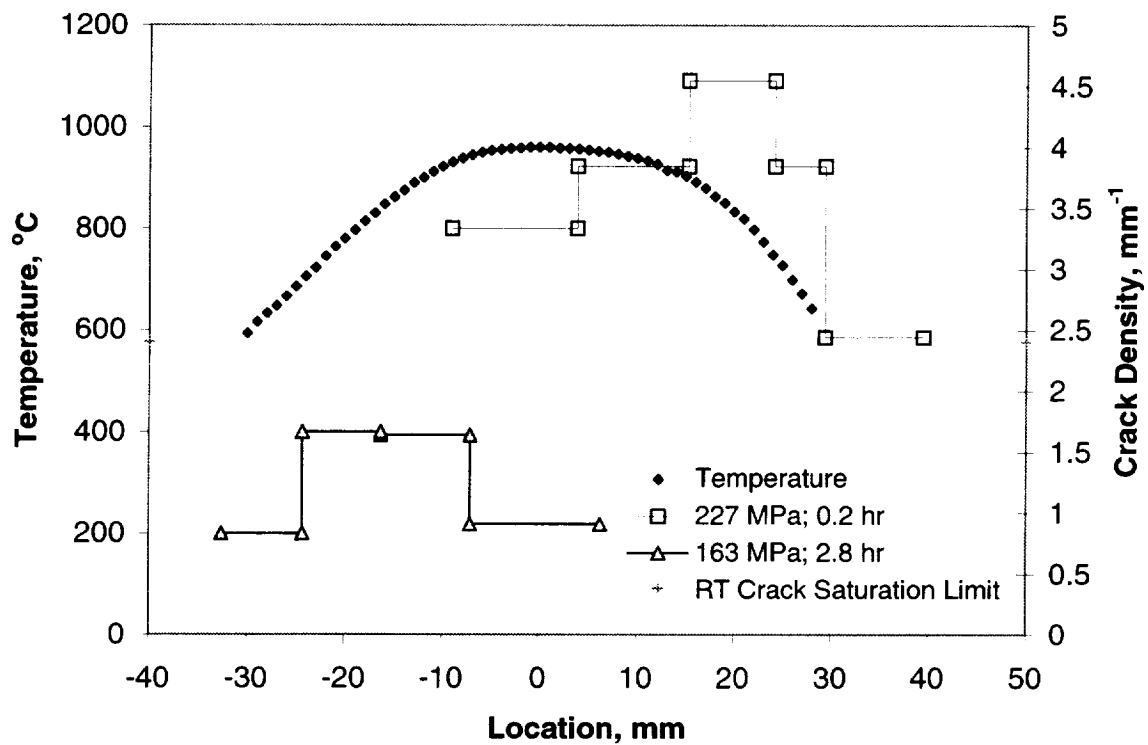


Figure 3.8: Measured matrix crack density for two samples tested at 960°C over the length of each sample as well as the furnace temperature profile as a function of length.

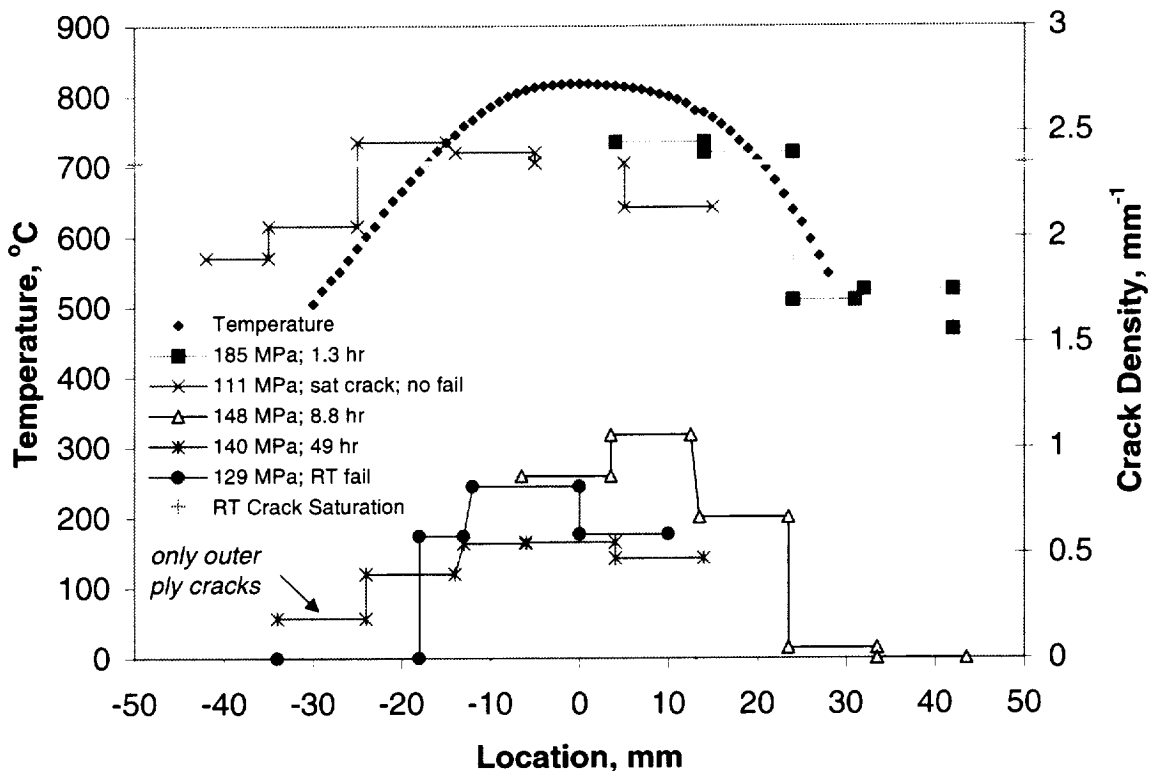


Figure 3.9: Measured matrix cracking for a sample tested at 815°C over the length of the sample as well as the furnace temperature profile as a function of length.

It was also observed, that for the hotter temperature regions of the 148 and 140 MPa specimens that cracks only penetrated three or four plies into the material. Sometimes, cracks emanating from both sides of the specimen would link up via a longitudinal crack. The specimen tested at 148 MPa that lasted for 100 hours from the reference 1 study also only showed cracks, for the most part, which start at the surface and penetrate only into the outer two plies.

There were only a couple of examples where a matrix crack had broken fibers, i.e. most fibers were bridging the cracks. The only specimen that showed many failed fibers in the matrix cracks was for the 227 MPa sample.

For the specimen tested at 227 MPa, a greater number of cracks were observed in the hot regions of the specimen than expected from the crack saturation density (Figure 3.8). This was the only specimen that showed this behavior. What caused this is not readily apparent. There was some crack branching observed where there appeared to be a several local cracks formed around a larger transverse crack in the load-bearing bundles. However, there were not enough of these to account for the higher crack density.

For both AE data sets plotted in Figure 3.6, there was considerable AE activity in the ± 25 to 30 mm regions of the samples. There is also considerable activity beyond these distances that had been removed from the data sets for the plots shown in Figure 3.6. This is especially pronounced for the longer time experiment (Figure 3.6b). For these regions, there was very little if any increase in the AE energy after the set-load was reached. Also, the matrix crack spacing in these regions were no greater than the matrix cracking closer to the gage section of the

composite. When compared to other tests performed at room temperature, it was concluded that this noise corresponded to microcracking, some possibly in the form of longitudinal cracking, associated with the bending stresses applied to the tensile bar fairly close to the grips and not due to any temperature/environment effect.

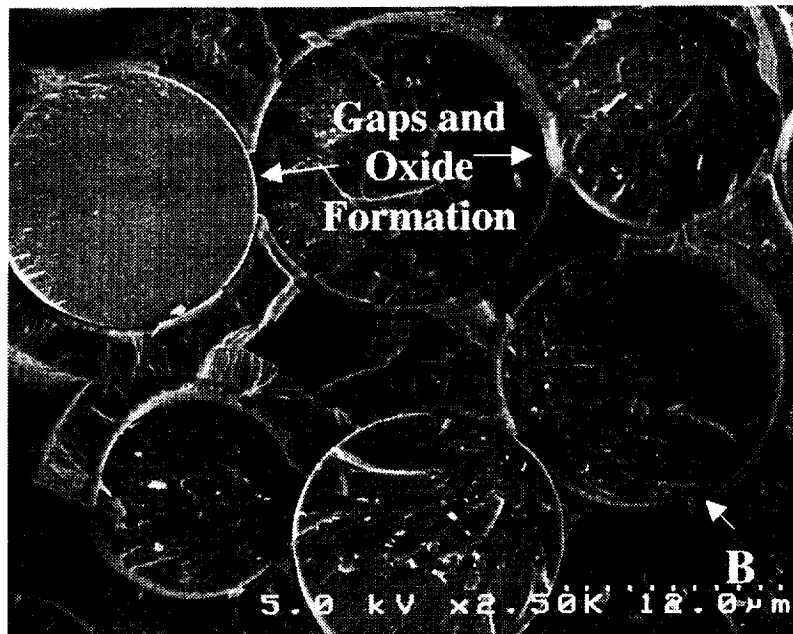
3.1.3 Microscopy of Composite Fracture Surfaces

Two representative fracture surfaces are shown in Figures 3.10 and 3.11 from Regimes I and II, respectively. The fracture surface of the Regime I tested specimen (Figure 3.10) is characterized by a “picture frame” type of appearance [14]. The outer layer of tows on the face and edges of the cross-section have little or no pull out whereas the interior fibers have all pulled out. The outer embrittled tows still have BN surrounding most of the fiber except where fibers are in near contact to one another (Figure 3.10b). The oxidation reactions occur first at the fiber/BN interphase probably enhanced by the presence of a thin carbon layer on the fiber surface resulting from the high temperature MI process temperature [4,5]. Since fibers are separated by only a fraction of a micrometer, the larger BN surface area exposed to the environment results in a greater amount of BN volatilization and oxide formation [6] in these near contact regions. Every fiber fracture mirror is observed to emanate from these near fiber contact regions (Figure 3.10b). A similar observation was made for Hi-Nicalon/BN/CVI SiC minicomposites tested at slightly higher temperatures (900 to 1050°C) [7,8] where fracture mirrors emanated from fiber-matrix bonds formed by the solidified oxidation product. For the fracture surface shown in Figure 3.10a, approximately ten tows were embrittled which corresponds to ~ 19 % of the load-bearing tows. For another sample tested at 165 MPa and a rupture time of 2.8 hours with the same type of picture frame appearance, eighteen tows were embrittled corresponding to ~ 34 % of the load-bearing tows.

The fracture surface for the low stress regime tested specimens (Figure 3.11) is characterized by a more jagged appearance. First, the fracture takes place on several different crack surface “planes” sometimes separated by up to 3 mm in the loading direction. Second, instead of forming a picture frame, it appears these smaller local cracks grew into the interior of the sample so that some interior bundles are embrittled while some surface bundles have fiber pull out. Figure 3.11b shows a fairly sharp transition in a single tow separating the embrittled fibers from the apparently pristine fibers. Figure 3.11c also shows a typical oxidized crack surface where borosilicate liquid/glass had formed to fill the interphase regions surrounding the fibers and the crack surfaces.



(a)

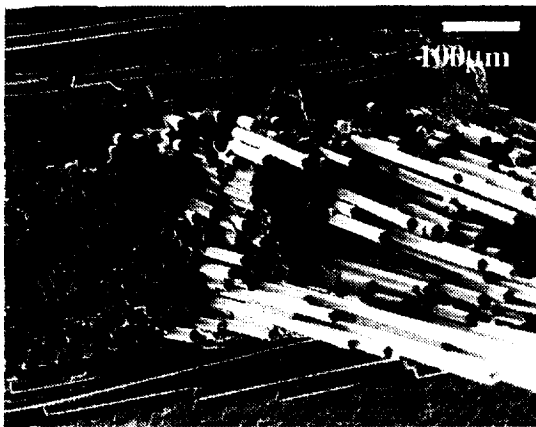


(b)

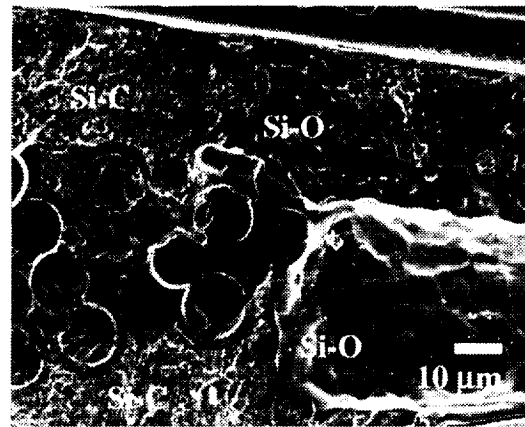
Figure 3.10: (a) Fracture surface of Regime I rupture fracture surface tested at 185 MPa and the rupture time was 1.3 hours. (b) Higher magnification region showing embrittled fibers.



(a)



(b)



(c)

Figure 3.11: (a) Fracture surface of Regime II rupture failure for fracture surface obtained from ref. 1. The applied stress was 160 MPa and the rupture time was 18.1 hours. (b, c) Higher magnification regions showing the oxidation front and region of pristine fibers.

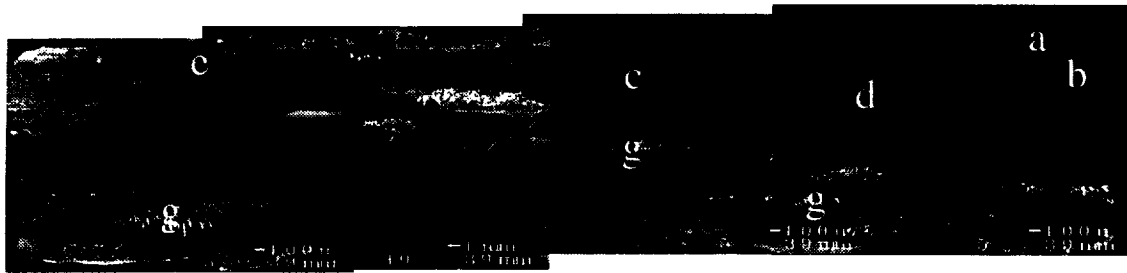
3.1.4 EDS Analysis

EDS was performed on individual fiber fracture surfaces from two composite fracture surfaces, one from Region I and one from Region II. The Region II composite fracture surface and EDS analysis are shown in Figure 3.12. EDS was performed on several fibers from seventeen different fiber bundles on the fracture surface. The O:C ratio peak height ratio from the EDS spectrum was calculated (Figure 3.12c). The data was organized according to the O:C peak height ratio and a map of the fracture was constructed based on relative O:C ratios. (Figure 3.12b).

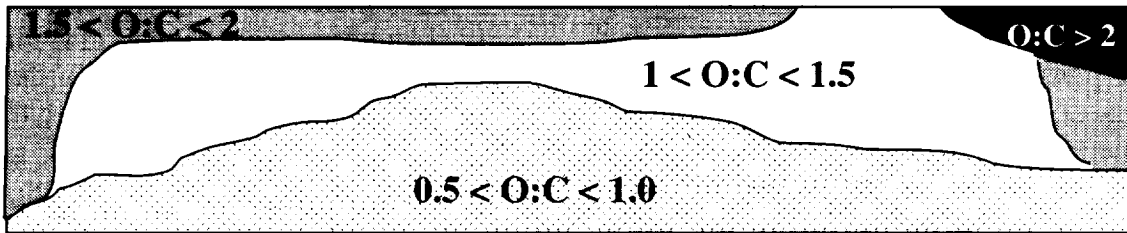
The pulled out fibers had the lowest O:C ratios which would be expected if the final failure event consisted of pulled-out fiber failure. For the embrittled fiber bundles, only one corner of the composite cross-section showed high O:C ratios indicative of a relatively thick SiO_2 scale and early fiber failure. The rest of the embrittled bundles showed higher O:C ratios than the pulled-out fibers, although not significantly higher. There does seem to be a consistent lowering of O:C ratio for the fiber bundles closer to the pulled out bundles. An arbitrary distinction is made in Figure 3.12b for regions of $1.5 < \text{O:C} < 2$ and $1 < \text{O:C} < 1.5$. The O:C ratio of the matrix surface around all of the embrittled bundles was on the order of 4 to 10 with the exception of a few regions where parts of a bundle (always less than ten fibers involved) appeared to be “sealed” by the oxidation product.

EDS analysis was performed on the fracture surface shown in Figure 3.10 (Region I). The time to failure for this specimen was only one hour. The O:C ratio for pulled out fibers was $\sim 0.25 \pm 0.01$ from three different bundles. The O:C ratio for embrittled fiber fracture surfaces ranged from 0.24 to 0.41 from seven different bundles. The O:C ratio for the matrix regions in and around the embrittled bundles ranged from 0.5 to 0.8. As with the Region II fracture surface, the pulled-out fibers had lower O:C ratios indicating they failed last. However, in this case there was only a small difference in O:C ratios between the pulled-out and embrittled fibers.

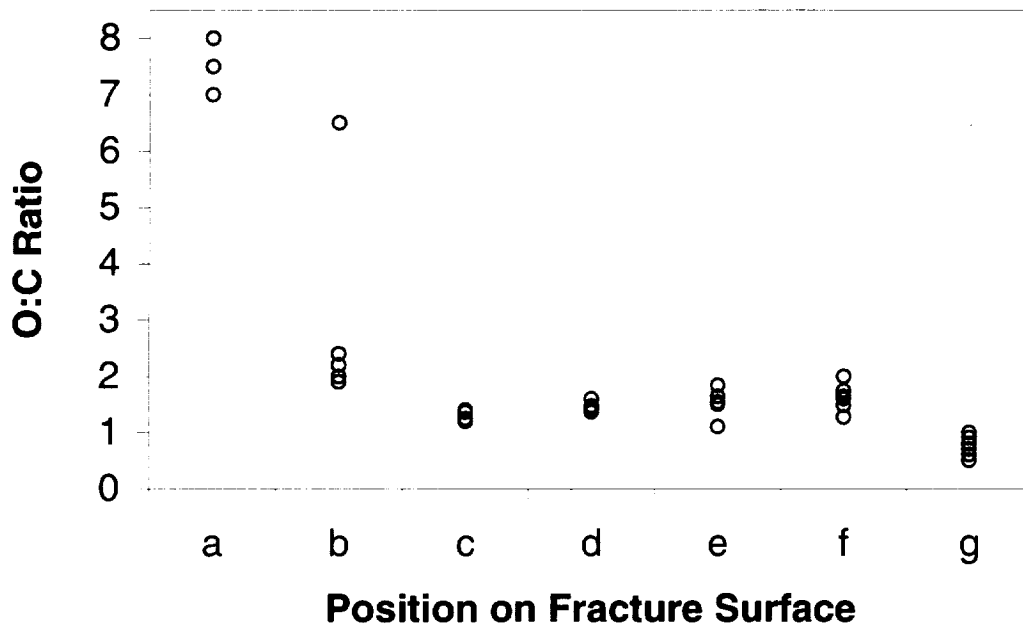
Therefore, it can be concluded that embrittled fiber failure occurred prior to pulled-out fiber failure. However, the time period between most embrittled fiber failure and pulled-out fiber failure was likely fairly short. The embrittled fibers must have been bridging the matrix cracks for considerable periods of time before failing. When the embrittled fibers did fail, the load they were carrying was shed onto the remaining fibers. In order to determine the criterion for fiber failure in the different regions of the composite fracture surface, fiber fractography was employed.



(a)



(b)



(c)

Figure 3.12: Fracture surface (a) of a specimen ruptured after 114 hrs and 148 MPa [1]. EDS was performed on individual fiber fracture surfaces to and the O:C ratio measured on 17 different bundles a some of which are shown in (c). A map was constructed based on the O:C ratios (b).

3.1.5 Fiber Fractography

The fracture mirrors of individual fibers were used to determine the relative (average) strengths of fibers on the ruptured composite fracture surfaces. Three groups of fracture surfaces were observed for each sample evaluated: embrittled fibers, pulled out fibers in the 2nd ply from the surface and pulled out fibers in the 4th ply from the surface (middle ply). Also, the fracture mirrors were determined for one of the room temperature tested tensile specimens.

The strength of the fibers, σ_f , is related to the mirror radius, r_c , by the relationship^[9-11]:

$$\sigma_f = A r_c^{-1/2} \quad (3.1)$$

where A is the fracture mirror constant. The data was to be compared on a relative stress basis, i.e. the tensile rupture stress divided by the room temperature ultimate tensile stress. For this reason, the magnitude of A is immaterial (assuming A is the same at room temperature and 815°C) and only the mirror radius needs to be determined. The normalized rupture stress from fracture mirrors was determined from the relationship:

$$\sigma_{fm(T,t)}/\sigma_{fm(RT)} = \{r_{c(R.T.)/r_{c(T,t)}}\}^{1/2} \quad (3.2)$$

where r_c is the radius corresponding to a 62.4% probability to failure, (T,t) refers to the rupture condition, and (RT) refers to room temperature. At least forty fibers were used for each distribution.

Probability plots from the fiber fracture mirror data for the fracture surface shown in Figure 3.10 are shown in Figure 3.13. The data is plotted as $\ln(r_c^{-1/2})$ rather than as $\sigma_{fm(T,t)}$. Figure 3.13a was the only probability plot that showed a difference in Weibull modulus, m , for the three distributions from the same fracture surface. For the other fracture surfaces, the m values varied between 2 and 4 but for a given fracture surface there was not much difference in m between the embrittled or pulled out fibers (Figure 13b). The room temperature m value was found to be 3.7. Lara-Curzio et al. [12] has shown that it is important to know the fiber area pertaining to the stress at which each fiber failed to determine accurate Weibull moduli data. Otherwise, reasonable differences in the distribution of fiber areas could lead to factors of 4 differences in the Weibull moduli when assuming a constant fiber diameter. This would be impossible for this study since the exact load each fiber failed at is unknown; however, the differences in fiber diameters can be greater than a factor of two (Figure 3.10b). Therefore, the Weibull modulus data is of limited utility. However, Lara-Curzio et al. [12] did show that the strengths determined from Weibull plots are not affected by the difference in fiber areas. Therefore, the fractographic analysis will concentrate on the relative strength data of the fiber distributions.

The results for four different fracture surfaces are shown in Figures 3.14 and 3.15 for two Regime I and two Regime II specimens, respectively. For all of the samples observed, the pulled out fibers showed the same strength properties regardless of the ply, so they are grouped together.

For both sets of data, the embrittled fibers fail at approximately 70 to 80% of the room temperature ultimate strength. However, there is a dramatic difference in the failure strength of the pulled-out fibers between the two different rupture regimes. Pulled out fibers for Regime I composites fail at an even lower stress (~ 65% of the room temperature strength) than the embrittled fibers. Pulled out fibers for Regime II composites fail at approximately the same strength as the room temperature failed fibers. It is evident that *a different failure criterion for the pulled-out fibers controls the different rupture regimes.*

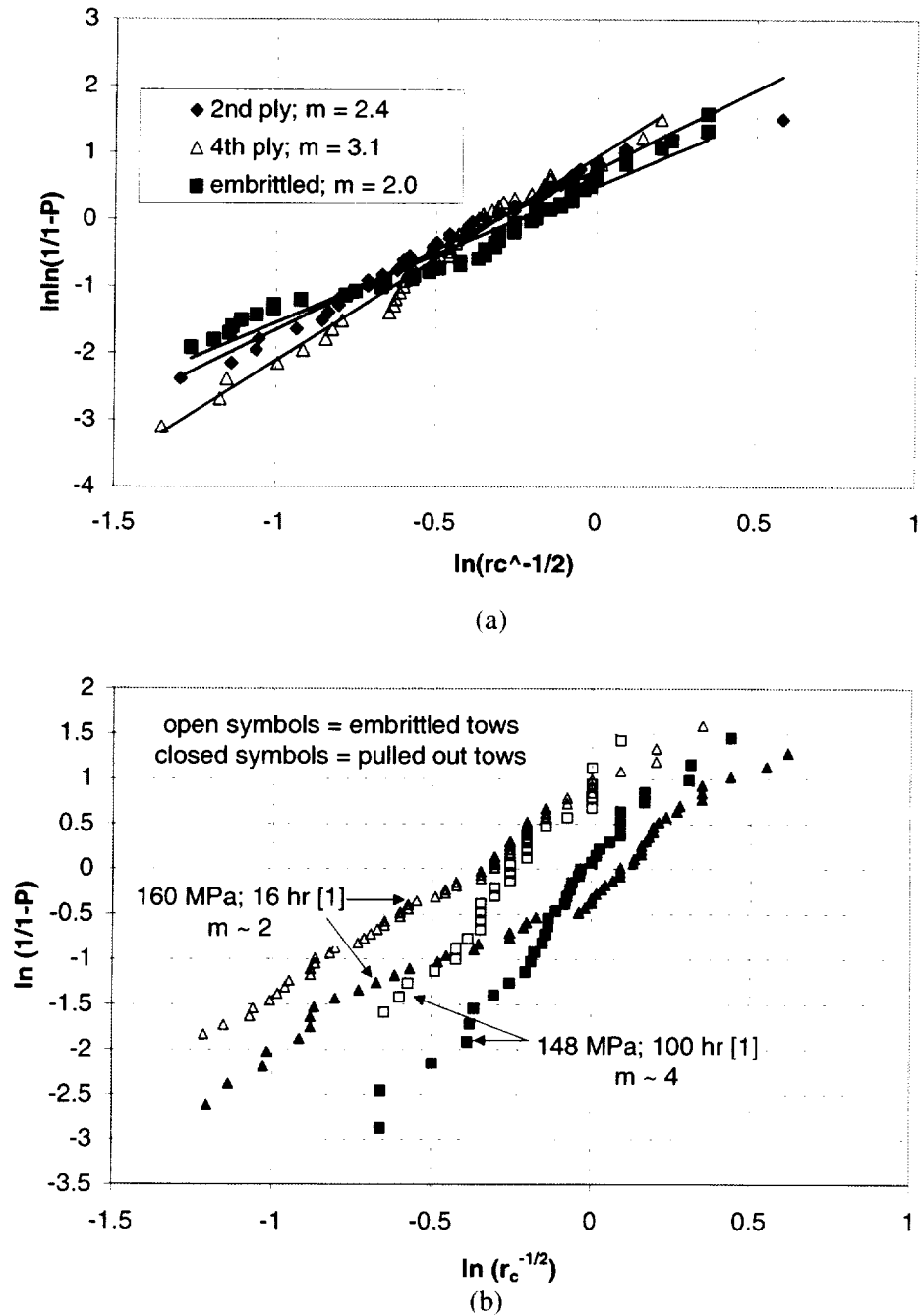


Figure 3:13: Weibull probability plots for fiber fracture mirrors from fracture surface of specimen that was ruptured (a) after 1.1 hours at 815°C and 185 MPa and (b) after longer times at 815°C.

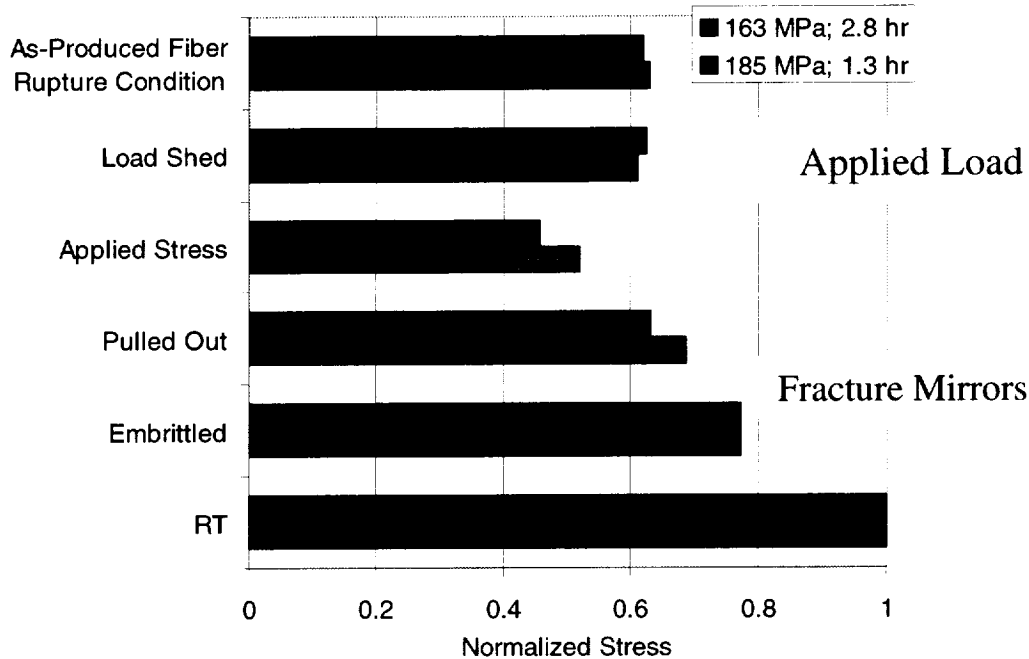


Figure 3.14: Bar charts of the normalized stress as determined from the fracture mirror analysis for two Regime I rupture specimens. Also plotted is the normalized applied stress, the normalized stress from the load shed by the embrittled fibers, and the Larson-Miller condition for fiber failure[13].

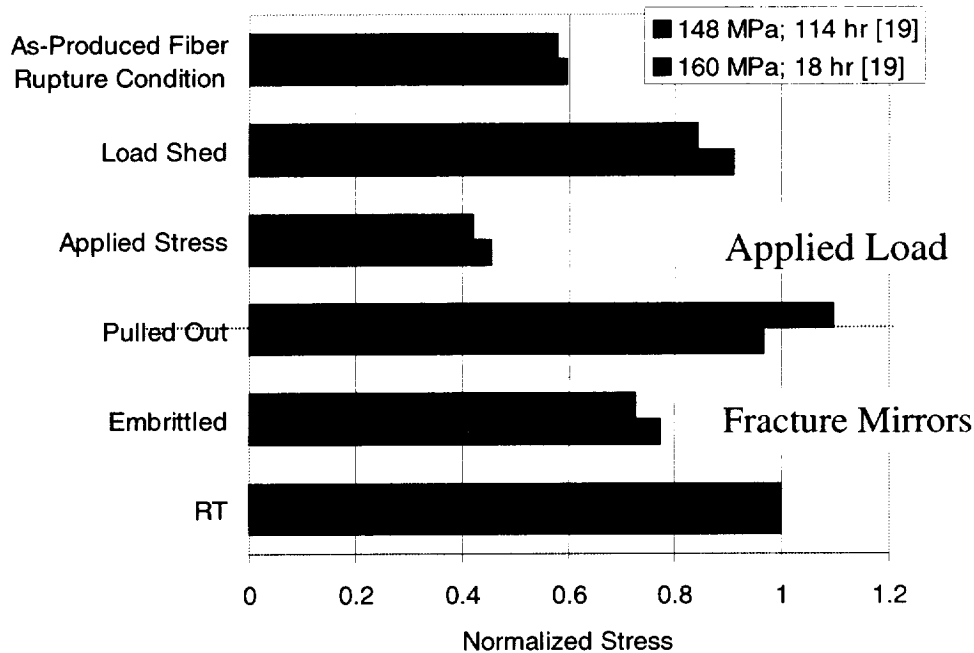


Figure 3.15: Bar charts of the normalized stress as determined from the fracture mirror analysis for two Regime II rupture specimens. Also plotted is the normalized applied stress, the normalized stress from the load shed by the embrittled fibers, and the Larson-Miller condition for fiber failure [13].

To understand these strength levels, also plotted in Figures 3.14 and 3.15 are the normalized average fiber stresses corresponding to the applied rupture load. These include the applied stress, the stress on the pulled-out fibers if the embrittled fibers failed first (load-shed stress), and the rupture stress condition for individual as-produced Hi-Nicalon fibers at the same time-temperature condition [13]. To determine the load-shed to the pulled-out fibers, the number of tows that were embrittled on the composite fracture surface was estimated as explained above and the load those tows would have carried was added to the applied load of the pulled-out tows. The rupture stress condition for individual as-produced fibers as determined by Yun and DiCarlo [13] is shown in Figure 1.1 as a Larson-Miller plot. The time, temperature regime that corresponds to this study would correspond to Larson-Miller parameters in the range 22800 to 27000 and are shown in graphical form as the “L-M Condition” on Figures 3.14 and 3.15.

Several observations can be made from comparing these stress conditions with the actual measured fiber strengths:

1. The failure stress of all the composites (applied stress) was significantly lower than the expected rupture stress for Hi-Nicalon fibers if the fibers were carrying all of the load in the matrix crack (L-M Condition).
2. The embrittled fibers appear to fail at stresses slightly higher than the as-produced fiber rupture criterion (L-M Condition).
3. For Regime I, after the load is shed onto the pulled-out fibers, the load-shed stress is about equal to the Hi-Nicalon L-M Condition stress. Both stresses are in good agreement with the measured (fiber fracture mirrors) normalized strength of the pulled-out fibers for Regime I materials.
4. For Regime II, after the load is shed on the pulled-out fibers, the load-shed stress is much higher than the Hi-Nicalon L-M Condition criterion, even approaching the ultimate strength of as-produced fibers. This load-shed stress is in good agreement with the measured (fiber fracture mirrors) normalized strength of the pulled-out fibers for Regime II material.

Two conclusions can be drawn from these observations. First, since the embrittled fibers fail first, their apparent “strength” is due to the local bonding of the fibers to one another because of the oxidation product formation. Similar to the minicomposite results [7], the fibers are probably weakened slightly by the stress-condition and oxidation reactions; however, they are also strongly bonded to one another resulting in shorter gage lengths and local stress-concentrations, i.e. correlated fiber failure. As with minicomposites [7], the weak fibers fail after some time at temperature. The load from these fibers is shed locally [14] rather than globally due to the interphase condition resulting in the progressive and probably rapid failure of all the embrittled fibers in the matrix crack.

Figure 3.10b shows a group of fibers where each fiber is in close contact (less than 100 nm) to at least one other fiber. The close contact is due to the tightness achieved during the weaving operation and pressure applied to the weave, to maintain dimensional stability of the panel, during CVI BN infiltration [15]. In order to quantify the extent of fiber-to-fiber contact, an as-produced composite was polished and the groupings of fibers were determined for individual tows from a surface ply, the second ply from the surface, and the center ply (fourth ply from the surface). The results are given in Table 3.2.

Table 3.2: Fiber grouping from different bundles of an as-produced MI-composite.

	Number of fibers (fraction of fibers) In a Given Group of Fibers		
	<i>Surface Ply</i>	<i>2nd Ply In</i>	<i>4th Ply In</i>
no-touch	24(.048)	22(.044)	22(.044)
in pairs	16(.032)	18(.036)	16(.032)
in triples	9(.018)	9(.018)	9(.018)
in groups < 10	103(.206)	84(.168)	68(.136)
in groups < 20	172(.344)	123(.26)	100(.2)

A group was defined as the number of fibers that were in close contact to at least one other fiber from the same group. The groups are categorized according to a single-fiber (no-touch) group, two-fiber group, three-fiber group, less than 10-fiber group, and less than 20-fiber group. There are few fibers from a 500 fiber count bundle that are in groups of only a few fibers. In fact, about two-thirds of a surface tow have fibers in groups of 20 or more. Groups containing 20 or more fibers are even more prevalent for the more interior located bundles.

If fiber failure is correlated, in the embrittled regions, with the failure of a neighboring fiber, then large portions of a load-bearing tow, if not the entire tow, could fail immediately after the failure of a single fiber in a large group of fibers. This nearly instantaneous, progressive failure could also be extended to neighboring tows in the same microcrack.

Second, for Regime I conditions, the fibers which have not been exposed to the environment are still being loaded and are weakening according to the intrinsic degradation mechanisms operating at the stress/temperature/time conditions [13] since the matrix cracks are through-thickness. For Regime II conditions, microcracks must grow into the material in order for new fiber bundles to be exposed to the environment and for the fibers to be fully loaded. The loading of the fibers in the uncracked regions where fibers have not been exposed to the environment would be a fraction ($\sim 1/3$ based on the rule of mixtures) of the loads applied to fully loaded fibers bridging a matrix crack since the matrix is sharing the load.

3.1.6 Retained Strength of Rupture Specimens Which Had Not Failed

Two composite specimens did not fail after 138 hours at 815°C. One had been precracked at 227 MPa and held at constant stress of 111 MPa. The other specimen was loaded to and held at 129 MPa for the duration of the experiment. Both of these specimens were later loaded in tension to failure at room temperature. The precracked specimen failed at 109 MPa just outside the hot zone region. The non-precracked specimen failed at 81 MPa in the hot zone region of the specimen. Both specimens failed at lower stresses than the stress that had been applied at temperature. There was very little non-linear stress-strain behavior or acoustic emission activity for either specimen.

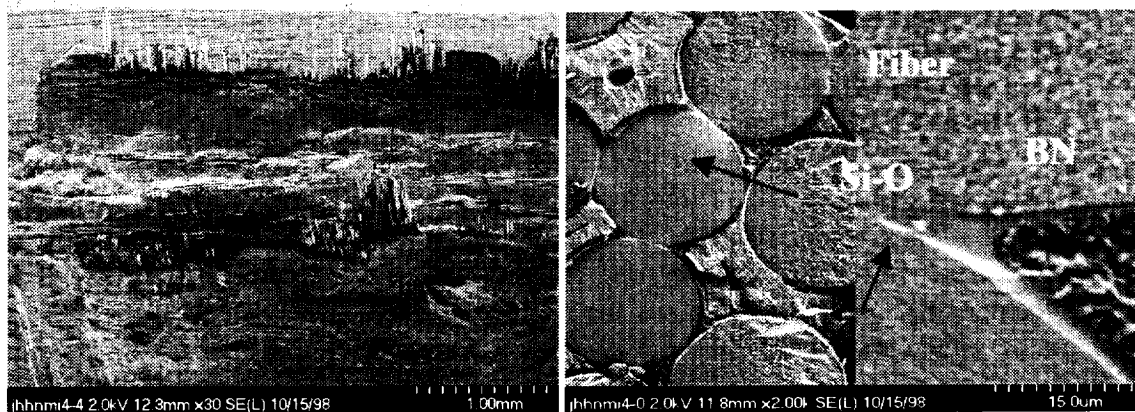
For the non-precracked specimen, there was little fiber pullout on the fracture surface (Figure 3.16a). The only fiber pullout existed at eight of the bundles near the surfaces of the specimen. Almost all of the embrittled bundles only showed minor amounts of interphase oxidation (Figure 3.16b) which always occurred at the fiber-to-fiber contact points. The BN around the rest of the fiber was almost always present except for a few bundles near the surface of the composite.

From EDS analysis, the matrix failure crack surface contained no oxygen, indicating that most of the failure crack did not propagate along an existing matrix crack. Even though fiber-bridged cracks were observed (after the experiment) to have traversed through half of the composite thickness elsewhere on the sample. Two matrix fracture surface locations were oxidized within fiber bundles. One region near an edge and the other near a face surface. It is apparent that the failure crack started at an existing crack but propagated in a relatively planar fashion (compared to rupture fracture surfaces) through previously uncracked but embrittled fiber bundles.

The fiber-bundle embrittlement came from oxidation along the length of the fibers in between the fiber/BN interface where a thin carbon layer resides as a result of fiber decomposition from matrix processing [4,5]. This "pervasive" oxidation is most prevalent at the near fiber-to-fiber contact regions (Figure 3.16b) because of the increased surface area for BN oxidation after the initial oxidation of carbon [5]. However, a thin oxide layer was observed to exist in between the fiber and the BN where the fibers were not in contact (Figure 3.16c) throughout the fracture surface.

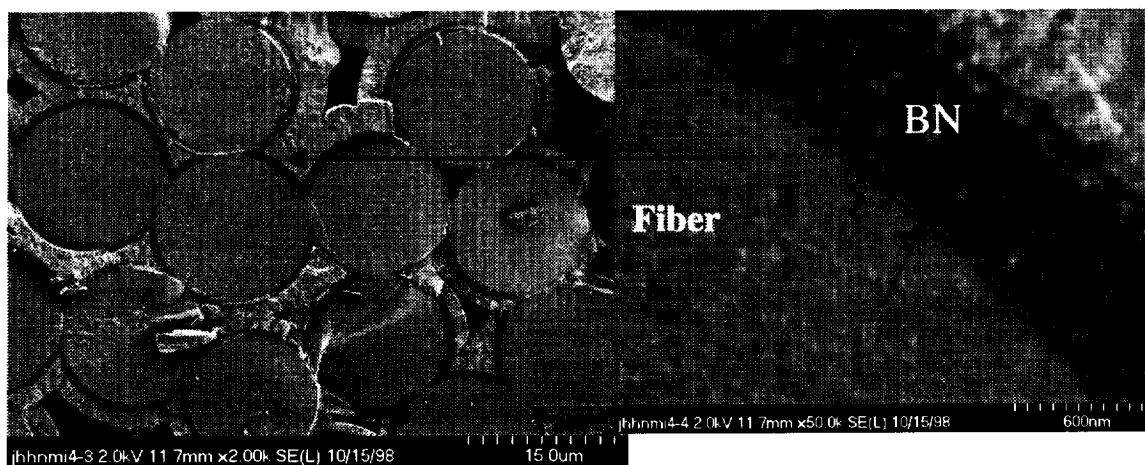
Ogbuji [5] observed this kind of "pervasive" oxidation for uncracked specimens subjected to a burner rig condition (800°C, 10% H₂O, 105 m/sec, 1 atm). Ogbuji also showed that for specimens exposed to lower and higher water vapor contents in a tube furnace that little if any "pervasive" oxidation occurred for these composites. For burner rig conditions, oxidation of the 0° bundles occurred through the exposed 90° bundles. For the case of this study, it is believed that the 0° oxidation occurs through the exposed 0° fibers at a matrix crack some distance away from the failure crack at room temperature.

For the precracked specimen very similar features were observed except that no fiber pull-out was observed and that most of the matrix was oxidized, i.e. the failure crack propagated along an existing matrix crack. The region where failure occurred corresponded to an exposure temperature of ~ 770°C. Still, most of the BN was present around a fiber and all of the fiber-to-fiber contact locations were oxidized and were the source for fiber fracture mirrors.



(a)

(b)



(c)

Figure 3.16: SEM micrographs of specimen tested after rupture conditions at room temperature. (a) Some pull-out occurred on some of the outer tows. (b) Most of the bundles showed no pull-out and oxide formation at the near fiber-to-fiber contact regions and in between the BN and the fiber (c).

3.2 Chemical Vapor Infiltration Composite Rupture

Although a thorough study of CVI-matrix composite rupture was not performed in this study, the data from Brewer et al. [1] and the test performed in this work are added to the results for comparison with the MI-matrix composite rupture.

3.2.1 Stress-Rupture Data

Figure 3.17 shows the rupture, LCF, and fast fracture data for CVI-matrix composites and MI-matrix composites (Figure 3.1). Table 3.3 lists all of the CVI-matrix rupture, LCF, and fast fracture data. The fast fracture strength of the CVI-matrix composite was significantly higher than the MI-matrix composite; however, the rupture properties were slightly worse than the MI-matrix composites. Figure 3.18 shows the rupture data and room temperature stress-strain behavior on the same curve. The onset of a lower rupture rate regime occurs at a stress of ~ 140 MPa which corresponds to a stress above the “knee” in the stress-strain curve. This is different than what was observed for the MI-composites (Figure 3.4) where the transition to a lower rupture rate regime occurred just prior to the “knee” in the stress-strain curve.

Table 3.3: CVI-Matrix Stress-Rupture, LCF and Fast Fracture Results.

Applied Stress, MPa	Hot Zone Temperature, °C	Time to Failure, hr	Failure Temperature, °C	Applied Load, kN
<i>Stress-Rupture Results</i>				
186	815	0.8	815	4.5
405	25	Fast Fracture	25	
<i>LCF and Fast Fracture Results From Reference 1</i>				
139	815	2	815	~3.4
130	815	8	815	~3.1
114	815	201	815	~2.8
111	815	391	815	~2.7
413	815	Fast Fracture	815	
420	25	Fast Fracture	25	

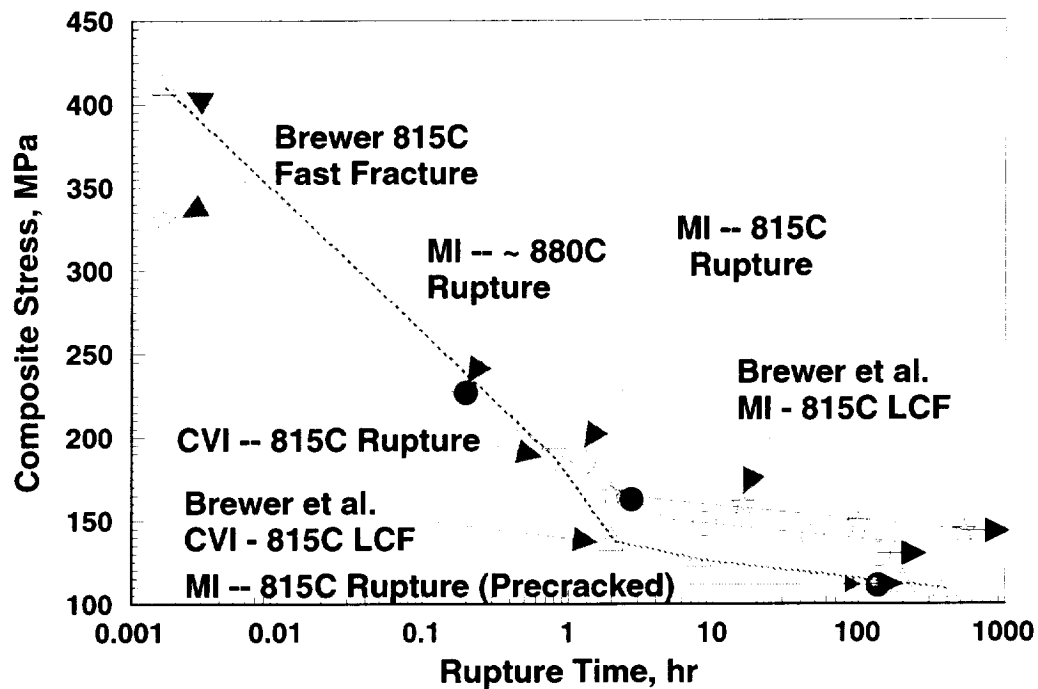


Figure 3.17: CVI matrix and MI matrix (Figure 3.1) composite stress-rupture data from this study and LCF data from ref. 1 plotted versus time. Also plotted is the 815°C fast fracture strength of the composites tested in ref. 1.

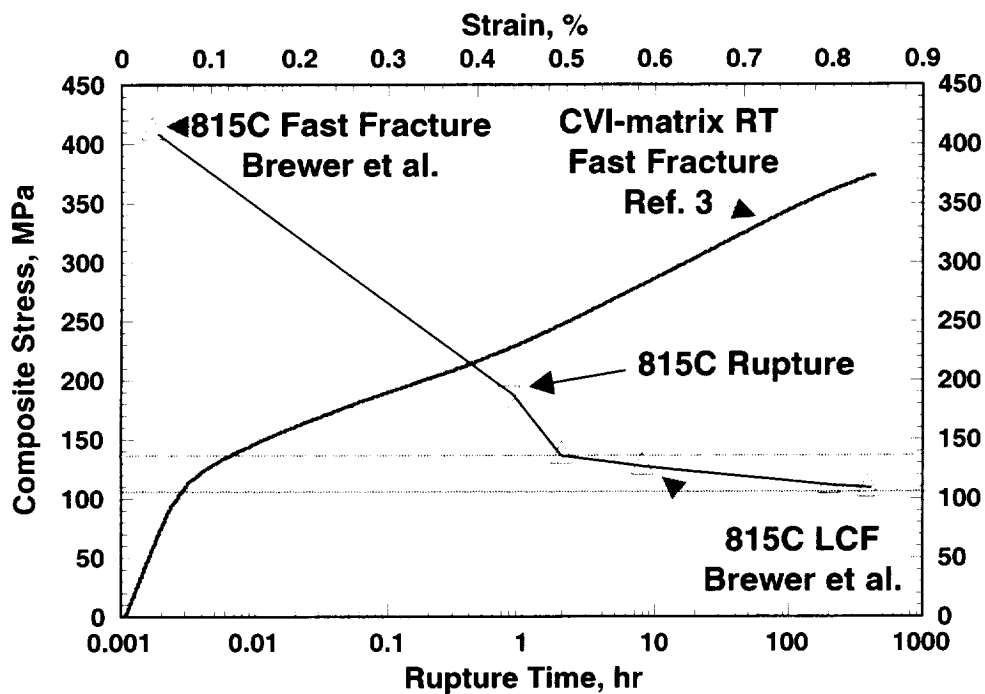


Figure 3.18: Room temperature and time dependent stress-rupture behavior of Hi-Nicalon, BN interphase, CVI SiC composites.

Figure 3.19 shows the stress-strain behavior of the 185 MPa stress-rupture specimen and the room temperature stress-strain curve. The initial part of the stress-strain curves is identical, however for stresses higher than the knee in the stress-strain curve, greater strains are recorded for the stress-rupture specimen. Since the stress-rupture specimen was loaded at 815°C at a fairly slow rate, it is surmised that the excess strain accumulated on loading is due to the reaction of the environment with the BN.

3.2.2 Acoustic Emission Data

The AE location and stress versus time for the ruptured CVI-matrix composites are shown in Figure 3.20. For this high stress test, very little AE activity occurred after the rupture load was reached. The final event, which occurred in the hot zone region, was an order of magnitude louder than the next loudest event. The location of the failure event was again determined from the difference in the arrival times for the final event on the two sensors and was only 1 mm from the measured location.

3.2.3 Microscopy of Composite Fracture Surfaces

The fracture surface of the highest stress, shortest time rupture specimen is shown in Figure 3.21. Most of the fracture surface was characterized with fiber pullout. There were a few tows that were embrittled (Figure 3.21b). However, most of the tows were characterized with embrittlement of some of the outer fibers (no pullout) in a tow and significant pullout for most or some of the inner fibers in a tow (Figure 3.21 c and d).

For the fibers that were embrittled, many of the fiber fracture mirrors emanate from near fiber-to-fiber contact points (Figure 3.21 e and f) similar to the MI-matrix composites. An oxidation product was observed to fuse the fibers together even though most of the BN interphase remained. Also, the presence of gaps or holes near the fiber-to-fiber contact points observed on the MI-matrix rupture surface (Figure 3.10b) were absent for the CVI-matrix rupture surface. For embrittled fibers, a very noticeable rim of oxidation product was observed between the fiber and BN interphase for all of the embrittled fibers (Figure 3.21g). For MI-matrix composite tested under similar conditions (Figure 3.10) there was a gap which existed between the fiber and the interphase.

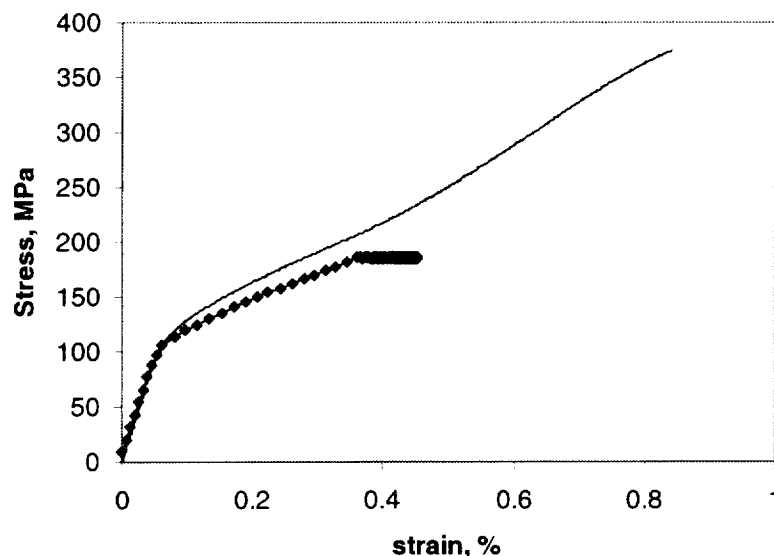


Figure 3.19: Stress-strain behavior of material tested at room temperature fast fracture and the rupture test.

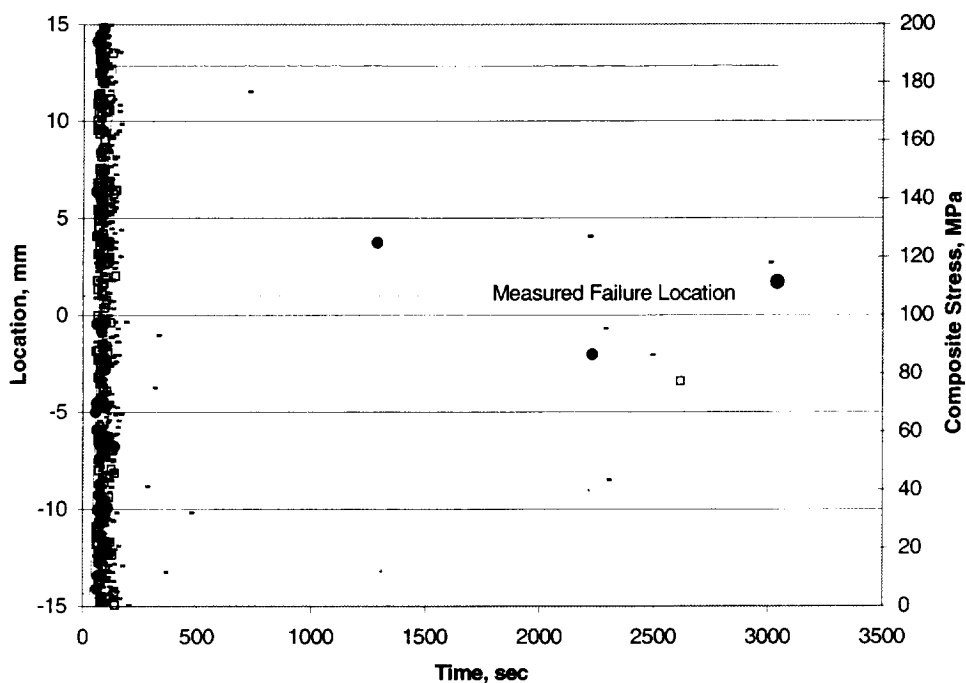


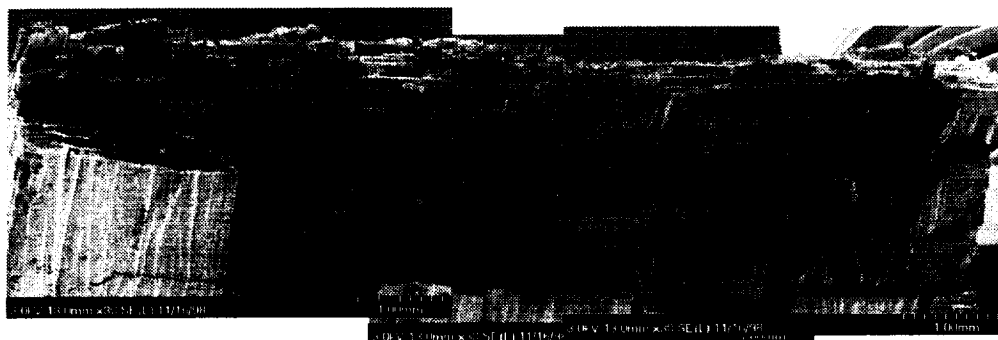
Figure 3.20: Stress and AE event location versus time for 186 MPa, 815°C stress-rupture test.

In addition, there appeared to be a greater number of embrittled fibers, compared to MI-matrix composites, that were not intimately contacting another fiber (Figure 3.21g) or that were bonded to another fiber but had a fracture mirror which did not emanate from a fiber-to-fiber contact point (Figure 3.21e). The fiber grouping statistics for the CVI-matrix composite was determined from an as-produced composite (Table 3.4) which do show a significantly greater number of fibers not touching other fibers or in smaller groupings compared to the MI-matrix composite (Table 3.2). These non fiber-to-fiber failure sites appear to be due to the thin oxide layer formed between the fiber and the BN interphase.

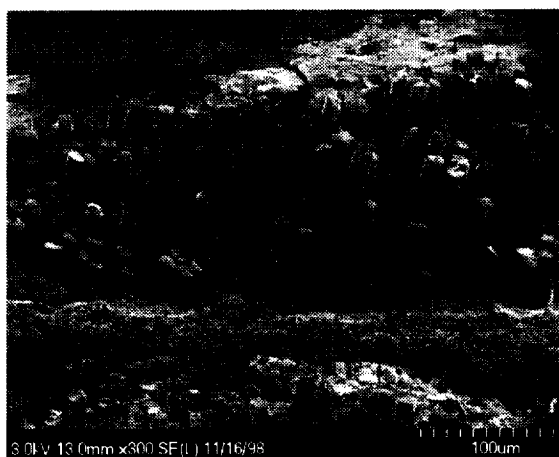
Within two hours, most of the fibers have been embrittled through the entire thickness of the CVI-matrix rupture specimen (Figure 3.22a). Only a few fibers pullout for this sample. There are varying degrees of oxidation, in some regions interphase recession is evident and greater amounts of oxide product formation (Figure 3.22b) whereas in other regions the oxidation is the same as that described for the shorter time rupture specimen (Figure 3.22c).

Table 3.4: Fiber grouping from different bundles of an as-produced CVI-composite.

	Number of fibers (fraction of fibers) In a Given Group of Fibers		
	<i>Surface Ply</i>	<i>2nd Ply In</i>	<i>4th Ply In</i>
no-touch	68(.136)	37(.074)	74(.148)
in pairs	38(.076)	28(.056)	68(.136)
in triples	72(.144)	21(.042)	27(.054)
in groups < 10	281(.562)	184(.368)	238(.476)
in groups < 20	324(.648)	266(.532)	321(.642)



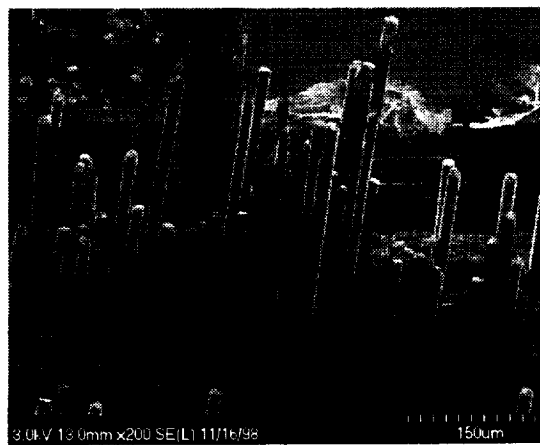
(a)



(b)



(c)



(d)

Figure 3.21: FESEM micrographs from CVI-matrix rupture (186 MPa; 0.8 hr; 815°C).



(e)

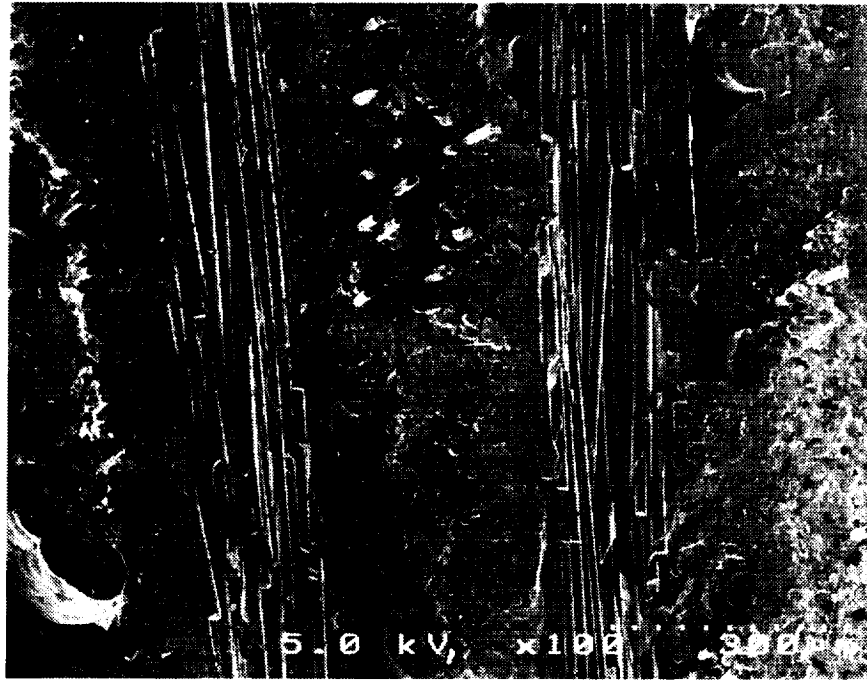


(f)



(g)

Figure 3.21: Continued.



(a)



(b)

Figure 3.22: FESEM micrographs from CVI-matrix rupture (139 MPa; 2 hr; 815°C).



(c)

Figure 3.22: Continued.

3.3 Works Cited

1. D. Brewer, A. Calomino, and M. Verilli, unpublished research.
2. G.N. Morscher and J.Z. Gyekenyesi, "Room Temperature Tensile Behavior and Damage accumulation of Hi-Nicalon Reinforced SiC Matrix Composites," *Ceram. Eng. Sci. Proc.*, **19** [3] 241-249 (1998).
3. G.N. Morscher, "Modal Acoustic Emission of Damage Accumulation in a Woven SiC/SiC Composite," *Comp. Sci. Tech.* **59** 687-697 (1999).
4. J.J. Brennan, unpublished research.
5. L. Thomas-Ogbuji, "A Pervasive Mode of Oxidative Degradation in a SiC-SiC Composite," *J. Am. Ceram. Soc.*, **8** [11] 2777-84 (1998).
6. N.S. Jacobson, G.N. Morscher, D.R. Bryant, and R.E. Tressler, "High Temperature Oxidation of Boron Nitride Part II: BN Layers in Composites," *J. Am. Ceram. Soc.*, **82** [6] 1473-82 (1999).
7. G.N. Morscher, "Tensile Stress Rupture of SiCf/SiCm Minicomposites with Carbon and Boron Nitride Interphases at Elevated Temperatures in Air," *J. Am. Ceram. Soc.*, **80** [8] 2029-42 (1997).
8. G.N. Morscher, "The Effect of Static and Cyclic Tensile Stress and Temperature on Failure for Precracked Hi-Nicalon/BN/CVD SiC Minicomposites in Air," *Ceram. Eng. Sci. Proc.*, **18** [3] 737-745 (1997).
9. J.F. Jamet, D. Lewis, and E.Y. Luh, "Characterization of Mechanical Behavior and Fractographic Observations on Compoglas SiC/LAS Composites," *Ceram. Eng. Sci. Proc.*, **5** [7-8] 625-42 (1984).
10. L.C. Sawyer, R.T. Chen, F. Haimbach IV, P.J. Harget, E.R. Prack, and M. Jaffe, "Thermal Stability Characterization of SiC Ceramic Fibers: II, Fractography and Structure," *Ceram. Eng. Sci. Proc.*, **7** [7-8] 914-30 (1986).
11. A.J. Eckel and R.C. Bradt, "Strength Distribution of Reinforcing Fibers in a Nicalon Fiber/Chemically Vapor Infiltrated Silicon Carbide Matrix Composite," *J. Am. Ceram. Soc.*, **72** [3] 455-58 (1989).
12. E. Lara-Curzio and C. Ross, "Why is it Necessary to Measure Each Fiber Diameter When Determining the Distribution of Strengths of Ceramic Fibers," *Ceram. Eng. Sci. Proc.*, (1999) in print.
13. H.M. Yun and J.A. DiCarlo, "Time/Temperature Dependent Tensile Strength of SiC and Al₂O₃-Based Fibers," Ceramic Transactions Vol 74, Advances in Ceramic-Matrix Composites III, eds. N.P. Bansal and J.P. Singh. pp. 17-26 (1996).
14. S.J. Zhou and W.A. Curtin, "Failure of Fiber Composites: A Lattice Green Function Model," *Acta Metall. Mater* **43** [8] 3093-3104 (1995).
15. Joseph Halada, Allied Signal Corporation, private communication.

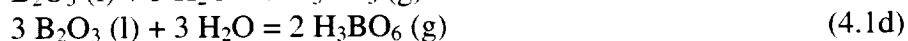
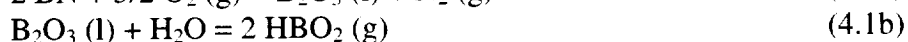
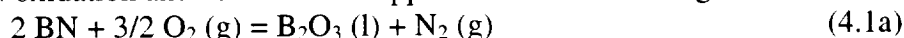
4.0 MODELING COMPOSITE RUPTURE

A model for rupture of MI-matrix and CVI-matrix composites has been developed based on the results of this study. Several factors need to be accounted for in order to model rupture of these composites: the oxidation of the BN interphase, the rate and extent of fiber weakening, and the damage state in the form of transverse matrix cracks.

4.1 Factors Controlling Rupture

4.1.1 Oxidation of the BN Interphase

Oxidation of BN can occur at temperatures as low as 450°C and is significantly enhanced when small concentrations (100 ppm) of water vapor in the environment caused by volatilization of the oxide reaction product [1,2]. Based on the thermodynamic data, the processes that control BN oxidation and volatilization appear to be the following:



At temperatures below ~ 900°C, volatilization is controlled by processes 4.1c and 4.1d. Above ~ 900°C, volatilization is controlled by 4.1b [1,2].

In addition, the boria reaction product can react and/or enhance the oxidation of the SiC fiber and matrix. This was demonstrated by Jacobson et al. [2] when a CVD SiC plate with a 2 µm coating of a low processing temperature BN* was oxidized at 900°C in an O₂ environment containing 20 ppm of H₂O. After 50 hours, the resulting oxidation product was approximately 8 µm on the surface of the SiC. Pure SiC under the same conditions would possess a SiO₂ scale less than 0.5 µm. Also, the oxide scale contained very little B. A similar sample was oxidized under the same conditions for two hours. The oxidation product for this condition was predominantly boria. Therefore, within a relatively short time at a very low H₂O concentration, BN on SiC oxidizes to form a very thick oxidation product in which B is leached out of the oxide product with time via the same reactions listed in 4.1b to 4.1d.

For the ambient air conditions of the experiments performed in this study, the water content in the atmosphere on a cold day in the winter would be ~ 0.003 atm**, about two orders of magnitude greater content of H₂O than Jacobson et al. [2] used. For experiments performed on very warm days, the water pressure can climb to as high as 0.025 atm**. Therefore, it can be expected that the presence of water vapor in the atmosphere will enhance oxidation and reduce the boron content of the glass at an even faster rate than was observed by Jacobson. The significance of this is that as B₂O₃ is removed from the oxidation product, the viscosity of the liquid would increase and possibly freeze if enough B₂O₃ is removed [6].

The accessibility of the environment depends on whether a concentration gradient exists due to the consumption of oxygen and water vapor and the formation of gaseous reaction products. It is apparent that for short times, there exists such a concentration gradient. For Regime I rupture, the area fraction of embrittled load-bearing tows increases with time from the outside of the composite inward (Section 3.1.3). Figure 4.1 plots the area fraction of embrittled tows versus

* The stability of BN in water containing environments depends on the purity and crystallinity of the BN [3,4]. Higher temperature processing results in denser and more crystalline BN [5]. The lower temperature CVD BN used by Jacobson is comparable to the BN used in SiC/SiC composites.

** Based on data received from the National Weather Service and the effectiveness of the air handling system in Building 106 of NASA Glenn Research Center (see reference 15).

time for the MI-matrix composites. Also plotted is a data point from 18.1 hour Regime II rupture surface. For this rupture surface, a condensed phase oxidation product covered the BN and matrix at least to a depth of three plies from the outer surface of the composite cross-section. It is signified with an arrow pointing in the higher fraction – shorter time direction because oxidation penetration was at-least this deep. For Regime II conditions, the BN interphases in a matrix crack were not directly exposed to the environment since a continuous layer of oxide covered the matrix and interphase. For Regime I conditions, most of the BN interphases in a matrix crack were still exposed to the environment during rupture (Figure 3.10b). For this reason, quantifying the kinetics of oxygen ingress is difficult because it is not based on the total BN surface area exposed or BN recession distance but just on the enhanced or faster oxidation of BN between fiber-to-fiber contact points. For this reason, the empirical relationship shown in Figure 4.1 will be used where the embrittled depth of a composite is proportional to time to the one-half power.

A fast rupture rate (Regime I) only exists for a few hours: ~ 2 hours for the Brewer et al. material and ~ 6 hours for the material tested in this study. It can be argued that a gas concentration gradient for slower rupture rate (Regime II) conditions does not exist through the matrix crack because all of the exposed crack surfaces and interphases in the matrix cracks are covered with a condensed phase oxide reaction product. In other words, the gas composition is very similar to the atmosphere. If the BN is covered with a boron or borosilicate layer, oxidation of BN will be controlled by the kinetics of diffusion through the passivating oxide layer and would significantly slow down BN oxidation. However, the physical phenomenon controlling rupture, fusing the fibers to one another, has already occurred by this time.

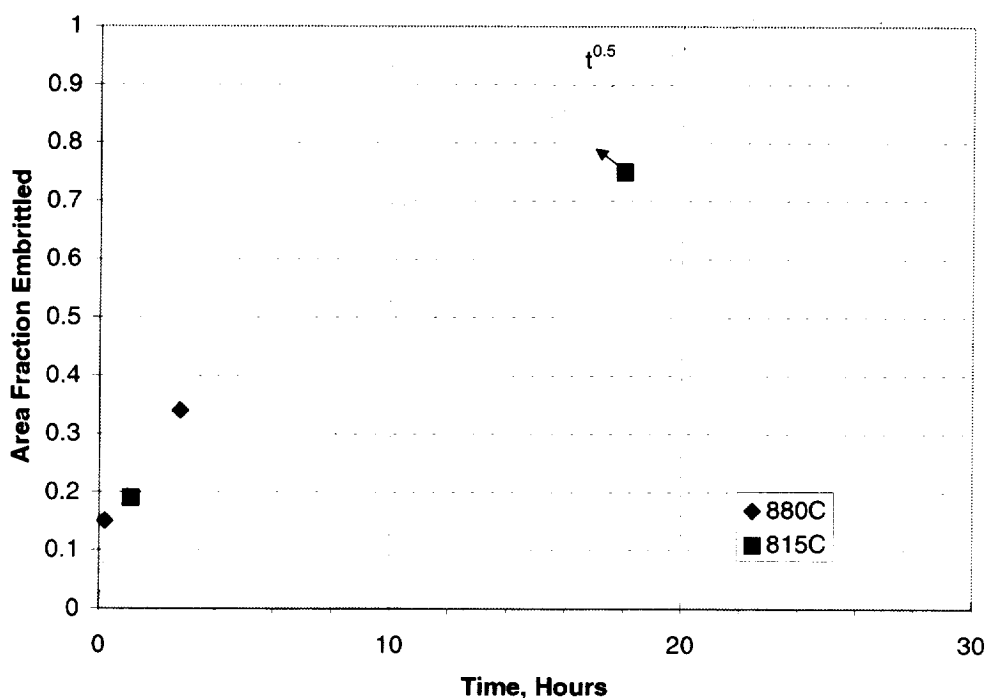


Figure 4.1: Area fraction of embrittled load-bearing tows versus time determined from the fracture surfaces of rupture specimens. The shortest time data points correspond to Regime I rupture and the longer time (with arrow) data point corresponds to a Regime II rupture condition where a condensed phase oxidation reaction product was apparent three plies from the surface of the composite cross-section.

It is possible that matrix crack sealing could occur from the production of an oxide reaction product that fills the crack and prohibits the ingress of the environment to load-bearing fibers. Observations consistent with this were made at a few locations on Regime II fracture surface; however, these few locations corresponded to a small fraction of the load-bearing fibers (Section 3.1.4). Therefore, it can be concluded that at this low a temperature, crack sealing is not occurring to slow down environmental ingress.

Finally, the creation of a strong-bond must occur in order for fiber fracture surfaces to be correlated to embrittled load-bearing tows at the composite fracture surface. This means that the oxidation of BN and removal of B_2O_3 form the borosilicate oxidation product must occur in a short time (0.2 hours for the shortest experiment). This is reasonable considering the thin section of BN that is oxidized and the much higher water content of the environment compared to the experiment performed by Jacobson et al. [2] as stated above. Also, Hi-Nicalon fibers oxidize at a faster rate than pure SiC [7] that would only increase the SiO_2 content of the oxidation product.

4.1.2 Fiber Weakening

Apparent fiber “weakening” during stress-rupture in other SiC fiber systems has been attributed to the removal of a carbon interphase, thereby increasing the gage length of fully-loaded fiber [8], and, alternatively, flaw growth in the form of an oxide scale [9,10]. For the composite in this study, interface volatilization in the loading direction was on the micron scale compared to the millimeter scale for carbon oxidation. Therefore, a gage length effect is minimal at best for these conditions. Oxide layers are formed on the fibers at fiber-to-fiber contact points for short times and around the circumference of the fiber for longer times. It is also true that where fibers fuse together is the failure location for most of the embrittled fibers. However, fibers that are not oxidized but are fully-loaded in the through thickness matrix cracks, weaken at a rate comparable to individual fibers subjected to similar stress-temperature-time conditions (Figure 3:14a). It is reasonable therefore to assume that the fibers in the embrittled regions of matrix cracks also weaken according to the same mechanism. However, the effective fiber gage length reduces as fibers are bonded to one another since it is observed that no or little pullout occurs for embrittled fibers. In addition, since a strong bond exists, a change in applied load will result in a stress-concentration at a strongly bonded fiber [11]. This could also result in local-load sharing conditions [12,13] where the load shed from an individual fiber that breaks would be carried by the nearest neighboring fibers instead of distributed amongst all the load-bearing fibers bridging a matrix crack. It is also apparent that for these strongly bonded fibers, once one fiber breaks all the fibers that are interconnected will subsequently fail.

Unfortunately, the stress-rupture data of Yun and DiCarlo [14] only describes the average stress for fiber failure at a certain stress and temperature and does not reveal the strength of a fiber which is subjected to a condition not as severe as the rupture-criterion. In fact the rupture data from the Larson-Miller data for individual fiber rupture would correspond to a time exponent, n , of ~ 50 ($\sigma = t^{-n}$). For minicomposites tested under similar conditions [15] the time exponent, n , was ~ 40 . This infers that most of the crack growth leading to failure occurs just prior to the failure event and not at a constant rate during the applied loading.

4.1.3 Matrix Cracking

As discussed in section 3.1.2, matrix cracking continues to occur even after the saturation load for a given rupture experiment has been attained. The mechanism and kinetics for matrix crack growth cannot be quantified from the results of this study, especially for the lower stress conditions. However, matrix crack growth without fiber failure in the crack wake could be due to lowering of the toughness of the matrix. A slight reduction in elastic modulus with temperature and/or slow crack growth of the matrix also could account for this. It is also possible that the interfacial shear stress at the fiber-matrix interphase could be lessened during the initial stages of oxidation that would result in raising the stress intensity at the crack tip. For simplicity, this modeling effort will only incorporate the final crack density for each specimen into the rupture model in order to estimate the length of fully-loaded fibers.

4.2 Fiber Failure Considerations

It is evident that fibers in the embrittled region of a matrix crack fail first. It is also apparent or at least suggestive that all the fibers or groups of fibers in an embrittled region fail at the same time due to the strong bonding which exists between fibers. Therefore, the critical factor to determine is the stress-state on the embrittled fibers and whether that is sufficient to fail fiber(s) that can “trigger” embrittled fiber failure. After embrittled fibers fail, the composite failure will depend on the ability of the remaining unembrittled fibers to carry the extra load.

In order to determine the likelihood for weak fibers existing, Weibull probability distributions can be employed for the various composite crack density and loading conditions encountered in this study. The Weibull probability relationship is as follows:

$$P(\sigma, L) = 1 - e^{-\Phi(\sigma, L)} \quad 4.1$$

where L corresponds to the effective gage length and Φ the fraction of failed fibers for the applied stress condition given by:

$$\Phi = (L/L_0) (\sigma/\sigma_0)^m \quad 4.2$$

where m is the Weibull modulus and the stress scale parameter, σ_0 , is the stress required to cause one failure, on average, in a specimen of L_0 . The reference stress, σ_0 , and length scale, L_0 , parameters correspond to the average strength for individual fibers tested in tension with a 25.4 mm gage length. For room temperature, σ_0 is 2800 MPa. For elevated temperature conditions and through thickness cracking, σ_0 will be estimated based on the time dependent strength, $\sigma_{o(t,T)}$ determined by Yun and DiCarlo [14] for the time-temperature conditions of this study:

$$\sigma_{o(t,T)} = \sigma_{f-ult}(t,T) = 10^{[-1.625E-5 T \log(t) + 3.635]} \quad 4.3$$

The only quantity that needs to be estimated is L .

L corresponds to the length of fiber that is fully loaded in the 15 mm length of a specimen in the hot zone. For unembrittled fibers (global load sharing), L will be approximated as the length that the fibers are fully loaded in the matrix crack plus the length that the fibers are nearly fully loaded in the half-debonded region away from the matrix crack for all of the matrix cracks in the 15 mm gage length. The crack opening, u , at each matrix crack can be estimated by the relationship [16]:

$$u = (b_2 + b_3) [fE_c / (1-f)E_m]^2 \{ (\Gamma_i / RE_m)^{1/2} (\sigma_p - \sigma_i) / c_1 \tau + (\sigma_p - \sigma_i)^2 / 2E_m \tau \} \quad 4.4$$

where R is the fiber radius, Γ_i is the interface fracture energy (assumed to be 10 J/m^2 [17]), and

$$\sigma_i = (E_m/c_1) \{ (\Gamma_i/RE_m)^{1/2} - c_2\varepsilon_T \} \quad 4.5$$

The constants, b_2 , b_3 , c_1 , and c_2 , are relationships between the composite constituent elastic constants [16] and ε_T is the misfit strain from the difference in thermal expansion coefficients between the fiber and matrix. The sliding length at a single crack, l , can be approximated by the relationship:

$$l = \sigma_i R / 2\tau \quad 4.6$$

Table 4.1 lists the values used in equations 4.4–4.6.

Several conditions will be considered:

- (1) composites tested at room temperature ($\sigma_o = 2800 \text{ MPa}$)
- (2) composites tested at 815°C for the same time/temperature/stress conditions of the samples failed in this study incorporating the degradation in “intrinsic” fiber strength properties, $\sigma_{o(t,T)}$, based on the data of Yun and DiCarlo [14]
- (3) composites tested at 815°C for the same time/temperature/stress conditions of the samples failed in this study assuming the as-produced fiber reference stress ($\sigma_o = 2800 \text{ MPa}$) and L equal to the cumulative crack opening displacements from the crack density measurements after the rupture test and no sliding
- (4) same as (3) with $\sigma_{o(t,T)}$ as the characteristic stress

Table 4.1: Values used in model.

$f = 0.17$
$E_f = 270 \text{ GPa}$
$E_m = 187 \text{ GPa}$
$E_c = 215 \text{ GPa}$
$\nu = 0.15$
$b_2 = 0.679$
$b_3 = 19.4$
$c_1^2 = 4.24$
$c_2^2 = 0.301$
$\tau = 36 \text{ MPa}$
$R = 6.5 \text{ }\mu\text{m}$
$\varepsilon_T = 0.1\%$
$\Gamma_i = 10 \text{ J/m}^2$
$m = 4$

Conditions (3) and (4) are based on the fact that little or no pullout is observed for embrittled fibers and therefore there is no sliding length contribution to the total gage length of fully-loaded fibers. The two highest stress-rupture conditions did have some pull-out in the embrittled fiber regime (e.g. Figure 3.10). Based on the fracture surface observations, it was assumed that the embrittled fibers of the 227 MPa and 185 MPa rupture specimens had sliding lengths of 3 and 1 fiber diameters, respectively. These sliding lengths were added to the crack opening lengths for the determination of L in conditions (3) and (4) (Figure 4.2).

Figure 4.2 shows the results of the probability to failure for the four conditions. Also plotted in Figure 4.2 is the time to failure for the given applied stress. As expected, lower applied stresses result in lower probabilities that a fiber will fail. The effect of modifying σ_o from the as-produced strength to $\sigma_{o(t,T)}$ corresponds to approximately an order of magnitude increase in the probability to failure in the stress-range of interest.

One apparent anomaly in Figure 4.2 is the increase in the probability to failure for the lowest stress rupture specimen. This was the specimen that was precracked at 227 MPa and then tested in rupture at 111 MPa. The crack density was very high for the precrack stress and resulted in relatively larger contribution to L compared to the higher applied rupture stress specimens that were not precracked even though the applied stress was low.

The probability for failure of (1) and (2) are similar to, at higher stresses, or greater than, at lower stresses, (3) and (4). (1) and (2) would correspond to conditions of no embrittlement at room and elevated temperatures, respectively. Even though they have higher probabilities for failed fibers, these conditions would also correspond to global load sharing conditions. When a fiber breaks the load is shed globally in the bridged crack so that the load shed on the other load-bearing fibers is a very small amount. For example, if one fiber breaks, the load that fiber was carrying would be distributed among the other 33,750 fibers (for the specimen dimensions and fiber lay-up of this study) in a through-thickness matrix crack. For a more extreme case, if 10% of the fibers failed at a given applied stress the stress on the remaining fibers in the matrix crack would only be increased 11%, not a catastrophic amount.

The most appropriate estimate for the probability to failure would be condition (4). Based on this analysis, it is not even likely that a fiber would fail in the gage section for the three lowest stress condition of this study, (140, 129, and 111 MPa). For the 148 MPa stress condition, 1.5 fibers are expected to fail and for the 163 MPa stress condition, 3.5 fibers are expected to fail.

From this analysis, it is apparent that for the lower stresses, very few fibers, if any, are likely to break. Therefore, additional stress must be applied to embrittled fibers in the form of local stress concentrators in order for some fibers to fail and trigger larger regions of embrittled fibers to fail.

Probably the most likely source for stress-concentrators would be in the form of the intrinsic stress-concentration on the outer rim of fibers at unbridged-bridged crack transition [18] (Figure 4.3). Large portions of a matrix crack are unbridged due to crack propagating through 90° plies and large matrix regions of the woven architecture. The outer "rim" of fibers in a load-bearing bundle would experience a stress-concentration due to the greater crack opening of the unbridged portion of matrix crack compared to the bridged portion of matrix crack (Figure 4.3). This is similar to the approach taken by Evans et al. [19] for a unidirectional material where the stress concentration on the outer row of fibers at the end of an unbridged crack led to fiber failure and crack growth.

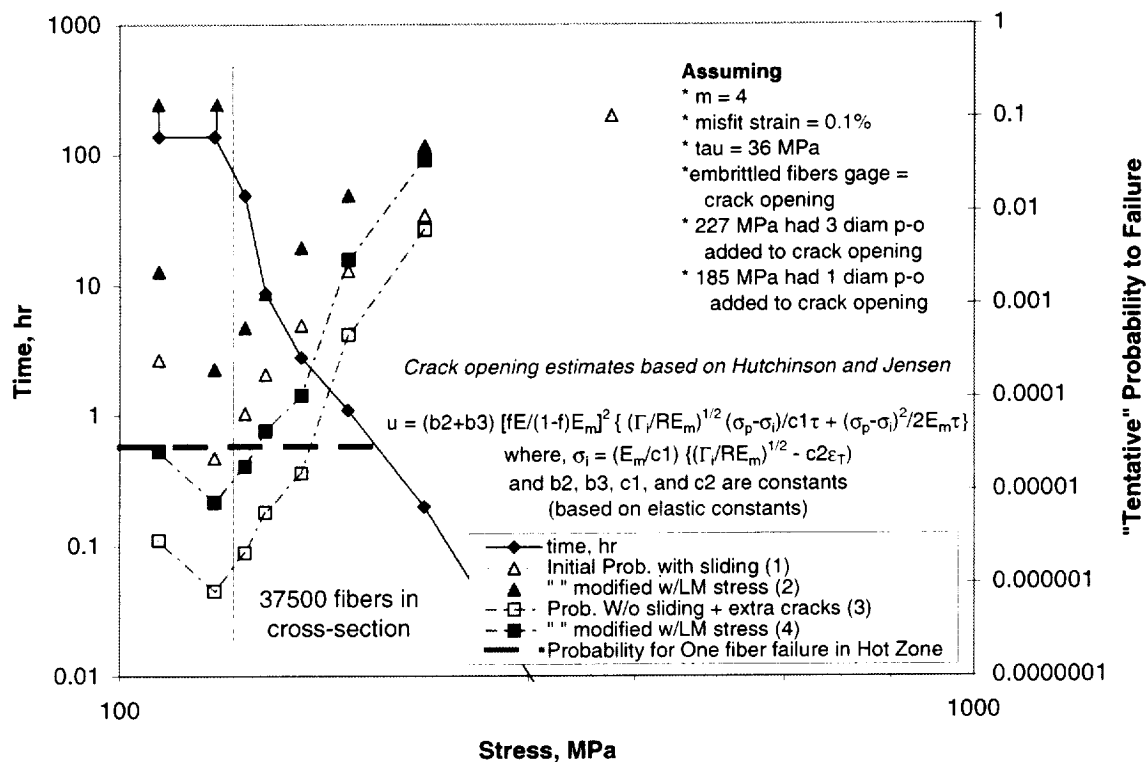


Figure 4.2: Probability to failure for as-produced and rupture conditions. The horizontal dashed line indicates the probability for one fiber to break in the hot zone section of the specimen. The vertical line indicates the demarcation above which rupture specimens failed during the test.

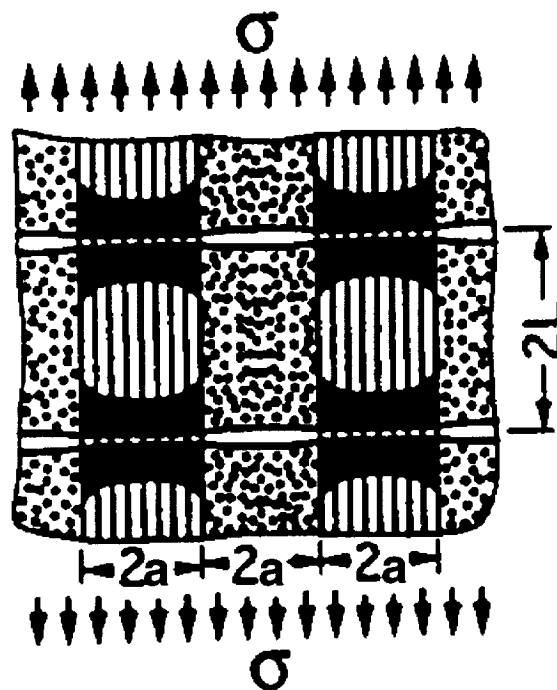


Figure 4.3: Schematic representation of stress-concentration at load-bearing fibers in a 2-ply composite (from Xia et al. [18]).

This stress concentration can be modeled as a “line-spring” condition where the fibers are treated as elastic springs. A modification to this analysis was made by Xia et al. [17] to incorporate the relief of some of the stress-concentration due to large slip lengths. The stress-concentration will be further relieved with increasing numbers of cracks since fibers would slide over longer lengths. In fact, when the matrix crack saturation limit is reached, the stress concentration is nil. However, for the low stress conditions of this study, matrix crack saturation was never reached. Xia et al [18] have modeled this stress-concentration effect and have found it to depend on the parameter η :

$$\eta = \{3\pi f^2 E_f E / (1-f)^2 E_m^2 A\} [a\tau / R_f \sigma] \quad 4.7$$

where A is an orthotropy factor (ranges between 0.8 and 1 for most composites [18], assumed to be 1 in this analysis) and a is half the unbridged crack size, in this case half the ply width (Figure 4.3).

The stress concentration as a factor of η was found numerically. However, it was shown that the stress concentration factor, S_c , could be approximated by:

$$S_c = (1 + \eta^{2/3})^{1/2} \quad 4.8$$

Table 4.2 lists the stress condition and stress-concentration factors used in this study.

Table 4.2: Stress concentration factors determined from η .

Stress, MPa	η	S_c
227*	13.0	1
185*	16.3	1
163	18.0	1.40
148	19.9	1.44
140	21.0	1.47
129	22.8	1.50
111*	26.5	1

*Crack density reached or exceeded matrix crack saturation density at higher temperature regions of sample during the rupture experiment.

4.3 Modeling Rupture Behavior with Through Thickness Cracks

Fiber weakening due to slow crack growth, the damage state, the rate of oxygen ingress into the crack, and the stress-concentration at the outer rim of fibers due to the unbridged-bridged crack transition were all incorporated into a simple model for MI composite rupture. This model will then be extended to CVI macrocomposite and CVI minicomposite rupture. One simplification is that only through-thickness cracks are considered. An attempt was made to assume microcracks that could grow but no additional insight was gained since a crack-growth criterion is not available for this material.

4.3.1 MI Matrix Composite Rupture

The fraction of fibers which fail, ϕ , for the applied load at $t = 0$ is determined from eqn. 4.2 for L_0 and σ_0 of as-produced fibers (25.4 mm and 2800 MPa, respectively). The strength on the remaining fibers, on average, would be

$$T = \sigma / (1 - \phi) \quad 4.9$$

With time, the fibers weaken according to the data from Yun and DiCarlo [14] (Eqn. 4.3). Therefore the fraction of fibers that fail would increase with time and temperature according to:

$$T_{t,T} = \sigma / (1 - \phi_{t,T}) \quad 4.10$$

where the reference length for $\phi_{t,T}$ is still 25.4 mm and $\sigma_{0(t,T)}$ was from Eqn. 4.3. Fibers will continue to fail until the composite fails. The simplest condition for failure will be when the stress on the remaining fibers reaches the ultimate stress condition which can be approximated by fiber bundle theory [10]:

$$T_{\max} = \sigma_{0(t,T)} (emL/L_0)^{-1/m} \quad 4.11$$

where T_{\max} is the average fiber stress criterion for failure. As expected (e.g. Figure 4.2), simply based on the slow-crack growth weakening of fibers, too few fibers would fail to cause ultimate failure of the composite alone for the applied stresses of this study.

The fraction of embrittled fibers can be estimated by best fitting the measured environmental ingress data of Figure 4.1:

$$f_{\text{emb}} = 0.215 t^{1/2} \quad 4.12$$

As mentioned earlier, it was observed that some pullout of fibers occurred for the embrittled fibers at the two highest stress-rupture conditions. For the applied stress conditions below 185 MPa, no pullout is observed for embrittled fibers. Because of these observations, L in $\phi_{t,T}$ will be treated the same as for the earlier statistical analysis (Figure 4.2), i.e. the case "without sliding" (Section 4.2). This would even make it more unlikely that fiber failure would occur in the embrittled region of a matrix crack without a stress-concentration.

Since, it is observed that the embrittled portions of the matrix crack fail "together" due to the network of fused fibers in a tow, it is likely that once one fiber fails in a bundle, all of the fibers in that bundle will also fail. This "cascade" of fiber failure would progress to any other neighboring embrittled bundles. The effect on the neighboring bundle is discussed in Section 4.4; however, at this point it will be assumed that when one embrittled fiber breaks, all the embrittled fibers in the matrix crack fail.

The parameter η (Eqn. 4.7) was determined for each applied stress condition (Table 4.2). The number of fibers making up the circumference of a bundle was counted and found to be ~ 124 . The number of embrittled bundles in a crack was estimated based on f_{emb} and the total number of bundles in the specimen cross-section (67.5). S_c can be determined from Eqn. 4.8 and the stress on the outer rim of embrittled fibers can be determined from:

$$T_{\text{outer}} = T S_c \quad 4.13$$

The fraction of outer-embrittled fibers to fail can then be determined from:

$$\phi_{\text{outer}} = L_{\text{emb}}/L_0 (T_{\text{outer}}/\sigma_{0(t,T)})^m \quad 4.14$$

The likelihood of a fiber failing in a matrix crack can then be determined from the number of available outer-embrittled fibers.

For higher stress conditions, Xia et al [18] showed that the critical density of matrix cracks for elimination of the stress-concentration occurs when:

$$(a/L_{\text{crack}})_{\text{crit}} = [f E t \tau] / [(1-f)E_m R_f \sigma] = (2 a \rho_{\text{crack}})_{\text{crit}} \quad 4.15$$

where L_{crack} is half the crack spacing (Figure 4.3) and ρ_{crack} is the measured crack density in the hot zone. Figure 4.4 shows $(a/L_{\text{crack}})_{\text{crit}}$ and the measured a/L_{crack} for the MI Composite stress-rupture conditions. The measured value for the normalized density of matrix cracks is always lower than the normalized critical density of matrix cracks. The cause of the difference in a/L_{crack} values at 227 MPa is not known. Perhaps it is due to not incorporating the elastic properties of the interphase (which were essentially rolled into the matrix modulus). At any rate, it is evident that matrix crack saturation had occurred where ρ_{crack} reached 2.4mm^{-1} for the 227, 185, and 111 MPa. Therefore, no stress-concentration was used for the outer fibers for these stress conditions. A $S_c > 1$ used for these stresses would have no effect on the model predictions.

It is also possible that embrittled fibers can fail at the interior of an embrittled tow due to the applied stress. The same approach was taken for the “inner” fibers of an embrittled bundle (376 inner fibers per bundle) as for the outer fibers except no stress-concentration was applied. The fraction of inner-embrittled fibers to fail can then be determined from:

$$\Phi_{\text{inner}} = L_{\text{emb}}/L_o (T/\sigma_{o(t,T)})^m \quad 4.16$$

where T is the average fiber stress (Equation 4.9).

Equations 4.7 to 4.14 and 4.16 were determined for time iterations of 0.1 hours up to one of the following two failure criteria:

I(a): *Picture Frame*. The composite fails when T_{max} is achieved for the unembrittled fibers in the cross-section of a through thickness crack. This requires successive embrittled fiber failure to occur while the oxidation front progresses into the matrix crack the necessary distance and for all the embrittled fibers in a matrix crack to fail when one fiber fails in the matrix crack.

I(b): *Fully Oxidized Matrix Crack*. The composite fails when the first embrittled fiber fails after the crack is fully oxidized, i.e. all the fibers are embrittled.

The results of the model for three different values of Weibull modulus are shown in Figure 4.5. There is very good agreement with the model and the actual experimental data. The Weibull modulus had a minimal effect for the model predictions except for the “run-out” stress condition. The predicted run-out stress condition was highest for higher values of m .

Figure 4.6 shows the predicted number of fiber failures for three of the stress-rupture conditions. For the 163 MPa condition, the fiber failures occurring in the unoxidized and oxidized (embrittled) portion of the crack were predicted. The data was further separated to show the number of fiber failures predicted to occur in the outer-rim of the bundles and the interior of the bundles for both situations. More fibers are expected to fail in the unoxidized portion of the crack based on this model since the effective gage length of the loaded fibers is greater (crack-opening plus sliding length contribution). The gage length estimated for the

embrittled portion was only the crack-opening^{*}. In addition, for the shorter times most of the area of the crack has not been oxidized. The reason for the decelerating rate of fiber failure in the 163 MPa unoxidized portion of the crack is due to the decreasing amount of unoxidized crack area with time. It is for this reason that the predicted number of failed fibers in the unoxidized portion of the crack is not shown for the lower stresses. The rate of fiber failure in this region decelerates to zero within six hours. For the 148 MPa condition, after six hours, approximately 35 fibers had failed in both the outer rim and interior regions of the unoxidized bundles.

Figure 4.6 also shows the effect of stress-concentration on fiber failure. If there was no stress-concentration on the outer rim of fibers, there should be only one third of the number of interior failed fibers in the outer rim of the bundles. A greater number than that occurs for the 163 MPa condition. With decreasing applied stress, a greater proportion of outer-rim fibers fail so that the number of outer-rim failures equal the number of interior fiber failures for the 148 MPa condition and are slightly greater for the 140 MPa condition. As can be seen with the lowering of stress, fewer fibers will fail. At too low of a stress, e.g. 129 MPa, no fibers will fail in a reasonable time.

Based on equation 4.12, the time for all of the fibers to be embrittled would be approximately 21.6 hours. For rupture times less than this time case I(a) applies whereas for rupture times greater than this time case I(b) applies. Both failure cases are possible in SiC/SiC; however, for the MI-SiC, I(a) applied for most conditions. This can be seen in Figure 4.6 as a change in the fiber failure rate. For all of the conditions predicted to fail at times less than 21.6 hours, the fiber failure rate increases proportional to the square root of time, i.e. the rate of composite cross-section embrittlement (Figure 4.1). A significant reduction in the rate of fiber failure would occur for times greater than it takes to embrittle the entire matrix crack. This would occur since no new embrittled fibers would be added and embrittled fiber failure would only be dependent on the weakening of fibers due to the slow crack growth mechanism [14]. This is shown more clearly with the modeling of CVI SiC composites where I(b) is more common (see Figure 4.8).

^{*} This may or may not be a faulty assumption. When the fibers fuse together, they do so at the fiber stress condition along the length of the fiber the same as (or nearly so) that expected in the unoxidized crack due to the load-sharing condition governed by τ . It would be expected that the embrittled fibers would fail at the same effective gage-lengths. However, the crack-opening gage length is used because there is no observation of pulled-out fibers in the embrittled regions. This issue will be discussed in section 5.2.2.

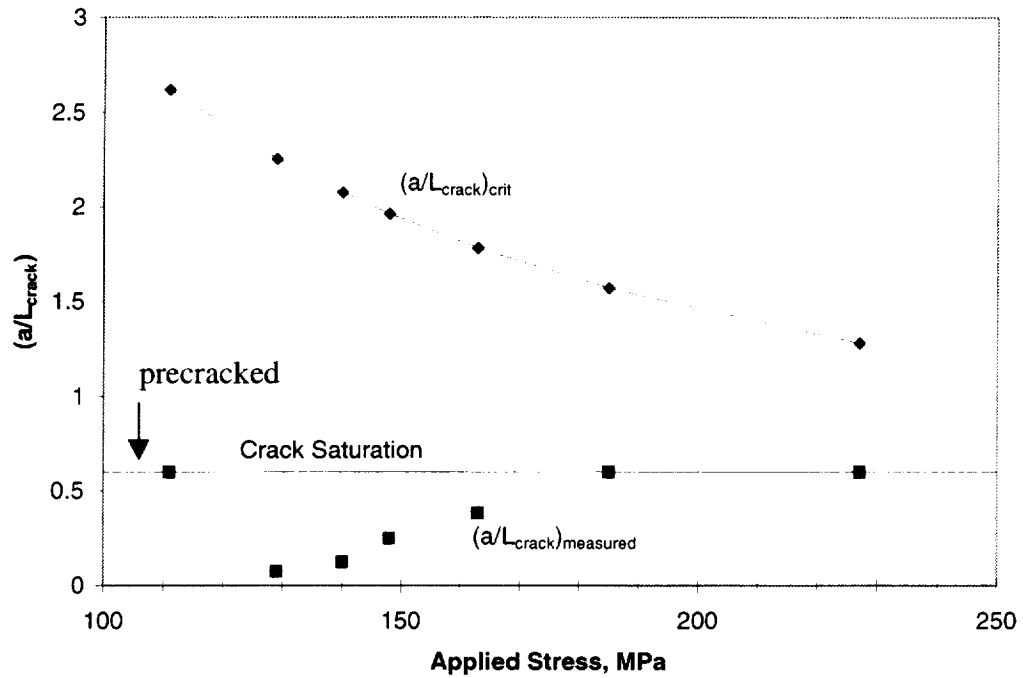


Figure 4.4: Critical crack density for elimination of stress-concentration for MI matrix composite rupture based on Xia et al. [18].

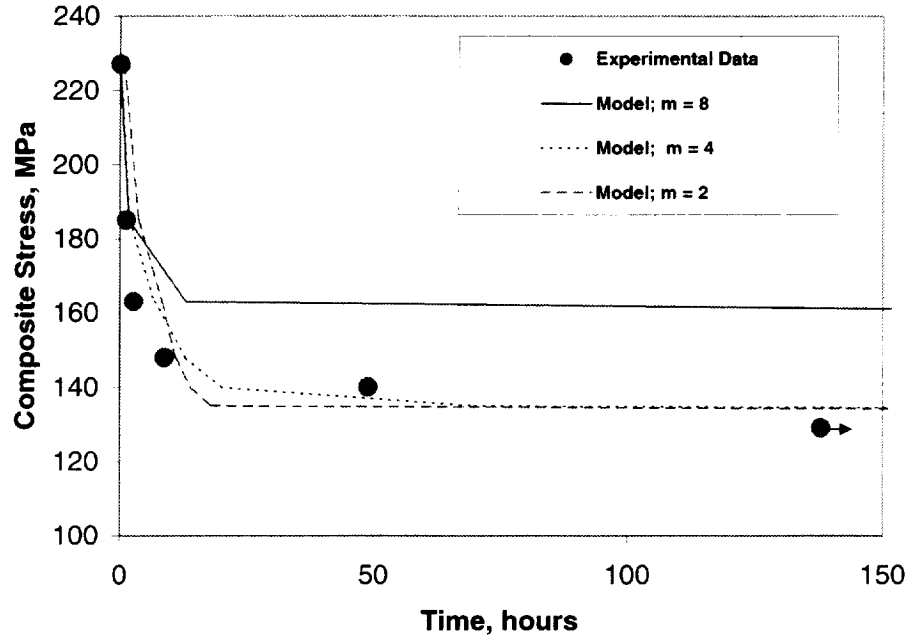


Figure 4.5: MI composite rupture modeled for through-thickness matrix cracking.

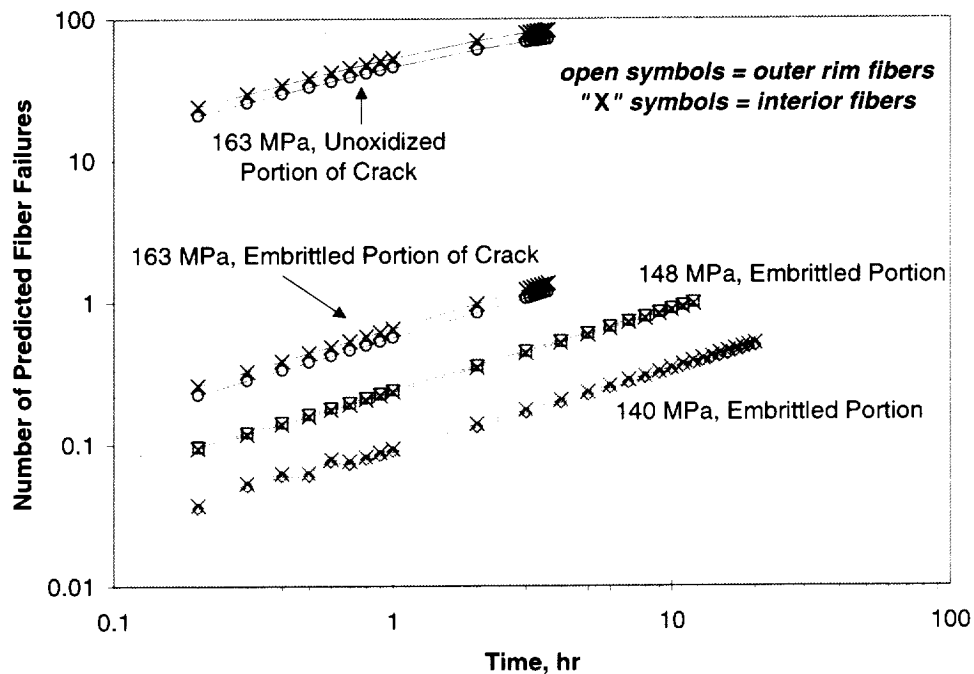


Figure 4.6: Predicted number of fiber failures at the outer-rim of the embrittled fiber-bundles and in the interior of the embrittled fiber-bundles throughout the gage section of the composite for $m = 4$.

4.3.2 CVI Matrix Composite Rupture

The same approach was applied to CVI SiC composites. The crack density was estimated from the final crack spacing of a specimen failed at room temperature and the known AE activity of that specimen as a function of stress (Appendix A and ref. 20). η and S_c were determined as before for each stress condition. Table 4.3 lists the estimated crack density, η , and S_c for the CVI matrix composite rupture conditions modeled.

Figure 4.7 plots the normalized crack densities and is similar to the MI composite result where the critical value is greater than the estimated value. Again, for the highest applied stress where matrix crack saturation is nearly achieved, no stress-concentration was applied to the outer-rim of fibers in an embrittled bundle.

The CVI SiC matrix is very porous with a network of large pores throughout the entire specimen enabling oxygen access to every single load bearing tow. It was observed that embrittlement of all of the fibers took less than two hours. Therefore, the fraction of embrittled fibers will be much faster with time for these composites and rupture case I(b) will occur at times greater than or equal to 2 hours.

The model predictions are shown in Figure 4.8 for the three different values of m . Weibull modulus has a stronger effect on the predicted run-out stress condition for this system compared to the MI system. However, the model prediction for $m = 4$ is in good agreement with the measured rupture data. Figure 4.9 shows the number of fiber failures predicted for the outer-rim of embrittled tows and the inner fibers in the embrittled tows for $m = 4$. For all of these cases it was the first fiber failure that failed the composite and it was an outer-rim fiber which was predicted to fail. The inflection in fiber rupture rate (Figure 4.8) occurs for this system at two hours where the environment has fully accessed the entire composite cross-section.

Table 4.3: Estimated parameters for modeling CVI SiC matrix rupture.

Stress, MPa	Crack Density (mm ⁻¹)	η	S_c
186	2.8	12.0	1.25
139	2.3	16.1	1.36
130	2.1	17.2	1.38
114	1.7	19.6	1.44
111	1.5	20.2	1.45

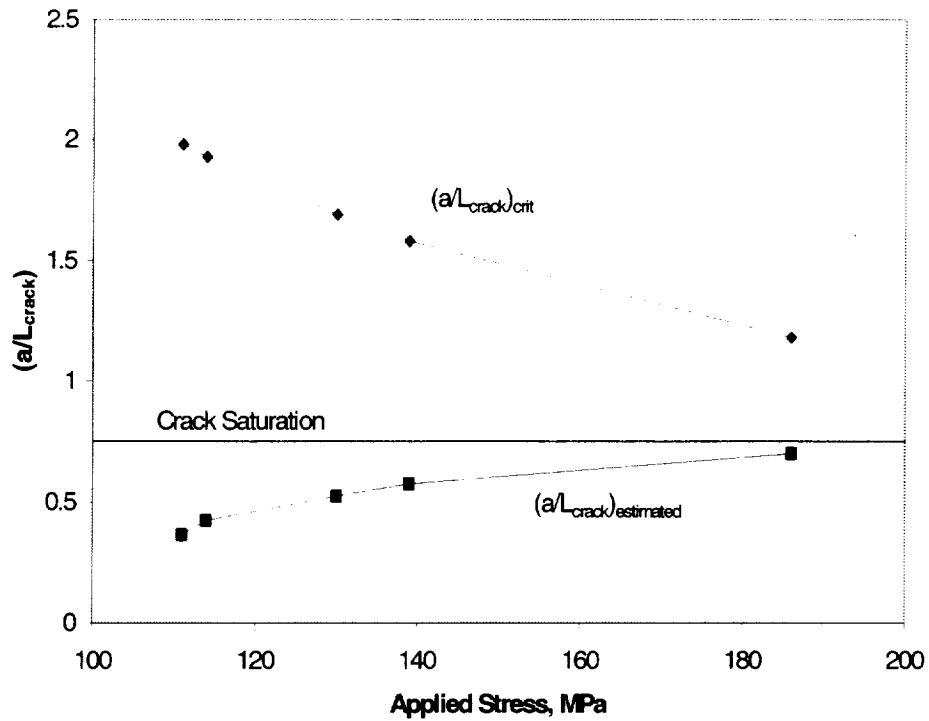


Figure 4.7: Critical crack density for elimination of stress-concentration for MI matrix composite rupture based on Xia et al. [18].

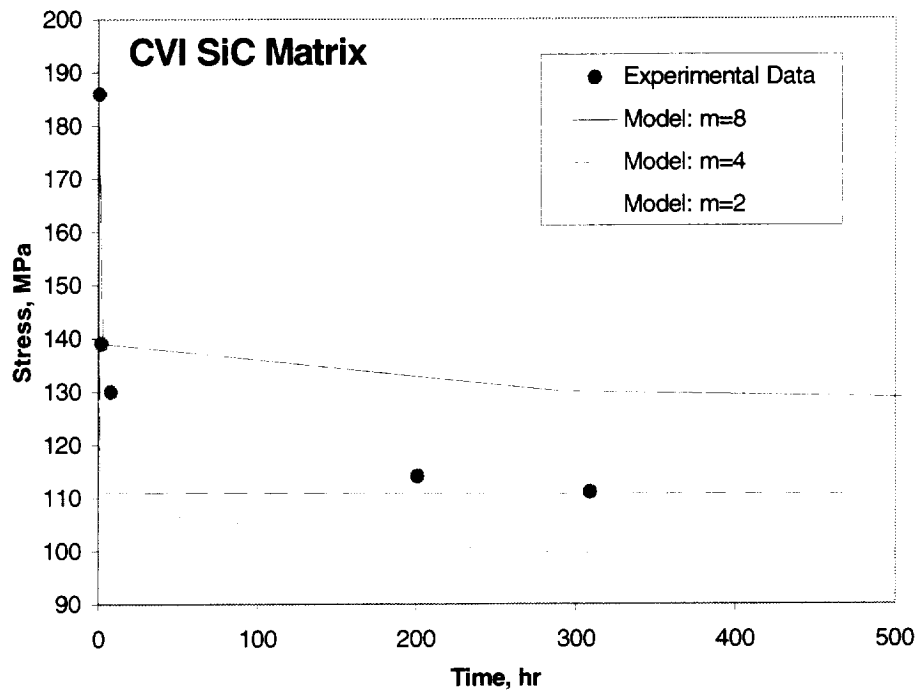


Figure 4.8: CVI composite rupture modeled for through-thickness matrix cracking with various values for m .

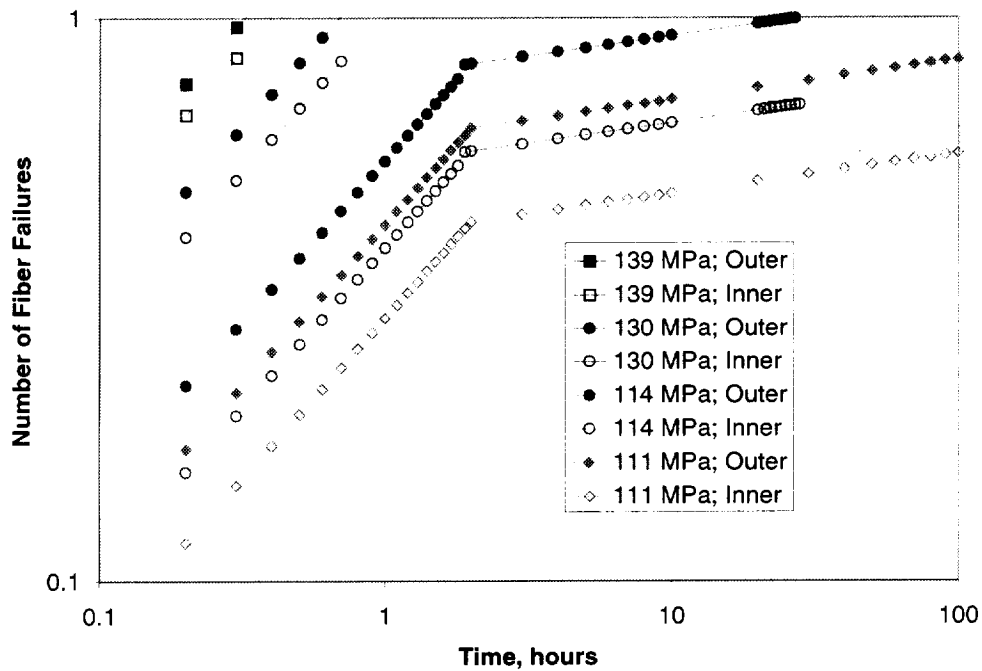


Figure 4.9: Predicted number of fiber failures at the outer-rim of the embrittled fiber-bundles and in the interior of the embrittled fiber-bundles throughout the gage section of the CVI composite for $m = 4$.

4.3.3 CVI Matrix Minicomposite Rupture

As discussed in the introduction, single tow, CVI matrix minicomposites have better rupture properties than SiC matrix macrocomposites. One of the reasons for this probably has to do with the absence of stress-concentrators from large unbridged matrix cracks since minicomposites are unidirectional and with a more uniform distribution of fibers throughout the thickness of the minicomposite. Also, minicomposite tests had been performed on precracked specimens, although the precrack density was about half the saturation crack density.

One other attribute of the minicomposites tested in an earlier study [15] was that the interphase coating was always greater than 0.3 microns around the circumference of the fiber. In other words, there were no near fiber-to-fiber contacts. In order for fiber-to-matrix fusing to occur, a significant amount of glass had to be formed to fuse the fiber to the matrix. At 815°C, the formation of a condensed phase oxidation product was not fast enough to result in minicomposite embrittlement. Higher temperatures were required to form enough oxidation product to strongly bond most of the fibers to the matrix. Figure 1.7 showed such fiber-to-fiber and fiber-to-matrix fusing for 950°C material ruptured after a few hours. It takes almost 100 hours at this temperature to completely fill in the interphase region. For minicomposites it is necessary to nearly fill in the interphase in order for significant embrittlement to occur because the recession distance of the BN itself is only on the order of tens of microns. The small recession distance enables fibers to remain suspended in the “hole” created by interphase recession and are unable to “move closer” to the matrix.

The embrittlement of these composites occurs between 900 and 1050°C for the HN/BN/CVI SiC minicomposite system and 950°C data will be modeled using the same approach as already used for the macrocomposite systems. The experimental data and estimated crack opening for the minicomposites are listed in Table 4.4. Figure 4.10 shows the model prediction for the three different Weibull moduli. It was assumed that global load-sharing existed for two hours after which fibers bonded to the matrix throughout the minicomposite thickness. Therefore, prior to one hour, Equation 4.11 must be satisfied for failure. After one hour, the first fiber break was assumed to cause composite failure.

Table 4.4: Experimental Data and Parameters Used to Model Minicomposite Embrittlement*

Failure Time, hr	Stress on Fibers, MPa	Crack Opening, μm
226	950	3.0
98	983	3.1
17	1114	3.8
3.3	1179	4.1
2	1179	4.1
1.9	1310	4.9

* $f = 0.16$; $E_m = 400 \text{ GPa}$; $\tau = 0.15 \text{ MPa}$; $\rho_{\text{crack}} = 1 \text{ mm}^{-1}$

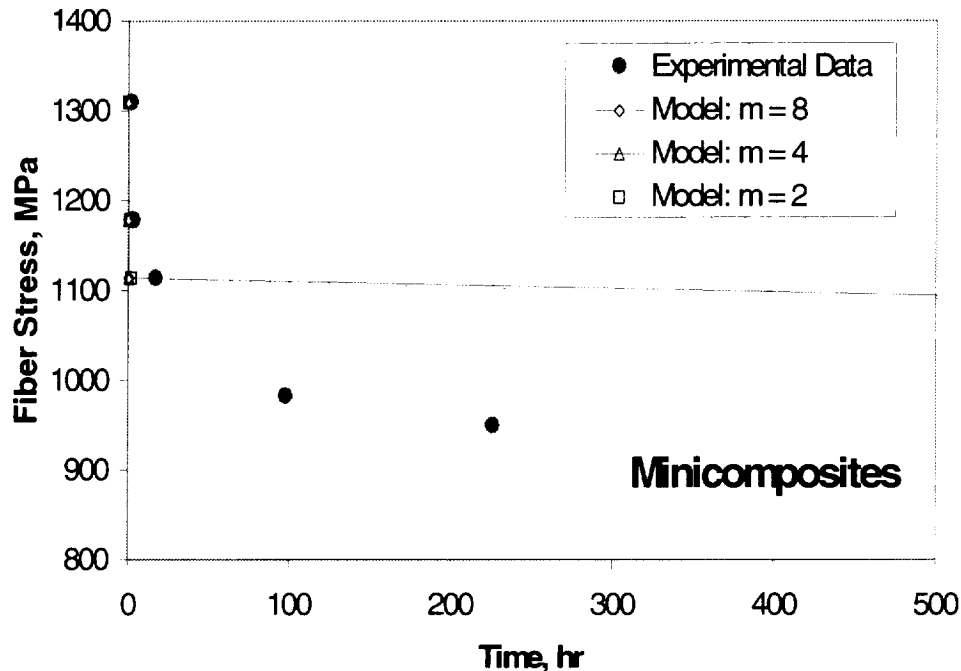


Figure 4.10: CVI SiC minicomposite rupture (950°C) modeled for through-thickness matrix cracking with various values for m .

The model predictions are remotely accurate except for the highest stress. There are probably several factors not taken into account in the model to account for this. First, the BN interphase is receding at a faster rate at 950°C than 815°C and therefore the length of fibers fully loaded are also increasing. Second, the fibers may be further weakened from the growth of relatively thick oxide scales at this temperature. In addition, it was observed on most fracture surfaces that a few fibers, with thick interphases, would have pulled out several fiber diameters whereas most of the other fibers had no pullout. These fibers may have failed first since the BN would have receded a greater distance and increased the gage length for those difficult to bond fibers. This could have been the trigger to cause minicomposite ultimate failure.

4.4 Modelling With Progressive Non-Bridging Crack Propagation

It was assumed in the above model that when one fiber breaks all the neighboring fibers break. This seems reasonable since nearly all the fibers in a bundle are connected to one another. It was also assumed that when one embrittled fiber bundle fails, all the embrittled fiber bundles fail. The likelihood of neighboring embrittled fiber bundle failure will be explored here.

The likelihood that a second fiber will fail at a neighboring embrittled bundle will be modeled in a matrix crack. When one fiber is predicted to fail from the initial conditions (section 4.3), the local load-sharing condition, local stress-concentration, and local likelihood that a fiber will fail in that specific matrix crack will be estimated.

Figure 4.11 shows a rendition of the cross-section of a woven, five harness satin composite. Depicted in the figure is an embrittled bundle that failed and shed its load on the neighboring bundles. Since the fibers are bonded together at this point, it is assumed that only

local load sharing occurs. It will be assumed that the load of the failed bundle will be shed to the four neighboring bundles. In addition, the size of the unbridged crack, a , in Equation 4.7 has at least doubled and S_c has increased accordingly (Equation 4.8) on the outer row of embrittled fibers. Therefore, for the new stress on the fibers in the neighboring four bundles can be estimated by:

$$T_{nn} = (T + T/4) S_c \quad (4.17)$$

where S_c for the outer row of fibers is estimated from Equations 4.7 and 4.8 and for the fibers on the interior of the neighboring bundles is unity. ϕ_{nn} can be estimated using the crack opening, L_{co} , as the tested length and the number of matrix cracks where a bundle has failed based on the number of fiber failures, N_{ff} :

$$\phi_{nn} = (L_{co}/L_o) (T_{nn}/\sigma_{o(t,T)}) * N_{ff} \quad (4.18)$$

It is important to again note that the length scale in Equation 4.18 pertains to the length of fibers in a crack(s) where a fiber break(s) has occurred. The length scales for ϕ in Equations 4.2, 4.10, 4.14, and 4.16 are the cumulative lengths of loaded fibers in all the cracks in the gage section. Therefore, L_{co} in Equation 4.18 will be on the order of a micron and the number of available fibers will be approximately 2000.

It was found that this type of analysis is most appropriate for the lower stress, fewer fiber failure conditions. For stresses applied at stresses equal to and greater than 163 MPa for MI composites and 185 MPa for CVI composites so many fibers fail and so little of the cross-section is embrittled that this analysis was not deemed useful.

Figure 4.12 and 4.13 show the results for the lower stress-conditions that lead to failure for MI and CVI composites, respectively, plotted as the time to failure for the next embrittled bundle to fail versus the stress concentration factor. Also plotted are the measured failure times for the given stress-conditions. It can be easily demonstrated that if S_c was sufficient to fail the next embrittled bundle at the value measured, that the stress-concentration condition resulting on the neighboring bundles would be so great (since a would be doubled), that the whole composite would fail. In other words, if S_c was 4.2 for the 140 MPa condition in Figure 4.12 and the next embrittled bundle failed at 49 hours, the stress concentration on the new (and remaining old) nearest neighbors would be 5.3. A value exceeding what is required to immediately fail the next embrittled fiber (bundle). Therefore it can be assumed that once the next embrittled bundle fails, the composite fails.

The S_c values required for this to occur for MI composites are ~ 4.2 . In order to achieve this stress concentration, based on the parameters and assumptions in this analysis, τ and a would have to be large, e.g. 250 MPa and 0.5 mm, respectively. These values are probably larger than reality, but certainly τ for an interphase filled with a glass approaches that value.

For the CVI composites, a greater S_c is required for the lower applied stress conditions. It is estimated that a stress-condition of 130 MPa would require S_c to equal about 3 which could be achieved with $\tau = 200$ and $a = 0.28$. For the lower stress conditions, slightly larger τ 's and/or a 's would be required.

From this analysis it can be concluded that for the lower stress-conditions, a significant stress-concentration on the neighboring embrittled bundles would be needed to cause all the embrittled fibers to fail at once (e.g. ~ 4.4 for the 140 MPa rupture condition when the first fiber fails at 20 hours (Figure 4.12)). However, this value is not that much greater than the stress-concentration needed to cause progressive bundle failure.

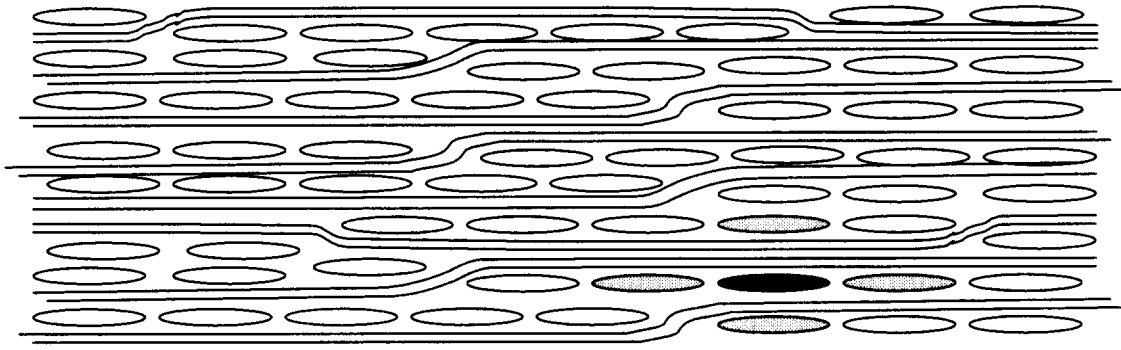


Figure 4.11: Schematic representation of five harness satin composite cross-section. Black bundle represents a failed bundle and grey bundles represent the nearest-neighbor bundles which share the load of the failed bundle.

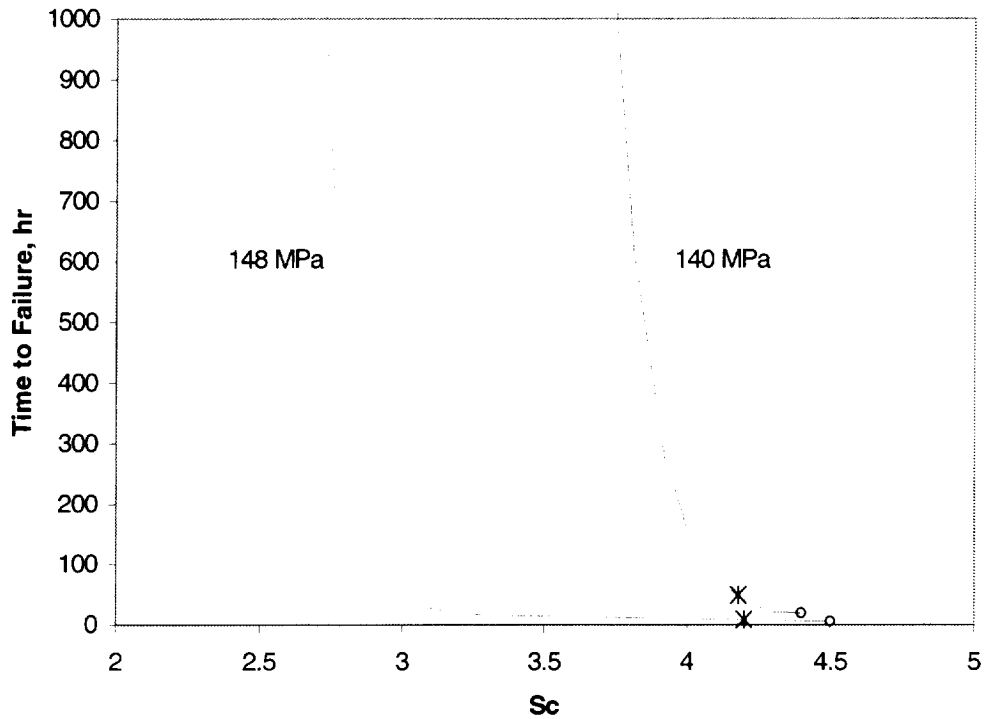


Figure 4.12: The effect of the stress concentration factor on the time to fail the second embrittled bundle in a matrix crack for MI composite rupture. The star data points indicate the measured rupture times for the composites. The circle data points indicate the time when the first fiber break was estimated.

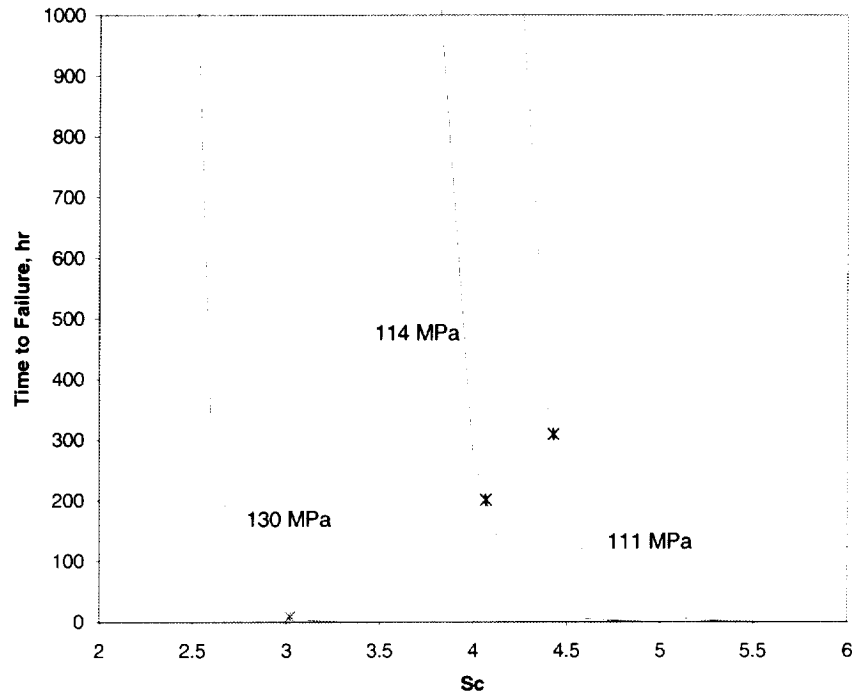


Figure 4.13: The effect of the stress concentration factor on the time to fail the second embrittled bundle in a matrix crack for CVI composite rupture. The star data points indicate the measured rupture times for the composites. All the curves were estimated to a minimum time to failure of 2 hours (the time to fully embrittle the cross-section of the composite). At least one fiber failure was estimated to occur prior to this time for each stress-condition.

4.5 Effect of Input Variables on Model

The model can be used to determine the effect different variables have on the predicted life of a composite under intermediate temperature stress-rupture. Two variables that are examined here and are important practically are the as-composited fiber strength and the amount of damage. The modeling approach of section 4.3.1 for the MI system was used for this analysis.

4.5.1 The Effect of σ_o

In the earlier models, the as-produced fiber strength was used for σ_o and $\sigma_{o(t,T)}$. During composite fabrication fiber degradation could occur that would result in a lower for σ_o and $\sigma_{o(t,T)}$. Figure 4.14 shows the effect of a 20% and 40% reduction in for σ_o and $\sigma_{o(t,T)}$. The run-out stress was lowered about 5% for the 20% lowering of σ_o whereas the run-out stress was lowered about 30% for the 40% lowering of σ_o . Evidently, moderate reductions in fiber strength result in minor strength degradation whereas greater reductions in fiber strength result in comparable strength degradation.

One interesting artifact of the model in general that did not appear in earlier predictions is the sharp drop in composite stress at approximately 20 hours in Figure 4.14. This is associated with a transition from two fiber breaks required to achieve ultimate composite failure (usually the case for the *Picture Frame* failure criterion) to only one fiber break required for ultimate composite failure (*Fully Oxidized Matrix Crack* failure criterion). If there was a more progressive crack growth nature to ultimate composite failure, the predicted stress-lifetimes probably will not be as severe as predicted here.

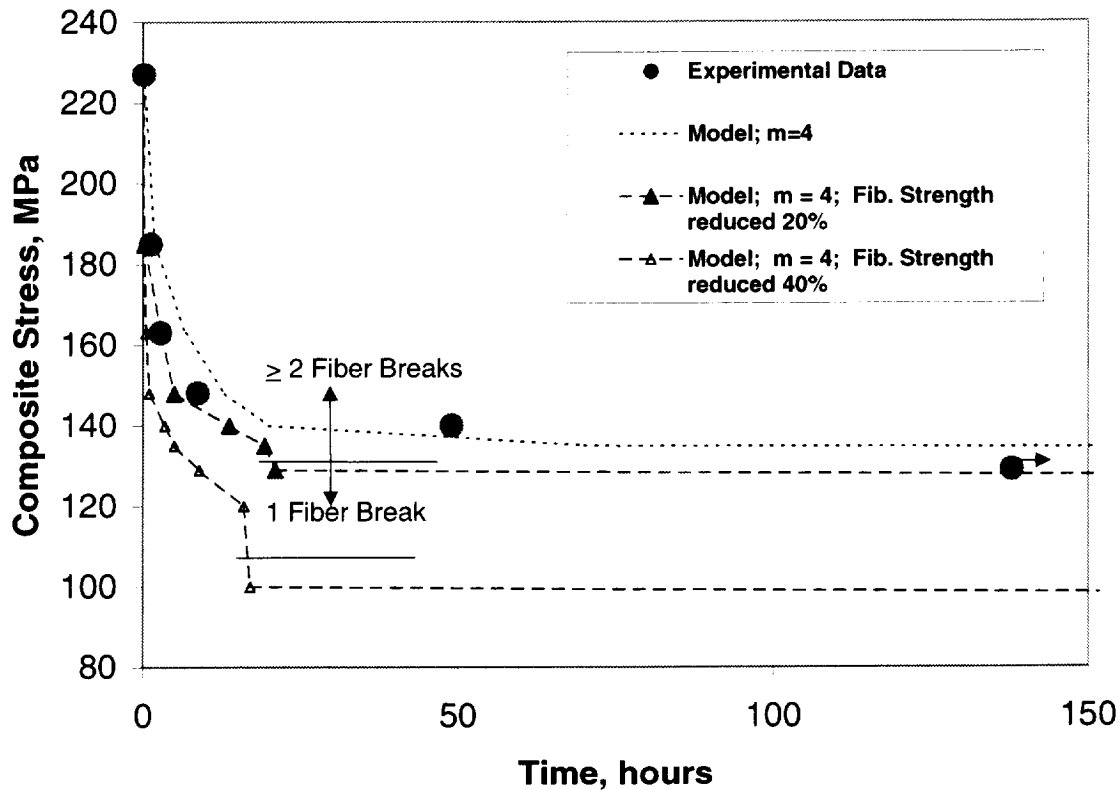


Figure 4.14: Rupture model with varying as-composited fiber strength.

4.5.2 The Effect of Precracking (Crack Density)

Another variable of practical importance is the crack density. During service, it is possible that an overstress condition could arise in a part that creates a higher crack density in a section of the composite than would be expected from just the use stress. Also, it can be conceived that perhaps an increase in crack density may have a beneficial effect if the reduction in S_c on the outer rim of fibers in a bundle offset the increase in effective fiber gage length. Figure 4.15 shows the predicted stress-rupture life for a fully precracked specimen. It was assumed that $S_c = 1$ for all the loaded fibers. This represents the opposite extreme crack density condition compared to the crack density that is just a function of applied load, time, and environment. The effect of the crack-density conditions is significant. Of course there is no effect at higher stresses since crack growth during the experiment resulted in matrix crack saturation. For the lower stress conditions where S_c can be as high as 1.5 for the original model, a 25% reduction in run-out stress is predicted. There was one precracked data point that did not fail at 111 MPa after 138 hours which is also plotted in Figure 4.15. Unfortunately, other precracked specimens could not be tested at slightly higher stresses to test the validity of the model. However, the prediction shows that increasing the gage length more than nullifies any gain from reducing stress concentrators at the outer rim of fiber bundles.

It should also be noted that the same multi-fiber break to single fiber break transition occurred for this modeling effort. Again, this is an artifact of the failure criterion for ultimate composite failure.

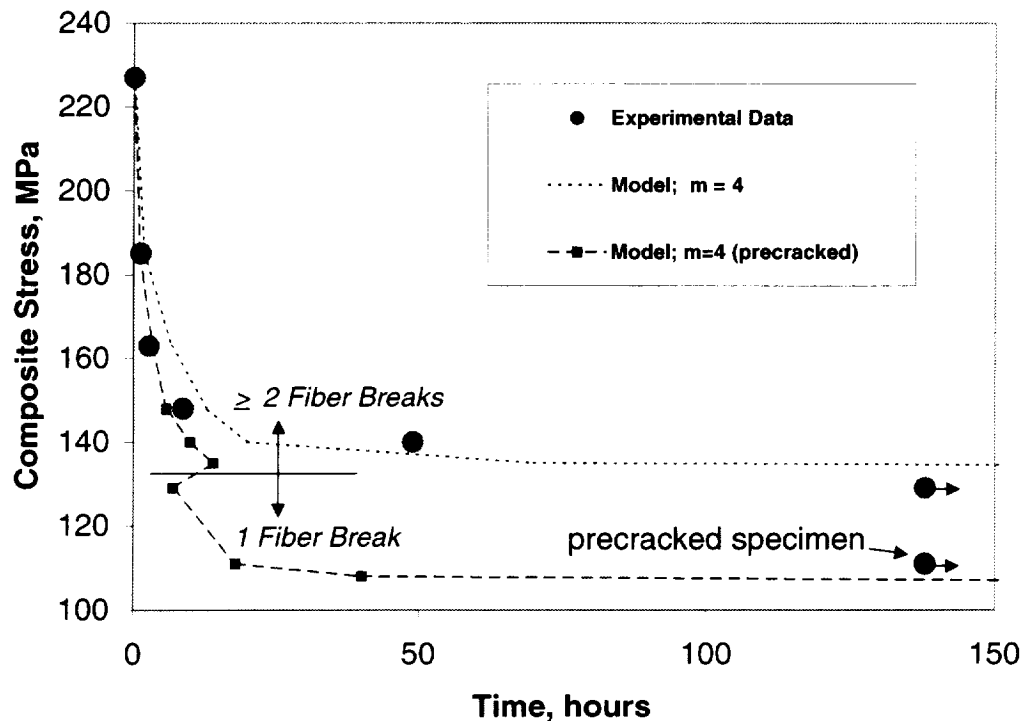


Figure 4.15: Rupture model with different crack densities.

4.6 Works Cited

1. N.S. Jacobson, S. Farmer, A. Moore, and H. Sayir, "High Temperature Oxidation Behavior of Boron Nitride Part I: Monolithic BN," *J. Am. Ceram. Soc.*, **82** [2] 393-8 (1999).
2. N.S. Jacobson, G.N. Morscher, D.R. Bryant, and R.E. Tressler, "High Temperature Oxidation Behavior of Boron Nitride Part II: BN Layers in Composites," *J. Am. Ceram. Soc.*, **82** [6] 1473-82 (1999).
3. C.G. Cofer and J. Economy, "Oxidative and Hydrolytic Stability of Boron Nitride – A New Approach to Improving the Oxidation Resistance of Carbonaceous Structures," *Carbon*, **33** [4] 389-95 (1995).
4. G.N. Morscher, D. Bryant, and R.E. Tressler, "Environmental Durability of Different BN Interphases (for SiC/SiC) in H₂O Containing Atmospheres at Intermediate Temperatures," *Ceram. Eng. Sci. Proc.*, **18** [3] 525-534 (1997).
5. A.W. Moore and S.L. Strong, "Variations in the Structure and Morphology of Pyrolytic Boron Nitride," *Ceram. Eng. Sci. Proc.*, **10** [7-8] 846-856 (1989).
6. N.P. Bansal and R.H. Doremus, Handbook of Glass Properties, Academic Press, Inc., 1986, p. 244.
7. T. Shimoo, T. Hayatsu, M. Takeda, H. Ichikawa, T. Seguchi, and K. Okamura, "Mechanism of Oxidation of Low-Oxygen SiC Fiber Prepared by Electron Radiation Curing Method," *J. Ceram. Soc. Japan (Int. Edition)*, **102** [7] 618-622 (1994).
8. E. Lara-Curzio, M.K. Ferber, and P.F. Tortorelli, "Interface Oxidation and Stress-Rupture of NicalonTM/SiC CVCCs at Intermediate Temperatures," Key Engineering Materials Trans Tech Publications, Switzerland. Vols. 127-131 pp. 1069-1082 (1997).
9. A.G. Evans, F.W. Zok, R.M. McMeeking, and Z.Z. Du, "Models of High-Temperature, Environmentally Assisted Embrittlement in Ceramic-Matrix Composites," *J. Am. Ceram. Soc.*, **79** [9] 2345-52 (1996).
10. E. Lara-Curzio, "Stress-Rupture of Nicalon/SiC Continuous Fiber Ceramic Matrix Composites in Air at 950°C," *J. Am. Ceram. Soc.* **80** [12] 3268-72 (1997).
11. W.H. Glime and J.D. Cawley, "Stress Concentration Due to a Fiber-Matrix Fusion in Ceramic-Matrix Composites," *J. Am. Ceram. Soc.*, **81** [10] 2597-604 (1998).
12. S.J. Zhou and W.A. Curtin, "Failure of Fiber Composites: A Lattice Green Function Model," *Acta Metall. Mater* **43** [8] 3093-3104 (1995).
13. M. Ibnabdeljalil and W.A. Curtin, "Strength and Reliability of fiber-Reinforced Composites: Localized Load-Sharing and Associated Size Effects," *Int. J. Solids Structures*, **34** [21] 2649-2668 (1997).
14. H.M. Yun and J.A. DiCarlo, "Time/Temperature Dependent Tensile Strength of SiC and Al₂O₃-Based Fibers," Ceramic Transactions Vol 74, Advances in Ceramic-Matrix Composites III, eds. N.P. Bansal and J.P. Singh. pp. 17-26 (1996).
15. G.N. Morscher, "Tensile Stress Rupture of SiCf/SiCm Minicomposites with Carbon and Boron Nitride Interphases at Elevated Temperatures in Air," *J. Am. Ceram. Soc.*, **80** [8] 2029-42 (1997).
16. J.W. Hutchinson and H.M. Jensen, "Models for Fiber Debonding and Pullout in Brittle Composites with Friction," *Mech. Mater.*, **9**, 139-63 (1990).

17. J. Lamon, F. Rebillat, and A.G. Evans, "Microcomposite Test Procedure for Evaluating the Interface Properties of Ceramic Matrix Composites," *J. Am. Ceram. Soc.*, **78** [2] 401-405 (1995).
18. Z.C. Xia, J.W. Hutchinson, A.G. Evans, and B. Budiansky, "On Large Scale Sliding in Fiber-Reinforced Composites," *J. Mech. Phys. Solids*, 42 [7] 1139-58 (1994).
19. A.G. Evans, F.W. Zok, R.M. McMeeking, and Z.Z. Du, "Models of High-Temperature, Environmentally Assisted Embrittlement in Ceramic-Matrix Composites," *J. Am. Ceram. Soc.*, **79** [9] 2345-52 (1996).
20. G.N. Morscher and J. Martinez-Fernandez, "Fiber Effects on Minicomposite Properties for Several Silicon Carbide Fiber – Chemically Vapor-Infiltrated Silicon Carbide Matrix Systems," *J. Am. Ceram. Soc.*, 82 [1] 145-55 (1999).

5.0 DISCUSSION

The results of this study clearly show that time-dependent life of SiC/SiC composites, with BN interphases under constant stress at intermediate temperatures in air, is controlled by several factors:

- (i) Interphase stability – Without the poor resistance of BN to oxidation and attack by water vapor in the atmosphere, these composites would not have an intermediate temperature problem. This, of course, has been well documented and modeled elsewhere [1,2]. One factor demonstrated in this study is that only the thinnest portion of a BN interphase separating two fibers needs to be oxidized as opposed to an entire interphase to a certain depth.
- (ii) The damage state of the matrix – Certainly for MI composites, postponing through-thickness cracking to higher stresses enables longer rupture life to higher stresses for Regime II rupture. For stress rupture in the lower stress-range, the growth of microcracks permits or allows the environmental attack of the BN interphase.
- (iii) The architecture of a woven macrocomposite – Woven architectures, though desirable from a fabrication and design standpoint, introduce two critical life-reducing effects for intermediate temperature stress rupture. First, fibers in a given tow are in intimate contact with one another enabling strong bonding in a short period of time after exposure to the atmosphere. Second, the presence of 90° bundles and large matrix-only regions result in large unbridged crack areas which leads to fairly large stress-concentrations on the outer-rim of fibers in a load-bearing bundle in a matrix crack. This is the likely mechanism that triggers the first fibers to fail at lower applied stresses. These two architectural issues are most likely the reasons why macrocomposite stress rupture is considerably worse than single-tow minicomposite stress rupture. For minicomposites, the fibers are aligned in a unidirectional manner and no large unbridged crack areas exist and fibers are fairly well spread apart from one another and separated from the matrix by a thicker layer of BN.

The combination of these factors ultimately leads to failure of all the load-bearing fibers in a matrix crack and ultimate failure of the composite. The last two issues and some of the observations from this study will be discussed in the next two sections. Finally, some implications will be discussed for SiC/SiC and oxide ceramic matrix composites, since some of the phenomena leading to intermediate temperature embrittlement may be relevant to oxide-containing composites.

5.1 Matrix Cracking and Crack Opening During Rupture Testing

It is evident from the measured crack densities (Figures 3.8 and 3.9) and the AE data (Figure 3.6) that matrix cracks are growing and/or new matrix cracks are forming above ~ 600°C in the MI matrix composites during the rupture test. In addition, very few broken fibers were ever observed in the matrix cracks (from polished longitudinal sections). Therefore, it can be assumed that most of the matrix cracking is not due to fiber breakage in the matrix crack. Rather, the stress-intensity at the crack tip must be raised by some other mechanism, for example slow crack growth of the matrix SiC at the crack tip, crack opening due to a lowering of τ in the bridged crack wake, crack opening due to recession of the interphase in the bridged crack wake, and/or oxide product formation in the matrix crack at the crack tip or in the crack wake to produce a wedging stress.

New cracks emanating from flaws or the growth of non-through thickness microcracks would have to occur to account for the increase in observed crack density. It was observed for the Regime II specimens that cracks emanated from the surface and grew into the composite. This confirms the need for access of the environment into a matrix microcrack to cause crack propagation. It does not shed any light on whether new cracks can form. It can be assumed that a number of 90° cracks and/or cracks in matrix only regions exist which are blunted by the 0° bundles [3] as well as other non-through thickness cracks which are bridged by some 0° bundles. Some of this is discussed in Appendix A. One pertinent set of data from Appendix A is the overestimation of matrix cracking from the cumulative AE energy approach. The best explanation for this is that the “extra” AE activity can be accounted for in the creation of many more tunnel cracks than 0° cracks at lower stresses and strains. Therefore, it can be concluded that many 90° microcrack-sites available for growth exist.

One additional fact to consider is the increase in strain with time during the rupture experiment. The data from Figure 3.3 is plotted in Figure 5.1 as strain versus time for several of the MI rupture specimens. For the three specimens not precracked, the time vs. strain data looks very much like creep data. There is little if any creep occurring in the fibers at these temperatures so the extension occurring during the rupture test is only due to matrix cracking and matrix crack opening. Comparing this with some of the AE data, e.g. 3.7, where after about 15,000 seconds (~ 4.1 hours) the rate of AE activity and energy slows down considerably. This does appear to correspond with a slow down in the rate of strain accumulation for the 148 MPa sample in Figure 5.1. However, significant strain accumulation does occur after this point. Therefore, it appears that most, but not all, matrix crack propagation and crack-opening occurs in the first hours of the rupture test.

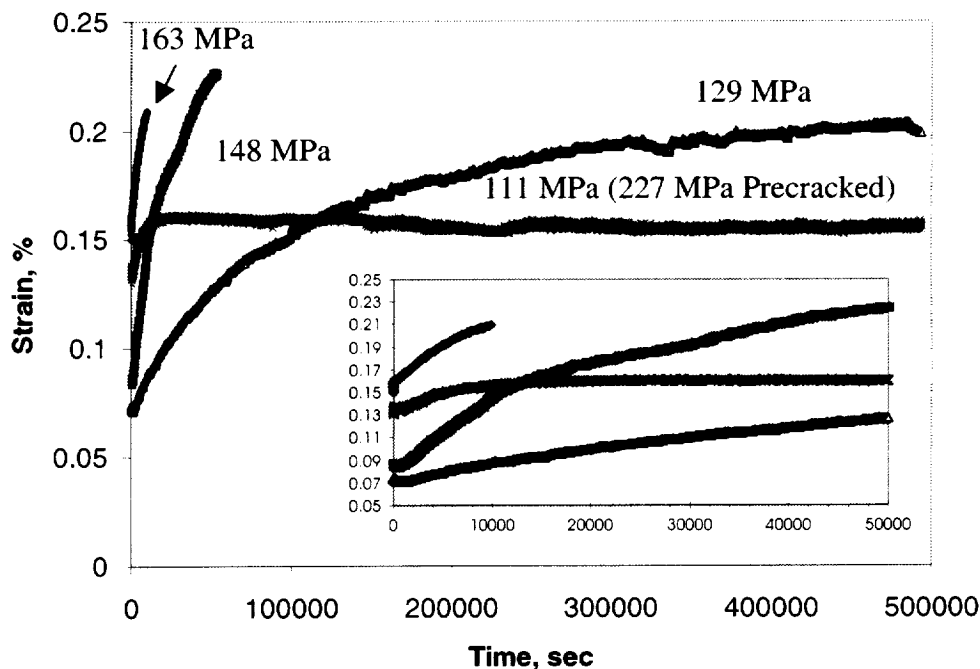


Figure 5.1: Strain versus time for the constant applied stress portion of the stress-rupture tests on some MI matrix composites.

For the precracked specimen, all the extension at constant stress occurs in the first three hours. After that, no extension occurs. Some matrix cracking (Figure 3.9) may have occurred during the rupture experiment. However, some of the time-dependent extension may be due to increased crack opening. If there were no increase in matrix cracking (one extreme), the amount of extension would correspond to approximately a 40% increase in inelastic strain (crack opening displacement). This would correspond to the maximum amount of increased crack opening during a rupture experiment. Considering these results, the mechanisms causing matrix crack propagation/formation and matrix crack opening can now be addressed.

Slow crack growth in SiC has been reported at higher temperatures ($\geq 1200^{\circ}\text{C}$) [4,5]. The fact that there is a reduction in strength for all the SiC fiber-types, albeit a minor reduction, under stress-temperature conditions at the intermediate temperature regime implies slow crack growth also occurs at intermediate temperatures (Figure 1.1) [6]. This has not been reported in the literature before. The reason for this is probably that the stresses that the fibers are tested at are in excess of 1.5 GPa. If this mechanism is stress-activated, as Easler et al. [4] suggest, it is possible that this phenomenon would not be observed in larger samples because they usually only have a starting strength of 500 to 700 MPa. This would also imply that the slow crack growth in the SiC matrix could not be activated because the stress on the matrix is too low, less than 250 MPa for all the specimens tested in this study.

Crack opening in a non-through thickness matrix crack due to a reduction in τ in the bridged fiber interphases and/or BN interphase recession is more likely. Since a carbon layer exists between the BN and the fiber, and it volatilizes first, τ should effectively be lowered before the formation of enough oxidation product to strongly bond the fiber to the matrix. With longer times, the BN interphase is replaced with an oxide reaction product (Figure 3.11c). Wang and Luthra [7] have measured BN recession in similar composites at 700 and 900°C in dry air. For the longer times, the BN recedes a few microns. During this process, it would be expected that the reaction product is a liquid and unable to transfer load from the fiber to the matrix. Therefore, it is quite likely that some crack opening would occur in an exposed microcrack due to these phenomena and resulting in crack growth. After a crack propagated through the thickness of the specimen, these same processes would continue to open the crack wider. In a newly formed matrix crack or crack extension, the borosilicate oxidation product would be so depleted in boron within a few hours that it would be very viscous, and capable of transferring load to the matrix if not strongly bonded to the matrix. However, each time a microcrack grew, this process would begin again with the newly exposed BN interphases.

One other possible mechanism would be the increased volume of an oxidation product formed in the matrix crack. This would act so as to wedge the crack open. Although a significant amount of oxide product is observed in matrix cracks after longer times (Figure 3.11 b and c), this mechanism is deemed least likely. In order for a solid oxide product to form and grow large enough to fill a crack would require hundreds of hours on pure SiC. A greater amount of borosilicate glass could be produced in a few hours; however it would take at least a couple of hours to remove enough boron from the borosilicate oxidation product to make it rigid enough to cause a stress on the crack tip. Even if this did occur it is expected that the oxide product would have flowed to relieve any compressive “growth” stress in the oxide product prior to rigidizing.

For some of the lower stress (129 to 148 MPa) rupture specimens, little if any cracking was observed in the “colder” regions of the specimens. The fact that cracks do grow from the surface inward and that a significant amount of AE activity had occurred during loading implies that some surface cracks, at the very least, did exist. It is also possible that cracks had closed and

were difficult to observe, even with etching. It is very possible that, at these stresses, many of these surface cracks did not fully penetrate the 0° bundles and would therefore not be counted during crack density measurements. The cracks exposed to higher temperatures are probably easier to observe because they are larger and more open due to the reduction in τ and BN recession.

5.2 Modeling Stress-Rupture and the Role of Stress-Concentrators

The modeling effort in this study though, limited in its mathematical sophistication, produced good agreement between the predictions and measured stress-rupture data for the MI composite system. There was less agreement for the CVI woven composite system. The reason for the good agreement for the MI matrix system was probably because the damage-state and environmental ingress into the matrix crack was fairly well characterized experimentally. These two factors could only be estimated for the woven CVI composite. The unidirectional CVI minicomposites, although the simplest of the three composite systems, was the most difficult to model. The experimental data used was determined at a higher temperature (950°C) compared to the woven systems. The only fiber weakening mechanism used for this system was taken from Yun and DiCarlo [6]. It is likely that fibers could be further weakened at this higher temperature due to the much more prevalent formation of oxide reaction products which are not only thicker on the fibers, but also bond fibers to the matrix.

Some of the limitations and assumptions used in the models are discussed in the following. Even with these simplifications and inaccuracies, the modeling effort yielded some insight into the extent of fiber failure and the need for stress-concentrators to trigger intermediate temperature rupture.

5.2.1 Individual Fiber Failure and Stress Concentrators

It was shown that not enough fiber failure could occur based on the model with the assumption of each fiber acting independently at the applied stresses to cause ultimate composite failure. However, based on the experimental observations, it appeared that when one fiber failed in an embrittled bundle, the bundle failed since nearly all of the fibers were interconnected. Estimates of fiber failures in the hot zone section of the composite specimens were made based on the number of cracks and crack opening displacements. For MI matrix composites subjected to the higher stresses (≥ 185 MPa), tens and hundreds of fibers would be expected to fail somewhere in the hot section of the composite (Figure 4.2). Therefore, it is not surprising that these composites failed within a few hours. For the lower stress conditions, few if any fibers would be expected to fail in the measured rupture times at the applied experimental stresses. Consequently, there is a need for stress-raisers to trigger embrittled fiber failure.

The stress-concentration employed was that determined to be on the rim of fibers at the bridged-unbridged matrix crack [8]. When incorporating this stress-concentration into the population of outer rim fibers (about one third the number of interior bundle fibers) it was found that the number of fiber failures increased significantly. Figure 4.6 shows that the number of outer rim fibers for the 140, 148, and 163 MPa rupture conditions nearly equals or is greater than interior bundle fibers even though there were one-third the number of outer rim fibers compared to interior fibers.

It was assumed in the model that the gage length of loaded fibers was made up of the cumulative crack-openings in the hot zone section. This was based on the observation of no pullout in the embrittled bundles. It can be argued that the actual stress-profile along the length

of the fiber would be the same as that with the BN interphase in tact (see Appendix B). It would then be expected that a number of fibers could fail in the “sliding length” region away from the matrix crack (scenario 2 in Figure 4.2). The probability for fiber failure when the sliding zone was included in the calculation was found to be about twice the probability for fiber failure in the crack opening. Therefore, it is quite possible that the fiber failure that would trigger embrittled fiber failure would be in the sliding zone. This could only occur if the oxidation product was not strong enough to allow interfacial failure and sliding to occur between the fiber and matrix after fiber failure. The rest of the fibers would fail in the matrix crack because of the stress concentration created by the nearest-neighboring broken fiber and strong fiber-to-fiber bond.

The stress concentrations on the outer-rim of the fibers are calculated to be more critical for CVI SiC macrocomposite rupture. The applied fiber stresses are lower so fibers are less likely to fail without a stress concentration.

It is interesting to note that the rates of rupture (faster rupture rates at high stresses and slower rates at lower stresses) are approximately the same for MI and CVI composites. Even though the CVI macrocomposite have cracks through the thickness of the composite. Normalizing the composite stresses by the fraction of fibers in the loading direction (Figure 5.2) compares the average stress on fully loaded fibers for the three Hi-Nicalon reinforced composites. The Regime II stress range for the material tested in this study is almost as low as for the CVI SiC matrix composites. It may be that the CVI SiC matrix system approaches a minimum fiber-loading stress range for composite rupture. Higher Regime II stress-ranges would be due to fewer and/or non-through thickness matrix crack states. This would have to be confirmed with further experiments but if true, a minimum failure stress range for these systems (based on Hi-Nicalon reinforcement) could be used as a baseline for design purposes.

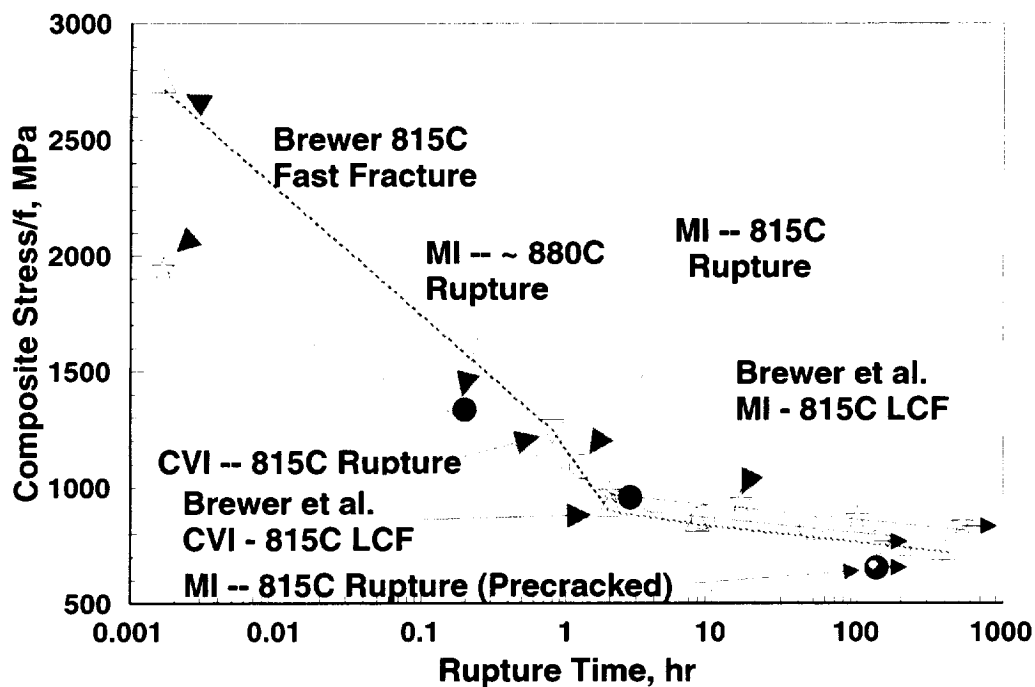


Figure 5.2: Composite stress normalized by volume fraction of fibers in the loading direction for the HN macrocomposite rupture and LCF data.

5.2.2 The Assumptions

The assumptions inherent in the modeling effort can be broken down into two categories. First are the governing equations used to determine values necessary for the lifetime model itself. The second category would be experimentally measured or approximated values used in the model or the governing equations themselves. Both categories of variables will be discussed with respect to their accuracy and potential for improvement.

Several equations were used to model parameters necessary for modeling intermediate temperature embrittlement. The ultimate lifetime comes down to the simple Weibull equation and the likelihood a fiber will fail given the number of fibers available. The important parameters then become the effective gage length for fiber loading, the applied stress, and the reference stress as a function of time and temperature. The governing equation were used directly or indirectly to determine the parameters in the Weibull formulation for life expectancy. These included experimentally-based (empirical) relationships, e.g. area of embrittlement (for MI composites) and fiber weakening, and model-based equations, e.g. crack-opening displacement and stress concentration factors.

Experimental-based relationships are considered to give the most accurate values into the life-time equations. This would especially be true for the rate of embrittlement due to the oxidation reactions occurring between the interphase and environment through the thickness of a composite via a surface-exposed matrix crack. This is most important for the high stress, short-time rupture conditions. The other experimental-based relationship used was the fiber weakening for time-temperature exposure under constant stress [6]. This is the only known relationship for these fibers. Unfortunately, it assumes a constant applied stress on the fibers. In reality, as areas of the composite embrittle and fracture resulting in load shed to remaining bridging fibers, increasing stress conditions will occur on those remaining fibers. This variable stress condition for fiber life is unknown and would be a source of improvement with more appropriate stress conditions to composite rupture.

Other sources of fiber weakening should also be taken into account if they exist. For example, any fiber weakening due to oxidation of the fibers. This could correspond to local oxidation effects due to the enhanced oxidative processes occurring from BN oxidation.

The determination of crack openings is based on a model by Hutchinson and Jensen [9] for unidirectional composites. It would be expected that some differences in crack opening may occur for a 0/90 woven composite. This would affect the gage length used in the Weibull relationship.

Related to this is the model used for the stress concentrators on the outer-rim fibers which exist at the bridging fibers nearest unbridged regions of a matrix crack [8]. For this model, a 0/90 lay-up is assumed, so the unbridged portion of a crack is expected to go through the width of the specimen. In reality, the unbridged matrix crack regions will be bridged on all sides by 0° bundles (except for surface cracks) so the unbridged crack dimensions would be smaller resulting in a lower stress-concentration. Also, in this model, a stress-concentration was applied to the outer rim of fibers. In reality, a varying amount of stress-concentration across the bundle would occur (Figure 4.3). Halverson and Curtin [10] have modeled this for a certain non-through thickness condition and calculate this variable stress-concentration with some of the interior fibers loaded at stresses below σ/f . A more accurate model would integrate the spectrum of stress-concentration states for the fibers affected. This would influence the life-time model at lower stresses with lower crack-densities.

Another area where the nature of local stress-concentrations should be explored is for the local condition around individual fiber break and individual bundle breaks. Better understanding of this may or may not show that there is a more progressive nature to crack growth than demonstrated by the modeling results of this study. The fact that significant AE activity occurs over the entire test definitely implies matrix crack growth. This may be due to bridged crack growth from microcracks in 90° plies. It could also be due to crack growth due to failure of embrittled bridging fibers or bundles.

Finally, the approach taken in Appendix B for the sliding portion of the fiber length could more accurately be modeled. Curtin [11] is currently working on such a model numerically integrating the stress along the sliding length with the reference stress condition.

The measured or approximated variables used in the governing equations or Weibull formulations themselves are σ_0 (at room temperature), crack density, τ , m , and a . σ_0 and “ a ” were assumed from the as-produced fiber strengths and unbridged regions between plies. Crack density was measured for MI composites and approximated for the CVI matrix composites. τ was approximated from hysteresis loops performed at room temperature. A range of m was used in the models; however, a value of 4 was used for most comparisons and was within the range of values measured from fiber fracture mirror results.

“ σ_0 ” could be lower due to fiber weakening as a result of composite processing. If so, all the reference strengths would be lower and shorter lifetimes would be expected as shown in Figure 4.14.

“ m ” was shown to mostly affect the lower stress lifetimes. m equal to 4 corresponded to the high-end of the m values measured from the different fracture mirror populations. A lower m would be expected to shorten the lifetimes for lower-stress conditions (Figure 4.5).

“ τ ” was the one variable from this set that could change as a function of time and temperature. A change in as-produced composite τ would directly affect the number of matrix cracks as well as crack opening. The oxidation reactions occurring at the fiber-matrix interphase has been discussed above and the effect on τ . The net result could be a lowering of τ , at shorter times, the growth of microcracks, and an increase in the effective gage length. Figure 4.15 shows the reduction in life times predicted for the MI composite system if matrix crack saturation is reached prior to or during the rupture test.

The value for “ a ” used was based on a simple representation of the five harness satin architecture. It is conceivable that larger a values could be achieved at locations where two 90° plies are next to each other and where there are large regions of matrix. Also, for the eight harness satin architecture of the CVI SiC composites, this effect would even be more likely. The net effect of increasing a would be an increase in the stress-concentration on the outer-rim of fibers.

5.3 Implications for Woven SiC/SiC Composites

The most significant result of this study is the understanding that intermediate temperature embrittlement in woven SiC/SiC composites with BN interphases is due in large part to two structural attributes of woven composites themselves in combination with the well-known environmental reactions. First, individual fibers in the load-bearing bundles are characterized by near fiber-to-fiber contact and second, the large stress-concentrators exist at bridged/unbridged regions of a matrix crack.

Near fiber-to-fiber contact is due to “tight” sized bundles which are woven into fabric. The nature of this process yields nearly all of the fibers in intimate contact (approximately 50 nm separation) with at least one neighboring fiber. The prevalence of fiber closeness has little or no effect on the ultimate strength of the composites. However, it only takes one hour at temperature, under load, to reduce the strength to about half the ultimate strength.

The embrittlement process is controlled mostly by the rate of BN oxidation that is enhanced at these near fiber-to-fiber contact regions. If more uniform ($\sim 0.5 \mu\text{m}$) BN layers could be applied without the near fiber-to-fiber regions, this process is expected to be slowed down and is probably why the rupture properties of minicomposites, with thicker and more uniform BN interphases, are superior to macrocomposite rupture properties at intermediate temperatures. More uniform interphases could possibly be achieved by weaving already coated tows or by using processing/fabrication approaches that separate the fibers.

The presence of large stress concentrations on the outer fibers in an embrittled bundle next to an unbridged region of a matrix crack is the most likely “trigger” for embrittled fibers to fail at the lower stresses. For the shorter time, higher stress rupture conditions it was shown that many fibers are expected to fail throughout the embrittled bundles due to the stress-rupture properties of the individual fibers themselves. However at the lower stresses, few if any fibers are expected to fail if global load-sharing conditions existed. The only plausible mechanism that could effect enough fibers in a reproducible way would be the stress-concentration on the bridging fibers at the unbridged crack border.

The modeling effort and some of the assumptions and approaches used to obtain stress-concentration factors were discussed above. There is much room for improvement in determining the actual stress-state for the outer rim of bridging fibers. However, one factor that directly affects the magnitude of the stress-concentration would be the size of an unbridged region. If the size of unbridged regions could be reduced, the stress-concentrations would be minimized. One way to reduce the bundle size would be to use fewer fiber-count tows. This would result in more bundles in the loading direction and a greater number of plies for the same thickness and volume fraction of composite. If the aspect ratio of bundles could be increased, a similar effect would result.

One source of stress-concentration not considered in this study, but certainly present in woven structures, would be that associated with bent fibers in the matrix crack. Fibers with off-axis loading and potentially pinned at a crack surface could also be another source for triggering embrittled fiber failure.

It was shown that cracks do grow, even at the lower stresses that are considered to be below the 0° onset stress. The empirical finding that the run-out stress corresponds to the 0° onset stress (Figure 5.3) may be serendipitous. What controls the onset of rupture more, the extent of 0° cracking, the stress state on the fibers, or a combination of both? Certainly, for MI matrix composites, the damage state does play a role (Figure 3.4 and 5.2); however, for CVI matrix cracks, the matrix contains through thickness cracks but rupture behavior is similar at lower stresses. The modeling approach also demonstrated that as applied stresses were reduced, the likelihood for fiber failure was reduced to the extent that at the run-out stress condition no fiber failure is expected even with the significant stress-concentrations on outer-rim fibers. Therefore, the run-out condition is probably a combination of both factors. One important implication for crack growth is that even though the composite may not ever fail at temperature, the composite can never experience a stress greater than that stress at room or high temperatures without catastrophic failure. In other words, poor retained strength.

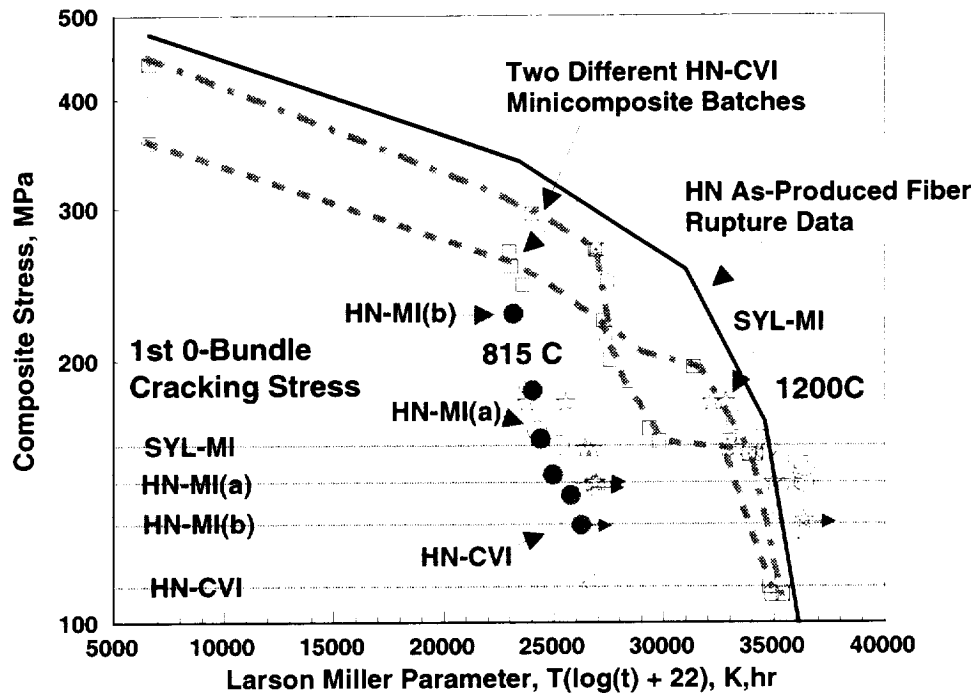


Figure 5.3: Larson-Miller plot from Figure 1.14 with data from this study (HN-MI(b)).

Figure 5.3 does demonstrate that the higher modulus SYL fiber reinforced MI composites are superior in rupture properties to Hi-Nicalon reinforced MI composites (Figure 5.2) at intermediate temperatures. There are a number of factors why this is the case. First, the rupture properties of the individual fibers at 815°C are greater than Hi-Nicalon (Figure 1.1). Second, the interfacial shear strength of SYL, MI SiC composites is much higher than HN MI-SiC. This would result in more cracks but significantly shorter sliding regions and shorter gage lengths for fully loaded fibers*. Thirdly, the stress range where matrix cracking occurs is higher than for HN-matrix composites. This is due to a stiffer fiber, a higher τ , and a mild compressive stress in the matrix of these materials [12]. Fourthly, since the SYL fiber does not decompose during MI processing, a carbon layer between the interphase and the fiber is absent. However, this last factor has been shown to not be a great benefit to HN-CVI SiC composites, so the first three factors are probably most important for the superior rupture performance of SYL-MI composites.

Summarizing for the Hi-Nicalon/BN/MI composite system in particular and the SiC/BN/SiC system in general, the characteristic intermediate temperature degradation of rupture properties observed for these composites are a combination of environmental attack causing strong fiber-to-fiber bonding and the inherent geometrical attributes of a woven structure which causes stress-raisers on the outer rim of load-bearing fibers. If the environmental attack in the form of the oxidation of the interphase did not occur, the woven structure would not be an issue because the interfacial shear stresses would be low enough to result in matrix crack saturation

* Sylramic-MI composites are observed to have three to five times more 0° cracks[12]. Therefore, based on a $\tau = 100$ MPa for Sylramic composites, a composite stress of 250 MPa, and a crack density four times as great in the Sylramic composite, the effective gage length of fiber loading would be approximately two times greater in the Hi-Nicalon-MI composite.

and the elimination of the stress-concentrators. Therefore, this is usually considered to be an issue for “non-oxide” composite systems only and is one of the motivating factors for development of oxide composite systems. However, as will be discussed below, there may be scenarios where similar degradation in rupture properties could occur for oxide composite systems.

5.4 Implications for Oxide Composite Systems

There has been and continues to be some work towards developing oxide fiber, matrix, and interphase composite systems [13-15]. Interestingly enough, the intermediate temperature degradation which occurs in non-oxide composite systems may also occur in oxide composites if the oxide composite consists of a woven architecture, a fairly high interfacial shear stress, e.g. ~ 100 MPa, and a dense matrix. The rupture properties of individual oxide fibers are even worse than non-oxide fibers [6] not only in absolute strengths but oxide fibers also have higher rupture rates for temperatures above ~ 800°C. This would result in the reduction of $\sigma_{o(t,T)}$ with time at temperature increasing the probability for fibers to fail. The source of stress-concentrators, 90° bundles and large matrix regions, are inherent to the woven architecture and are therefore present just as they are for the non-oxide systems. If the matrix is dense and continuous, the same sort of stress-concentration should occur at the outer row of bridged fibers in load-bearing bundles.

The key to intermediate temperature degradation for dense oxide composites will probably be the magnitude of interfacial shear stress. If τ can be low enough to promote global load sharing intermediate temperature degradation will probably be minimized. A high τ could lead to severe intermediate temperature degradation because of the stress-concentration effects coupled with the fact that oxide fiber strengths are poorer than SiC fiber strengths which would further limit their load-carrying capability.

Some oxide systems may avoid these problems for another reason. For example, several systems are fabricated with matrices that are very porous, almost granule-like [13]. The matrix in these systems do not really “crack”, it essentially disintegrates. Therefore, one would not expect large stress-concentrators to exist due to unbridged cracks.

Unfortunately, what is raised here is merely speculation. However, oxide composite systems are nearing the stage of development where some of these issues can be explored.

5.5 Works Cited

1. G.N. Morscher, D.R. Bryant, and R.E. Tressler, “Environmental Durability of Different BN Interphases (for SiC/SiC) in H₂O Containing Atmospheres at Intermediate Temperatures,” *Ceram. Eng. Sci. Proc.*, 18 [3] 525-34 (1997).
2. N.S. Jacobson, G.N. Morscher, D.R. Bryant, and R.E. Tressler, “High-Temperature Oxidation of Boron Nitride: II, Boron Nitride Layers in Composites,” *J. Am. Ceram. Soc.*, 82 [6] 1473-82 (1999).
3. G.N. Morscher and J.Z. Gyekenyesi, “Room Temperature Tensile Behavior and Damage Accumulation of Hi-Nicalon Reinforced SiC Matrix Composites,” *Ceram. Eng. Sci. Proc.*, 19 [3] 241-249 (1998).
4. T.E. Easler, R.C. Bradt, and R.E. Tressler, “Strength Distributions of SiC Ceramics After Oxidation and Oxidation Under Load,” *J. Am. Ceram. Soc.*, 64 [12] 731-34 (1981).

5. S.R. Choi, J.A. Salem, and N.N. Nemeth, "High-Temperature Slow Crack Growth of Silicon Carbide Determined by Constant-Stress-Rate and Constant-Stress Testing," *J. Mater. Sci.*, 33, pp. 1325-1332 (1998).
6. H.M. Yun and J.A. DiCarlo, "Time/Temperature Dependent Tensile Strength of SiC and Al₂O₃-Based Fibers," pp. 17-26 in Ceramic Transactions, vol. 74, Advances in Ceramic-Matrix Composites III. Edited by N.P. Bansal and J.P. Singh. American Ceramic Society, Westerville, OH, 1996.
7. H.Y. Wang and K. Luthra, unpublished data.
8. Z.C. Xia, J.W. Hutchinson, A.G. Evans, and B. Budiansky, "On Large Scale Sliding in Fiber-Reinforced Composites," *J. Mech. Phys. Solids*, 42 [7] 1139-58 (1994).
9. J.W. Hutchinson and H.M. Jensen, "Models of Fiber Debonding and Pullout in Brittle Composites with Friction," *Mech. Mater.*, 9 139-63 (1990).
10. H. Halverson and W. Curtin, unpublished research.
11. W. Curtin, private communication.
12. G.N. Morscher, J.Z. Gyekenyesi, and R.T. Bhatt, "Damage Accumulation in Woven SiC/SiC Composites," submitted to *Environmental, Mechanical, and Thermal Properties and Performance of Continuous Fiber Ceramic Composite (CFCC) Materials and Components*, *ASTM STP 1392*.
13. C.G. Levi, J.Y. Yang, B.J. Dalgeish, F.W. Zok, and A.G. Evans, "Processing and Performance of an All-Oxide Ceramic Composite," *J. Am. Ceram. Soc.*, 81 [8] 2077-86 (1998).
14. X. Gu and E.G. Butler, "Alumina Woven Fibre-Reinforced Composites Produced by Directed Melt Oxidation," *Ceram. Eng. Sci. Proc.*, 18 [3] 371-378 (1997).
15. L.P. Zawada and S.S. Lee, "The Effect of Hold Times on the Fatigue Behavior of an Oxide/Oxide Ceramic Matrix Composite," Thermal and Mechanical Test Methods and Behavior of Continuous-Fiber Ceramic Composites, ASTM STP 1309, eds. M.G. Jenkins et al., American Society for Testing and Materials, pp. 69-101 (1997).

6.0 CONCLUSIONS

Based on the findings of this study, several conclusions can be made:

1. Stress rupture of Hi-Nicalon, BN interphase, SiC matrix composites tested at intermediate temperatures in air occurs at stresses considerably lower than expected if due to degradation of the fibers alone. Three factors were concluded to cause this degradation in addition to the known thermochemical reactions:
 - The ease with which individual fibers can fuse to one another due to their close proximity to one another.
 - The amount and nature of matrix cracking for a given applied stress.
 - The presence of large unbridged regions of matrix cracks which cause stress-concentrators on the outer rim of fibers in a load-bearing tow.
2. Even though these composites do degrade in strength with time at stress and temperature, they still possess significant load carrying ability, ~ 130 MPa, for long times (hundreds of hours).
3. The stress-rupture properties of these composites could be modeled accurately if the damage-state for a given stress and the time-temperature degradation for fibers were known. The model was based on probabilistic predictions for individual fiber failures and subsequent catastrophic failure of neighboring embrittled fibers due to the strong bonding of these fibers to one another.
4. The retained strength of composites which do not fail at lower stress conditions are severely degraded in strength when tested again at room temperature. The cause of this is the growth of microcracks, which may not even bridge load-bearing fibers initially, during the rupture experiment that enables the environment access to the fibers and interphases resulting in strong bonding of the fibers to one another. This embrittlement would be expected to have a deleterious effect on the thermomechanical fatigue life of these composites.
5. Modal acoustic emission is an effective means to monitor and locate accurately the damage accumulation and eventual failure location of SiC/SiC composites at elevated temperatures.

Finally, based on the findings of this study, several recommendations can be made to improve this composite system:

- (1) more stable interphases than CVI BN,
- (2) greater separation distances between individual fibers,
- (3) smaller unbridged matrix crack areas,
- (4) more stable fibers that do not decompose to produce carbon layers on their surface, and
- (5) higher matrix cracking stresses.

APPENDIX A: MODAL ACOUSTIC EMISSION - AE ENERGY AS A MEANS TO QUANTIFY TRANSVERSE MATRIX CRACKING

The reception of an acoustic emission signal from a failure event may have several unique characteristics including the amplitude or intensity of the waveform and the frequency spectrum of the waveform. This is discussed in the introduction. There are really two entities one would be like to discern from AE: the location and the identity of the source event. It has been shown that the former can be easily determined in section 3.2 and reference 1 with modal AE. It would be especially useful if one could identify a source event as a transverse matrix crack, a longitudinal matrix crack, the sliding between a fiber and the matrix, or a fiber break. Some attempts have been made towards this aim [2-6] using traditional acoustic emission. However, some of the weaknesses of this approach are discussed in section 1.2.3 and reference 1.

Since, for modal AE, the actual waveform of the source event is captured, the potential for sorting events into different categories based on their frequency contents, modal contents, location, and intensities offers a real potential for identification. Some attempts have been made in this regard with some success [1]. The problem with identification in CMC's comes with the difficulty in verifying what one is hearing in a composite since so many different entities can be fracturing and/or sliding at the same time^{*}. In addition, the waveform is dependent on the source, the density of the medium the waveform travels through, and the dimensions of the medium the waveform travels through. An advantage of typical tensile bars is that they are thin plates (one dimension is much smaller than the wavelength) resulting in the effective propagation of extensional and flexural waves. However, a disadvantage of ceramic composites is that as the material damages the modulus decreases and consequently the speed of sound decreases and the attenuation of higher frequency waves most likely increases. Therefore, identifying the source of the event may not be straightforward; however, certain source events can be inferred indirectly.

In this study, some progress has been made towards using AE data to quantify matrix cracking using the relation between the energy of the AE data with the number or density of transverse matrix cracks. It was inferred in reference 1 that higher energy events correspond to matrix cracks because they occurred early in the stress strain curve just before and just after the "knee" in the curve (Figure A1). The highest energy events were essentially absent when the tangent modulus of the stress-strain curve increased ($\epsilon > \sim 0.3\%$) which signifies the saturation of matrix cracks (see section 1.2.1). Two sets of data from this study confirm this relationship: (1) the comparison of matrix cracking and applied stress for room or low temperature tests and (2) the comparison of cracking along the length of a test specimen with cumulated AE energy at elevated temperatures.

^{*} For simpler systems where fewer events are occurring this is not a problem. For example in the microcomposite work, using traditional AE, we were able to observe the cracks, since there were so few, either during the experiment or after to confirm what noise corresponded to a matrix crack[3,6].

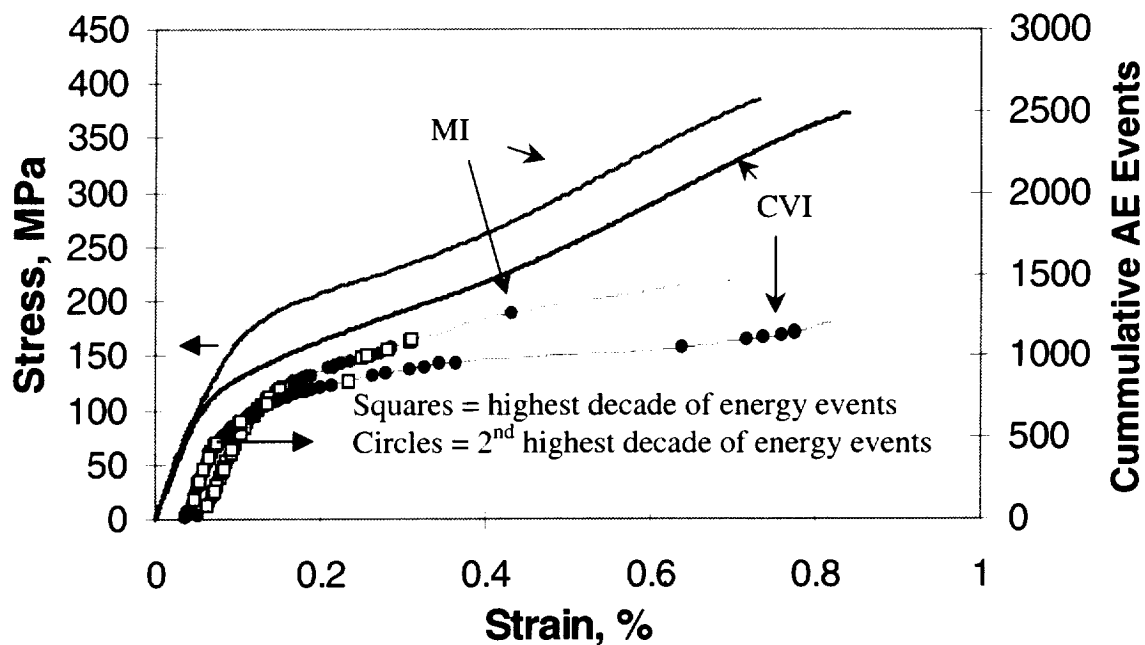


Figure A1: Tensile stress-strain and AE activity for Hi-Nicalon, MI and CVI matrix composites from references 1 and 7.

A.1 Matrix Cracking at Room (low) Temperatures

For the samples tested in this study, the matrix crack density was determined along the length of the sample (section 3.2). The part of the sample that was far from the hot zone is exposed to temperatures below 500°C. Since these samples were taken to a relatively low stress, compared to the ultimate stress of the composites, the crack spacing in the cold section should correspond to that applied stress. This can then be related to the AE activity as a function of the stress strain curve.

Figure A2 shows a comparison of the normalized cumulative AE energy* for two HN-MI composites and the normalized crack densities of the HN-MI composite used in the rupture experiments. The composite with AE activity occurring at the lower strain corresponds to the same material used for rupture in this study, except tested at room temperature to failure. Note that this sample underwent unload-reload tensile testing to failure that accounts for the low strain, high cumulative AE energy data. Also shown in Figure A2 is the AE activity for a “higher cracking strain composite” that was tested in reference 7. The room temperature stress strain curve for this composite system is shown in Figure A3 with the material tested in rupture in this study and the material used by Brewer et al [8]. The “knee” in the stress-strain curve, though not as high in stress as Brewer et al. [8], is measurably higher than the material used for rupture in this study. AE activity occurs very similarly for the two samples except the sample which has the lower cracking stress (and strain) also has more AE activity occurring at lower strains up to about 0.35%.

*Normalized cumulative AE energy is used because the absolute cumulative AE energy can vary by greater than a factor of two depending on the preamplification settings of the AE detector and how well the transducers contact the specimen surface. It is assumed that whatever causes the loudest acoustic waveforms in similar composites was comparable from specimen to specimen.

The normalized crack densities are also plotted for the “low strain cracking” composite and are in good agreement with the measured AE activity. However, the AE energy data overestimates the amount of cracking in the 0° bundles (crack density) for these composites.

For single fiber microcomposites and single tow minicomposites, using traditional AE, a direct relationship was found between AE energy and matrix cracking [6]. For these composites, all the transverse matrix cracks are bridged by load-bearing fibers. For the macrocomposites, the first cracks occur in the 90° bundles and large matrix regions (tunnel cracks) and are not bridged, at least initially, by the 0° bundles (Section 1.2.2). The reason for the greater amount of AE energy compared to the amount of matrix cracking probably has to do with the formation of these tunnel cracks since only 0° cracks were measured for the crack density determination.

It should be noted that there are some situations in which traditional AE monitoring can enable quantitative damage accumulation measurement. However, the reason for this was probably due to the specimen mounting. The ends of the microcomposites and minicomposites were tabbed in epoxy and the specimen epoxy tab was gripped in order to perform the tensile test. The sensors were mounted on the epoxy; therefore, sound had to travel along the minicomposite and through the epoxy in order to be detected by the transducer. Fortunately, the sound of SiC matrix failures was significantly louder and higher in frequency than grip noise. Therefore, the grip noise could easily be filtered out. The length of minicomposite between the two tabs was the effective gage length of the tested specimen so that all the sound of the specimen could be used for analysis, i.e. the location of the sound was not important because the entire length of minicomposite was the gage section.

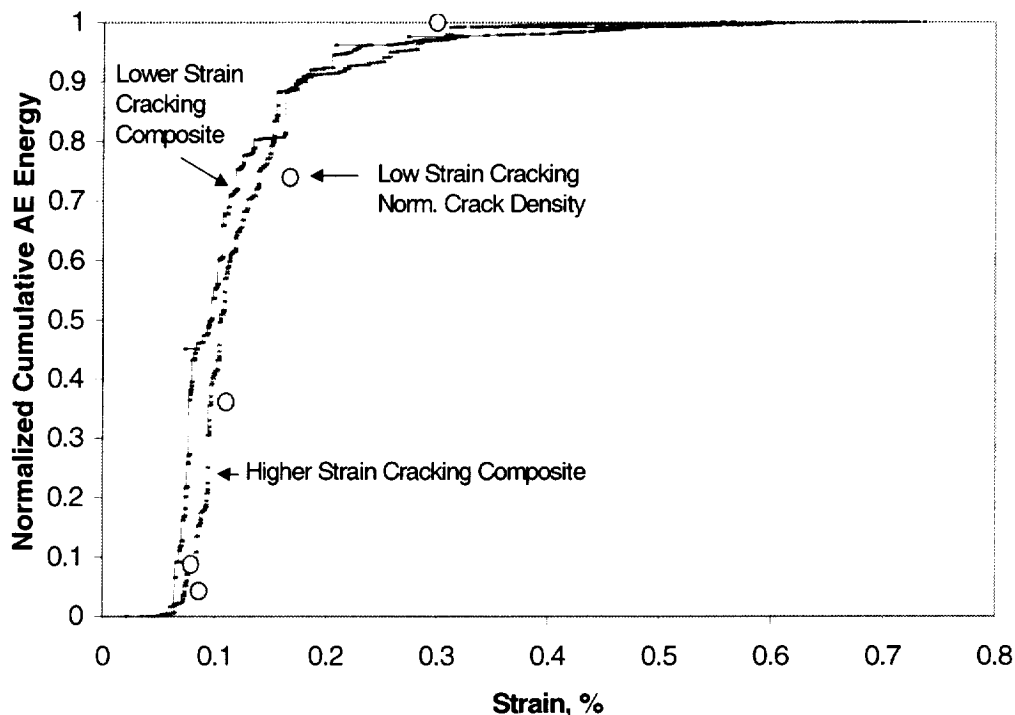


Figure A2: Comparison of cumulative AE energy from room temperature experiments and the linear crack density versus strain from crack-spacings measured in the cold section of ruptured samples.

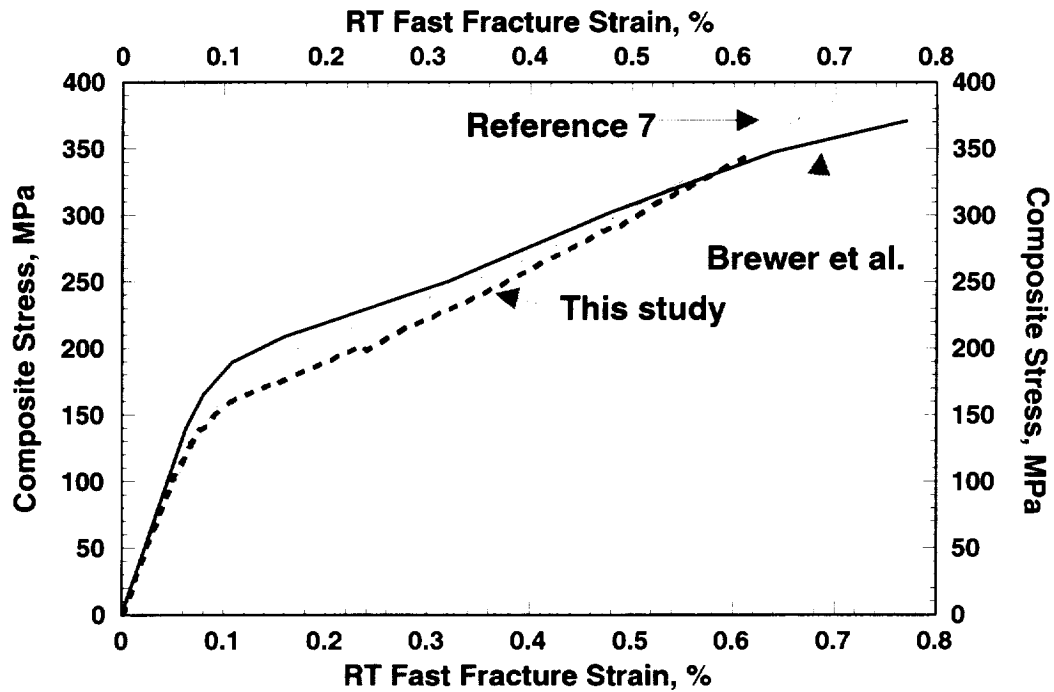


Figure A3: Stress-strain curves of different HN-BN-MI SiC composites.

For the case where the sensors are attached to the tensile specimen surface (Figure A4), the location of the sound is very important because cracking occurs in between and outside of the two sensors but not in the gage section. For example, the absolute cumulative energies of all the events and the gage-separated events are plotted for the MI-matrix composite tested in this study (Figure A5). The absolute energy for all the events is 3.4 times greater than the gage-separated events for the low-strain cracking composite. This correlates well with the length of composite. The length of composite in between the grips is about 3 times the length of the gage section. For dogbone specimens, cracking would also occur over a wider load range along the length of the dogbone specimen due to the changing cross-sectional area.

The normalized AE energy curve for both the entire AE data set and the gage-separated data set is the same at lower strains. However, the two data sets diverge with increasing strain. It is apparent that more AE activity occurs outside the gage during unloading and reloading than in the gage section. The crack density relates better to the gage-separated AE energy than the entire AE event data set.

For both of the macrocomposites discussed in this section tested at room temperature, $92.5 \pm 0.5\%$ of the cumulative energy pertain to events with the two highest decades of energy. Comparable percentages are found for Hi-Nicalon-CVI SiC matrix composites and Sylramic-MI SiC matrix composites [9].

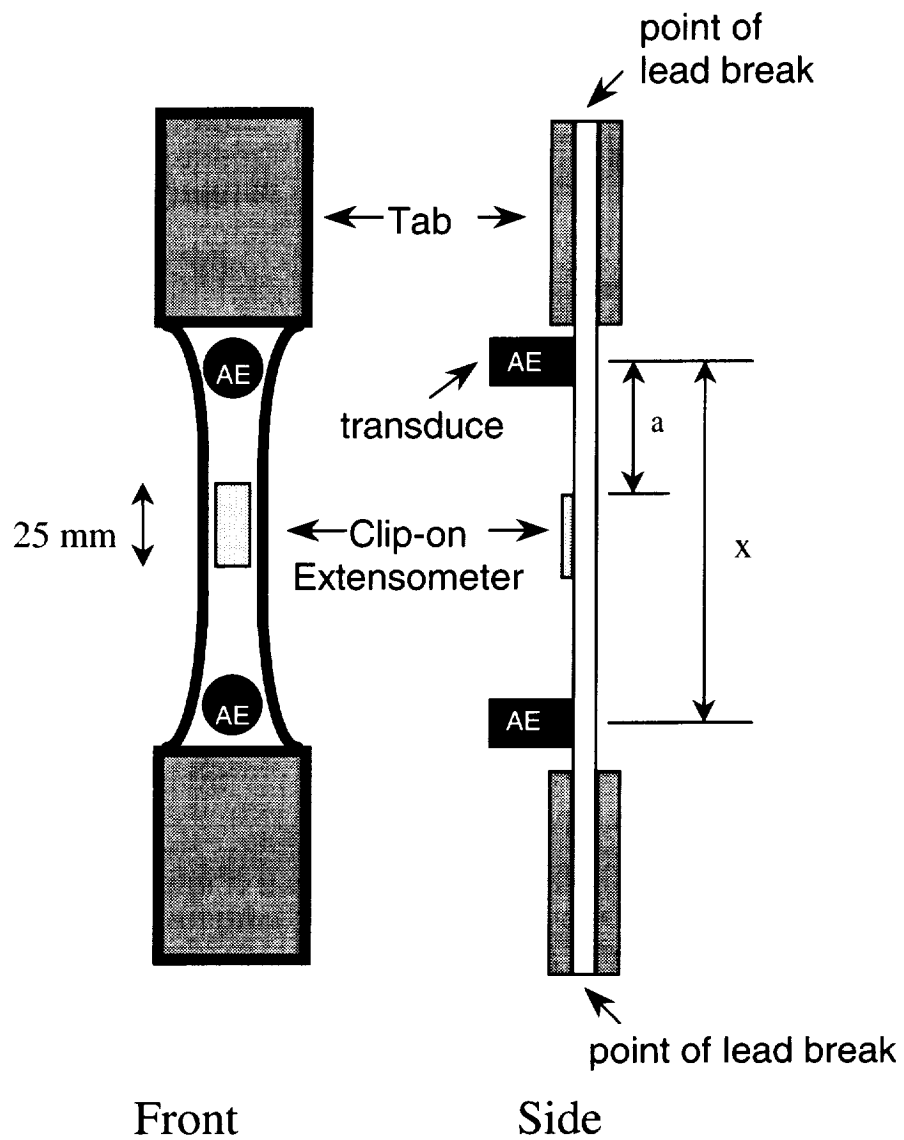


Figure A4: Typical AE sensor placement for room temperature tensile specimen. The specimen tested at room temperature from the same panel as the stress-rupture specimens was not a dogbone.

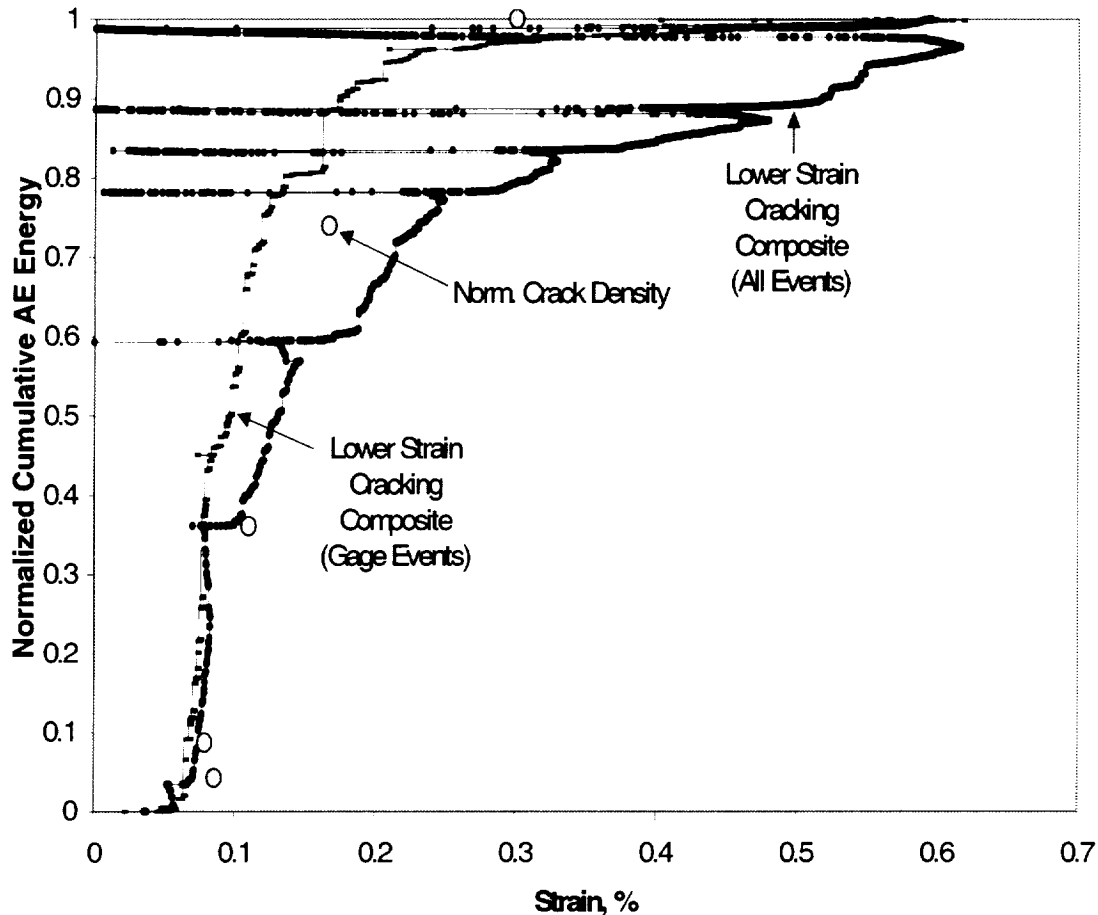


Figure A5: Comparison between the gage-separated and total number of AE events recorded during the unload-reload hysteresis tensile test for the “low strain cracking” composite. The normalized crack density is also plotted from the measured crack densities of the cold sections of rupture specimens.

A.2 Matrix Cracking at Elevated Temperatures

For the stress-rupture tests, the sensor placement for these experiments is “edge-on” whereas the sensor-placement for the room-temperature tests is on the “face” of the test specimen. The “edge-on” sensor-placement cannot detect the flexural portion of the acoustic waveform. Even so, the AE energy analysis showed similar results to the room temperature results. Figure A6 shows the AE energy and crack density over the length of the samples that were ruptured at 4.4 kN (960°C) and 4 kN (815°C). To get this data, the number of cracks was measured over approximately 10 mm length-intervals and the cumulative AE energy was determined over 5 mm length-intervals of the composite specimen. There is excellent correlation between the crack density and the cumulative energy. For these high temperature tests, 85 and 89% of the cumulative AE energy were from the two highest decades of energy events for the 4.4 kN and 4 kN rupture tests, respectively. The slightly smaller percentage of cumulative AE energy corresponding to the loudest events for the elevated temperature tests compared to the room temperature tests (92%) may be a consequence of the sensor-placement.

Therefore, it can be concluded that the use of AE energy coupled with the location accuracy of modal AE is a reliable method to monitor matrix cracking in CMC's at both room and elevated temperatures.

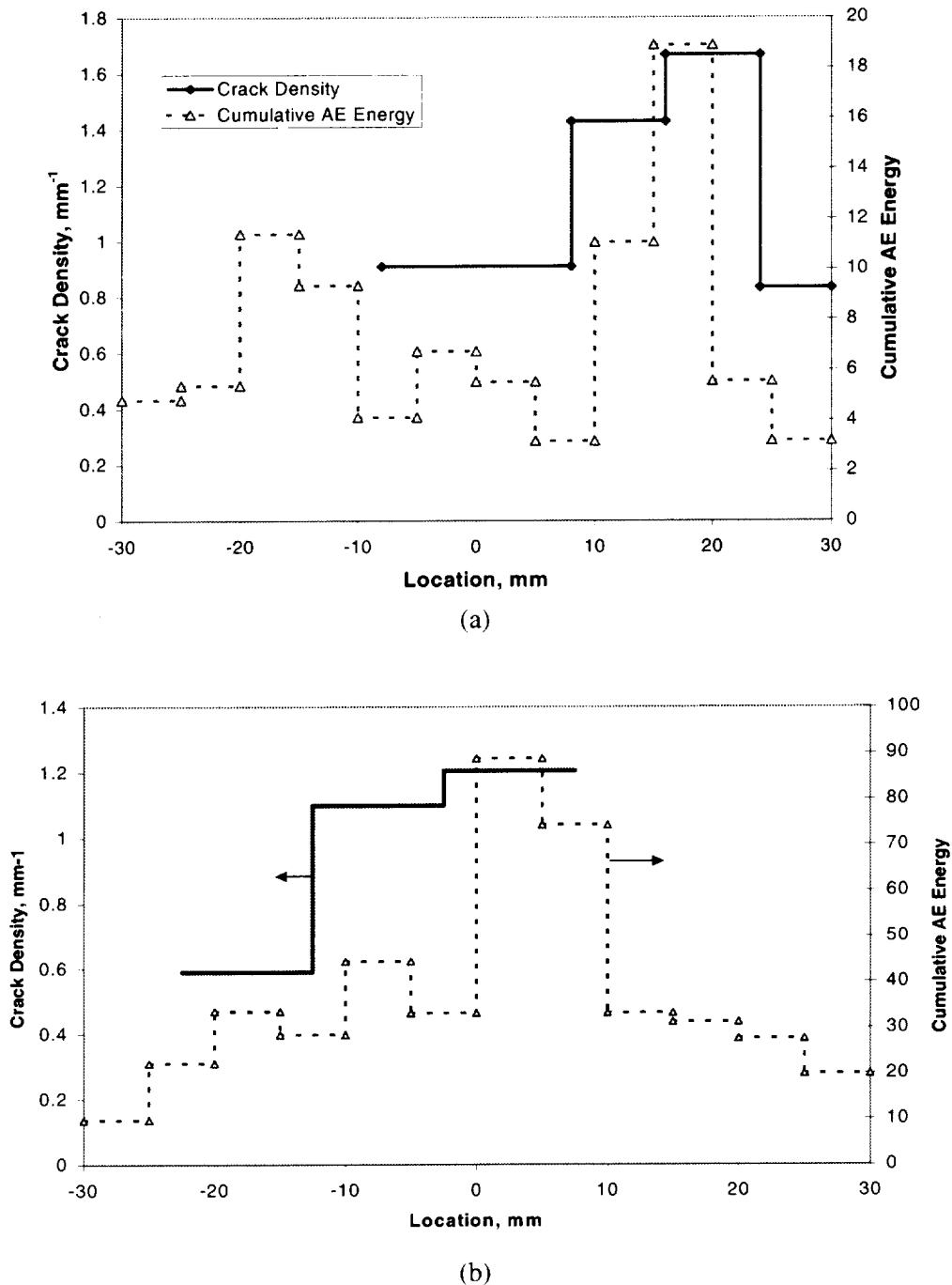


Figure A6: Comparison of cumulative AE energy and crack spacing for sample ruptured at (a) 4.4 kN and 960°C and (b) 4 kN and 815°C.

A.3 Works Cited

1. G.N. Morscher, "Modal Acoustic Emission of Damage Accumulation in a Woven SiC/SiC Composite," *Comp. Sci. Tech.* In press.
2. A. Chulya and J.P. Gyekenyesi, "In-situ NDE Monitoring of Crack Bridging in Ceramic Composites via Crack Opening Displacement," Presented at International Gas Turbine and Aeroengine Congress, The Hague, Netherlands; June 13-16, 1994. ASME publication 94-GT-444.
3. G.N. Morscher and J. Martinez-Fernandez, "Determination of Interfacial Properties Using a Single-Fiber Microcomposite Test," *J. Am. Ceram. Soc.*, **79** [4] 1083-91 (1996).
4. M. Surgeon, E. Vanswijgenhoven, M. Wevers, and O. Van Der Biest, "Acoustic Emission During Tensile Testing of SiC-Fibre-Reinforced BMAS Glass-Ceramic Composites," *Composites Part A*, **28A**, pp. 473-480 (1997).
5. N. Lissart and J. Lamon, "Damage and Failure in Ceramic Matrix Minicomposites: Experimental Study and Model," *Acta mater.* **45** [3] 1025-44 (1997).
6. G.N. Morscher and J. Martinez-Fernandez, "Fiber Effects on Minicomposite Properties for Several Silicon Carbide Fiber – Chemically Vapor-Infiltrated Silicon Carbide Matrix Systems," *J. Am. Ceram. Soc.* *J. Am. Ceram. Soc.*, **82** [1] 145-55 (1999).
7. D. Brewer, A. Calomino, and M. Verilli, unpublished research.
8. G.N. Morscher and J.Z. Gyekenyesi, "Room Temperature Tensile Behavior and Damage Accumulation of Hi-Nicalon Reinforced SiC Matrix Composites," *Ceram. Eng. Sci. Proc.*, **19** [3] 241-249 (1998).
9. G.N. Morscher, "Modal Acoustic Emission Source Determination in Silicon Carbide Matrix Composites," Review of Quantitative Nondestructive Evaluation, Vol. 19, eds. D.O. Thompson and D.E. Chimenti, (2000) in print.

APPENDIX B: THE LIKELIHOOD FOR FIBER RUPTURE AWAY FROM A MATRIX CRACK

Since the stress on the fiber is lower away from a matrix crack (Figure B1), and the stress rupture exponent, n , is very large the likelihood for fiber failure away from the matrix crack may not be so great. Based on traditional slow-crack growth theory [1], the flaw size required to fail a fiber under the reduced stress condition away from the matrix crack can be estimated. For constant stress conditions, the equation used to estimate the time to failure is

$$t_f = 2 / (\sigma^2 Y^2 A (n-2) K_{II}^{n-2}) \quad \text{B.1}$$

where Y and A are constants. K_{II} is the initial stress intensity at the start of the test:

$$K_{II} = \sigma (c)^{1/2} \quad \text{B.2}$$

where c is the initial flaw size. Therefore, the time to failure for rupture can be represented by:

$$t_f = k / (\sigma^n c^{n-2}) \quad \text{B.3}$$

where k is a constant. The time it takes a fiber loaded at a lower stress (assuming the same gage length) can be estimated by:

$$\underline{t} = t/t_f = (\sigma_f/\sigma)^n \quad \text{B.4}$$

where t_f is the time to failure for a fully loaded fiber, σ_f , and \underline{t} is the normalized time to failure for a different applied stress. The initial flaw size required to fail a fiber at a given stress in the same amount of time that it takes a fully loaded fiber to fail can be estimated by

$$\underline{c} = c/c_f = (\sigma_f/\sigma)^{2n/n-2} \quad \text{B.5}$$

where c_f is the initial crack size for a fully loaded fiber and \underline{c} is the normalized initial flaw size. Estimates of \underline{t} and \underline{c} are listed in Table B1.

At first glance, it appears improbable for a fiber to fail very far away from the matrix crack opening. However, this analysis assumes the same gage length for all the stress-conditions. In reality the sliding length is several orders of magnitude larger than the crack opening displacement. In order to account for this, the probability for failure in the sliding region and in the crack opening region can be estimated based on equations 4.1 and 4.2 where σ_o is determined from equation 4.3 (assumed to be 1 hour for comparison). The gage length for sliding was estimated from equation 4.6 multiplied by two and the stress in the sliding region was taken as the average stress over the whole sliding length (half the sum of the rule of mixtures stress and fully loaded stress on the fibers, see Figure B1). Table B2 lists the estimated probabilities and parameters used. From this analysis, it is about two times more likely that a fiber would fail in the sliding region rather than the matrix crack opening.

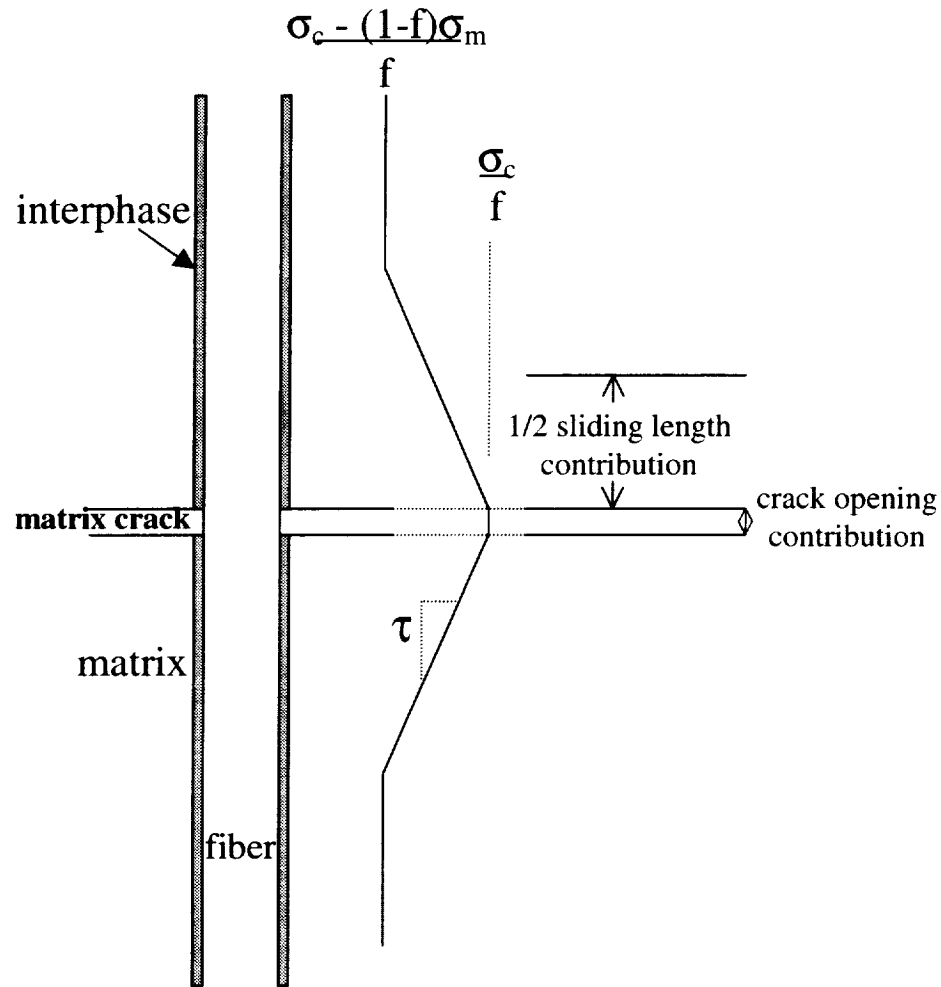


Figure B1: Schematic representation of stress-profile along the length of a fiber near and at a matrix crack (assuming the debond energy is zero).

Table B1: Estimated time to failure and flaw size for lower stresses away from matrix crack.

σ / σ_r	n	t	c
0.9	30	23.6	1.25
0.8	30	807.8	1.61
0.7	30	44370	2.15
0.6	30	4523400	2.99
0.5	30	1.07E+09	4.42

Table B2: Failure probabilities for fibers in the matrix crack and in the sliding region.

$\sigma_{\text{composite}}$ MPa	σ_f MPa	Rule of Mixtures Fiber Stress MPa	Sliding Length mm	Crack Opening μm	Probability for Failure in Matrix Crack	Probability for Failure in Sliding Region
163	959	282	0.1732	1.22	4.6E-06	1.0E-05
148	871	256	0.1573	1.05	2.9E-06	6.6E-06
140	826	243	0.1491	0.97	2.4E-06	5.7E-06

B.1 Work Cited

1. A.G. Evans, L.R. Russel, and D.W. Richerson, "Slow Crack Growth in Ceramic Materials at Elevated Temperatures," met. Trans. 6A [4] 707-716 (1975).

BIBLIOGRAPHY

Aveston, J.; Cooper, G.A.; Kelly, A.; "Single and Multiple Fracture," The Properties of Fibre Composites; IPC Science and Technology Press, Ltd, p. 15-24 (1971).

Bansal, N.P.; Doremus, R.H.; Handbook of Glass Properties, Academic Press, Inc., 1986, p. 244.

Bodet, R.; Bourat, X.; Lamon, J.; Naslain, R.; "Tensile Creep Behavior of a Silicon Carbide-Based Fibre with a Low Oxygen Content," *J. Mater. Sci.*, **30** 661-77 (1995).

Brennan, J.J.; Prewo, K.M.; "Silicon Carbide Fiber Reinforced Glass-Ceramic Matrix Composites Exhibiting High Strength and Toughness," *J. Mater. Sci.*, **17** [8] 2371-83 (1982).

Brennan, J.J.; private communication; Sun, E.Y.; Nutt, S.R.; Brennan, J.J.; "Interfacial Microstructure and Chemistry of SiC/BN Dual-Coated Nicalon-Fiber-Reinforced Glass-Ceramic Matrix Composites," *J. Am. Ceram. Soc.*, **77** [5] 1329-39 (1994).

Brewer, D.; Calomino, A.; Verilli, M.; Unpublished data from the Enabling Propulsion Materials Program at NASA Glenn Research Center.

Budiansky, B.; Hutchinson, J.W.; Evans, A.G.; "Matrix Fracture in Fiber-Reinforced Ceramics," *J. Mech. Phys. Solids* **34**, 167-189 (1986).

Buttle, D.J.; Seruby, C.B.; "Acoustic Emission Source Location in Fiber Reinforced Plastic Composites," *J. Acoustic Emission*, **7** [4] 211-223 (1988).

Cawley, J.D.; "Effect of Interphase Carbon Thickness on Environmental Resistance of Continuous Fiber-Reinforced Ceramic Matrix Composites," pp. 377-84 in Ceramic Transactions, Vol. 58, *High-Temperature Ceramic-Matrix Composites II*, Edited by A.G. Evans and R. Naslain. American Ceramic Society, Westerville, OH (1995).

Choi, S.R.; Salem, J.A.; Nemeth, N.N.; "High-Temperature Slow Crack Growth of Silicon Carbide Determined by Constant-Stress-Rate and Constant-Stress Testing," *J. Mater. Sci.*, **33**, pp. 1325-1332 (1998).

Chollon, G.; Paillet, R.; Naslain, R.; Laanani, F.; Monthieux, M.; Olry, P.; "Thermal Stability of a PCS-derived SiC fibre with a Low Oxygen Content (Hi-Nicalon)," *J. Mater. Sci.*, **32** 327-347 (1997).

Chulya, A.; Gyekenyesi, J.P.; "In-situ NDE Monitoring of Crack Bridging in Ceramic Composites via Crack Opening Displacement," Presented at International Gas Turbine and Aeroengine Congress, The Hague, Netherlands; June 13-16, 1994. ASME publication 94-GT-444.

- Cofer, C.G.; Economy, J.; "Oxidative and Hydrolytic Stability of Boron Nitride – A New Approach to Improving the Oxidation Resistance of Carbonaceous Structures," *Carbon*, **33** [4] 389-95 (1995).
- Cox, B.N.; Marshall, D.B.; "Crack Initiation in Fiber-Reinforced Brittle Laminates," *J. Am. Ceram. Soc.*, **79** [5] 1181-88 (1996).
- Curtin, W.A.; "Multiple Matrix Crack Spacing in Brittle Matrix Composites," *Acta. Metall. Mater.* **41** [5] 1369-1377 (1993).
- DiCarlo, J. A.; "Creep Limitations of Current Polycrystalline Ceramic Fibers," *Comp. Sci. Tech.* **51** 213-222 (1994).
- Domergue, J.M.; Heredia, F.E.; Evans, A.G.; "Hysteresis Loops and the Inelastic Deformation of 0/90 Ceramic Matrix Composites," *J. Am. Ceram. Soc.*, **79** [1] 161-70 (1996).
- Domergue, J-M.; Vagaggini, E.; Evans, A.G.; "Relationships between Hysteresis Measurements and the Constituent Properties of Ceramic Matrix Composites: II, Experimental Studies on Unidirectional Materials," *J. Am. Ceram. Soc.*, **78** [10] 2721-31 (1995).
- Easler, T.E.; Bradt, R.C.; Tressler, R.E.; "Strength Distributions of SiC Ceramics After Oxidation and Oxidation Under Load," *J. Am. Ceram. Soc.*, **64** [12] 731-34 (1981).
- Eckel, A.J.; Bradt, R.C.; "Strength Distribution of Reinforcing Fibers in a Nicalon Fiber/Chemically Vapor Infiltrated Silicon Carbide Matrix Composite," *J. Am. Ceram. Soc.*, **72** [3] 455-58 (1989).
- Eckel, A.J.; Cawley, J.D.; Parthasarthy, T.A.; "Oxidation Kinetics of a Continuous Carbon Phase in a Nonreactive Matrix," *J. Am. Ceram. Soc.*, **78** [4] 972-80 (1995).
- Evans, A.G.; Russel, L.R.; Richerson, D.W.; "Slow Crack Growth in Ceramic Materials at Elevated Temperatures," *met. Trans.* **6A** [4] 707-716 (1975).
- Evans, A.G.; Zok, F.W.; McMeeking, R.M.; Du, Z.Z.; "Models of High-Temperature, Environmentally Assisted Embrittlement in Ceramic-Matrix Composites," *J. Am. Ceram. Soc.*, **79** [9] 2345-52 (1996).
- Favre, J.P.; Laizet, J.C.; "Amplitude and Counts per Event Analysis of the Acoustic Emission Generated by the Transverse Cracking of Cross-ply CFRP," *Comp. Sci. Tech.*, **36** pp. 27-43 (1989).
- Filipuzzi, L.; Camus, G.; Naslain, R.; Thebault, J.; "Oxidation Mechanisms and Kinetics of 1D-SiC/C/SiC Composite Materials: I, An Experimental Approach," *J. Am. Ceram. Soc.*, **77** [2] 459-466 (1994).
- Glime, W.H.; Cawley, J.D.; "Stress Concentration Due to Fiber-Matrix Fusion in Ceramic Matrix Composites," *J. Am. Ceram. Soc.* **81** [10] 2597-604 (1998).

Gorman, M.R.; "New Technology for Wave Based Acoustic Emission and Acousto-Ultrasonics," AMD-Vol. 188, Wave Propagation and Emerging Technologies, ASME, pp. 47-59 (1994).

Gorman, M.R.; "Plate Wave Acoustic Emission," *J. Acoust. Soc. Am.*, **90** [1] 358-364.

Gorman, M.R.; Prosser, W.H.; "AE Source Orientation by Plate Wave Analysis," *J. Acoustic Emission*, **9**[4] 283-288 (1991).

Gu, X.; Butler, E.G.; "Alumina Woven Fibre-Reinforced Composites Produced by Directed Melt Oxidation," *Ceram. Eng. Sci. Proc.*, **18** [3] 371-378 (1997).

Guillaumat, L.; Lamon, J.; "Multi-fissuration de Composites SiC/SiC," in Revue des Composites et des Materiaux Avances, vol. 3, pp. 159-171 (1993).

Guillaumat, L.; Lamon, J.; "Probabilistic-Statistical Simulation of the Non-Linear Mechanical Behavior of a Woven SiC/SiC Composite," *Comp. Sci. Tech.*, **56** pp. 803-808 (1996).

Halada, J.; Allied Signal Corporation, private communication.

Halverson, H.; Curtin, W.; unpublished research.

Henager Jr., C.H.; Jones, R.H.; "Subcritical Crack Growth in CVI Silicon Carbide Reinforced with Nicalon Fibers: Experiment and Model," *J. Am. Ceram. Soc.*, **77** [9] 2381-94 (1994).

Heredia, F.E.; McNulty, J.C.; Zok, F.W.; Evans, A.G.; "Oxidation Embrittlement Probe for Ceramic-Matrix Composites," *J. Am. Ceram. Soc.*, **78** [8] 2097-100 (1995).

Hutchinson, J.W.; Jensen, H.M.; "Models for Fiber Debonding and Pullout in Brittle Composites with Friction," *Mech. Mater.*, **9**, 139-63 (1990).

Ibnabdeljalil, M.; Curtin, W.A.; "Strength and Reliability of fiber-Reinforced Composites: Localized Load-Sharing and Associated Size Effects," *Int. J. Solids Structures*, **34** [21] 2649-2668 (1997).

Jacobson, N.S.; Farmer, S.; Moore, A.; Sayir, H.; "High Temperature Oxidation Behavior of Boron Nitride Part I: Monolithic BN," *J. Am. Ceram. Soc.*, **82** [2] 393-8 (1999).

Jacobson, N.S.; Morscher, G.N.; Bryant, D.R.; Tressler, R.E.; "High Temperature Oxidation of Boron Nitride Part II: BN Layers in Composites," *J. Am. Ceram. Soc.* **82** [6] 1473-82 (1999).

Jamet, J.F.; Lewis, D.; Luh, E.Y.; "Characterization of Mechanical Behavior and Fractographic Observations on Compglas SiC/LAS Composites," *Ceram. Eng. Sci. Proc.*, **5** [7-8] 625-42 (1984).

Johnson, A.M.; Batlett, B.J.; Troha, W.A.; "Material Changes and Progress Toward Meeting the High Speed Civil Transport Propulsion Design Requirements," ISABE 97-7179, American Institute of Aeronautics and Astronautics, pp. 1321-1328 (1997).

Kawamoto, K.; Ono, K.; "Pattern Recognition Analysis of Acoustic Emission Signals from Carbon Fiber/Epoxy Composites," AECM-3 Third International Symposium On Acoustic Emission from Composite Materials, Paris France, July 17-21, 1989. Published by American Society for Nondestructive Testing, Inc., Columbus, OH, pp. 230-239 (1989).

Kimber, A.C.; Keer, J.G.; "On the Theoretical Average Crack Spacing in Brittle Matrix Composites Containing Continuous Aligned Fibers," *J. Mater. Sci. Letters* **1** 353-354 (1982).

Lamon, J.; Rebillat, F.; Evans, A.G.; "Microcomposite Test Procedure for Evaluating the Interface Properties of Ceramic Matrix Composites," *J. Am. Ceram. Soc.*, **78** [2] 401-405 (1995).

Lara-Curzio, E.; "Stress-Rupture of Nicalon/SiC Continuous Fiber Ceramic Matrix Composites in Air at 950°C," *J. Am. Ceram. Soc.*, **80** [12] 3268-72 (1997).

Lara-Curzio, E.; Ferber, M.K.; Tortorelli, P.F.; "Interface Oxidation and Stress-Rupture of NicalonTM/SiC CVCCs at Intermediate Temperatures," Key Engineering Materials Vols. 127-131, Trans Tech Publications, Switzerland, pp. 1069-1082 (1997).

Lara-Curzio, E.; Ross, C.; "Why is it Necessary to Measure Each Fiber Diameter When Determining the Distribution of Strengths of Ceramic Fibers," *Ceram. Eng. Sci. Proc.*, (1999) in print.

Le Coustumer, P.; Monthieux, M.; Oberlin, A.; "Understanding Nicalon Fibre," *J. European Ceram. Soc.*, **11** 95-103 (1993).

Levi, C.G.; Yang, J.Y.; Dalgeish, B.J.; Zok, F.W.; Evans, A.G.; "Processing and Performance of an All-Oxide Ceramic Composite," *J. Am. Ceram. Soc.*, **81** [8] 2077-86 (1998).

Lin, H.T.; Becher, P.F.; "Effect of Coating on Lifetime of Nicalon Fiber-Silicon Carbide Composites in Air," *Mater. Sci. Eng.* A231 143-150 (1997).

Lin, H.T.; Becher, P.F.; "Stress-Temperature-Lifetime Response of Nicalon Fiber-Reinforced SiC Composites in Air," pp. 128-41 in *ASTM Symposium of Thermal and Mechanical Test Methods and Behavior of Continuous-Fiber Ceramic Composites*, ASTM STP 1309, Eds. M.G. Jenkins, S.T. Gonczy, E. Lara-Curzio, N.E. Ashbaugh, and L.P. Zawada (1997).

Lipetzky, P.; Stoloff, N.S.; Dvorak, G.J.; "Atmospheric Effects on High-Temperature Lifetime of Ceramic Composites," *Ceram. Eng. Sci. Proc.*, **18** [4] 355-362 (1997).

Lipowitz, J.; Rabe, J.A.; Zangvil, A.; Xu, Y.; "Structure and Properties of Sylramic Silicon Carbide Fiber – A Polycrystalline, Stoichiometric β -SiC Composition," *Ceram. Eng. Sci. Proc.*, **18** [3] 147-157 (1997).

Lissart, N.; Lamon, J.; "Damage and Failure in Ceramic Matrix Minicomposites: Experimental Study and Model," *Acta Mater.* **45** [3] 1025-1044 (1997).

Marshall, D.B.; Cox, B.N.; Evans, A.G.; "The Mechanics of Matrix Cracking in Brittle Matrix Fiber Composites," *Acta Metall.*, **33** [11] 2013-21 (1985).

Marshall, D.B.; Evans, A.G.; "Failure Mechanisms in Ceramic-Fiber/Ceramic-Matrix Composites," *J. Am. Ceram. Soc.*, **68** [5] 225-31 (1985).

Martinez-Fernandez, J.; Morscher, G.N.; "Stress Rupture of Hi-Nicalon, Carbon Interphase, CVI SiC Matrix Minicomposites in Air," unpublished results.

Moore, A.W.; Strong, S.L.; "Variations in the Structure and Morphology of Pyrolytic Boron Nitride," *Ceram. Eng. Sci. Proc.*, **10** [7-8] 846-856 (1989).

Morscher, G.N.; "Modal Acoustic Emission of Damage Accumulation in a Woven SiC/SiC Composite," *Comp. Sci. Tech.* **59** 687-697 (1999).

Morscher, G.N.; "Modal Acoustic Emission Source Determination in Silicon Carbide Matrix Composites," Review of Quantitative Nondestructive Evaluation, Vol. 19, eds. D.O. Thompson and D.E. Chimenti, (2000) in print.

Morscher, G.N.; "Tensile Stress Rupture of SiC_f/SiC_m Minicomposites with Carbon and Boron Nitride Interphases at Elevated Temperatures in Air," *J. Am. Ceram. Soc.*, **80** [8] 2029-42 (1997).

Morscher, G.N.; "The Effect of Static and Cyclic Tensile Stress and Temperature on Failure for Precracked Hi-Nicalon/BN/CVD SiC Minicomposites in Air," *Ceram. Eng. Sci. Proc.*, (1997).

Morscher, G.N.; Bryant, D.; Tressler, R.E.; "Environmental Durability of Different BN Interphases (for SiC/SiC) in H₂O Containing Atmospheres at Intermediate Temperatures," *Ceram. Eng. Sci. Proc.*, **18** [3] 525-534 (1997).

Morscher, G.N.; Gyekenyesi, J.Z.; Bhatt, R.T.; "Damage Accumulation in Woven SiC/SiC Composites," submitted to *Environmental, Mechanical, and Thermal Properties and Performance of Continuous Fiber Ceramic Composite (CFCC) Materials and Components, ASTM STP 1392*.

Morscher, G.N.; Martinez-Fernandez, J.; "Determination of Interfacial Properties Using a Single-Fiber Microcomposite Test," *J. Am. Ceram. Soc.*, **79** [4] 1083-91 (1996).

Morscher, G.N.; Martinez-Fernandez, J.; "The Interfacial and Ultimate Strength Properties for Several Single Tow SiC-Fiber, CVI SiC Matrix Minicomposites at Room Temperature," *J. Am. Ceram. Soc.* **82** [1] 145-55 (1999).

Morscher, G.N.; Gyekenyesi, J.Z.; "Room Temperature Tensile Behavior and Damage accumulation of Hi-Nicalon Reinforced SiC Matrix Composites," *Ceram. Eng. Sci. Proc.*, **19** [3] 241-249 (1998).

Pluinage, P.; Parvizi-Majidi, A.; Chou, T.W.; "Damage Characterization of Two-Dimensional woven and Three-Dimensional Braided SiC-SiC Composites," *J. Mater. Sci.*, **31** 232-241 (1996).

Prewo, K.M.; Brennan, J.J.; "High Strength Silicon Carbide Fiber Reinforced Glass Matrix Composites," *J. Mater. Sci.*, **15** [2] 463-68.

Prewo, K.M.; Brennan, J.J.; "Silicon Carbide Yarn Reinforced Glass Matrix Composites," *J. Mater. Sci.*, **17** [4] 1201-1206 (1982).

Prosser, W.H.; Jackson, K.E.; Kellas, S.; Smith, B.T.; McKeon, J.; Friedman, A.; "Advanced, Waveform Based Acoustic Emission Detection of Matrix Cracking in Composites," *Mater. Evaluation* **53** [9] 1052-8 (1995).

Sawyer, L.C.; Chen, R.T.; Haimbach IV, F.; Harget, P.J.; Prack, E.R.; Jaffe, M.; "Thermal Stability Characterization of SiC Ceramic Fibers: II, Fractography and Structure," *Ceram. Eng. Sci. Proc.*, **7** [7-8] 914-30 (1986).

Shimoo, T.; Hayatsu, T.; Takeda, M.; Ichikawa, H.; Seguchi, T.; Okamura, K.; "Mechanism of Oxidation of Low-Oxygen SiC Fiber Prepared by Electron Radiation Curing Method," *J. Ceram. Soc. Japan (Int. Edition)*, **102** [7] 618-622 (1994).

Spearing, S.M.; Zok, F.W.; Evans, A.G.; "Stress Corrosion Cracking in a Unidirectional Ceramic-Matrix Composite," *J. Am. Ceram. Soc.*, **77** [2] 562-70 (1994).

Steyer, T.E.; Zok, F.W.; Walls, D.P.; "Stress Rupture of an Enhanced NicalonTM/SiC Composite at Intermediate Temperatures," *J. Am. Ceram. Soc.* **81** [8] 2140-46 (1998).

Sun, E.Y.; Lin, H.T.; Brennan, J.J.; "Intermediate-Temperature Environmental Effects on Boron Nitride-Coated Silicon Carbide-Fiber-Reinforced Glass-Ceramic Composites," *J. Am. Ceram. Soc.*, **80** [3] 609-14 (1997).

Surgeon, M.; Vanswijgenhoven, E.; Wevers, M.; Van Der Biest, O.; "Acoustic Emission During Tensile Testing of SiC-Fibre-Reinforced BMAS Glass-Ceramic Composites," *Composites Part A*, **28A**, pp. 473-480 (1997).

Takeda, M.; Imai, Y.; Ichikawa, H.; Ishikawa, T.; Kasai, N.; Seguchi, T.; Okamura, K.; "Thermomechanical Analysis of the Low Oxygen Silicon Carbide Fibers Derived from Polycarbosilane," *Ceram. Eng. Sci. Proc.*, **14** [7-8] 540-547 (1993).

Thomas-Ogbuji, L.; "A Pervasive Mode of Oxidative Degradation in a SiC-SiC Composite," *J. Am. Ceram. Soc.*, **8** [11] 2777-84 (1998).

Vagaggini, E.; Domergue, J-M.; Evans, A.G.; "Relationships between Hysteresis Measurements and the Constituent Properties of Ceramic Matrix Composites: I, Theory," *J. Am. Ceram. Soc.*, **78** [10] 2709-20 (1995).

Valentin, D.; Bonniau, P.; Bunsell, A.R.; "Failure Mechanism Discrimination in Carbon Fibre-Reinforced Epoxy Composites," *Composites*, **14** [4] 345-351 (1983).

Verilli, M.J.; Calomino, A.M.; Brewer, D.N.; "Creep-rupture Behavior of a Nicalon/SiC Composite," Thermal and Mechanical Test Methods and Behavior of Continuous-Fiber Ceramic Composites, ASTM STP 1309, eds. M.G. Jenkins, S.T. Gonczy, E. Lara-Curzio, N.E. Ashbaugh, and L. Zawada, ASTM pp. 158-175 (1997).

Wang, H.Y.; Luthra, K.; unpublished data.

Wiederhorn, S.M.; French, J.D.; Luecke, W.E.; "A Comparison of Fracture Mechanism Maps with the Larson-Miller Method of Predicting Life-time," *Ceram. Eng. Sci. Proc.*, **16** [5] 691-98 (1995).

Xia, Z.C.; Hutchinson, J.W.; Evans, A.G.; Budiansky, B.; "On Large Scale Sliding in Fiber-Reinforced Composites," *J. Mech. Phys. Solids*, **42** [7] 1139-58 (1994).

Yun, H.M.; DiCarlo, J. A.; "Time/Temperature Dependent Tensile Strength of SiC and Al₂O₃-Based Fibers," pp. 17-26 in Ceramic Transactions, vol. 74, Advances in Ceramic-Matrix Composites III. Edited by N.P. Bansal and J.P. Singh. American Ceramic Society, Westerville, OH, 1996.

Yun, H.M.; DiCarlo, J.A.; unpublished data.

Zawada, L.P.; Lee, S.S.; "The Effect of Hold Times on the Fatigue Behavior of an Oxide/Oxide Ceramic Matrix Composite," Thermal and Mechanical Test Methods and Behavior of Continuous-Fiber Ceramic Composites, ASTM STP 1309, eds. M. G. Jenkins et al., American Society for Testing and Materials, pp. 69-101 (1997).

Zhou, S.J.; Curtin, W.A.; "Failure of Fiber Composites: A Lattice Green Function Model," *Acta Metall. Mater* **43** [8] 3093-3104 (1995).

Ziola, S.M.; Gorman, M.R.; "Transverse Cracking and Longitudinal Splitting in Graphite/Epoxy Tensile Coupons as Determined by Acoustic Emission," *J. Acoustic Emission*, **8** [3] 51-60 (1989).

Zok, F.W.; Spearing, S.M.; "Matrix Crack Spacing in Brittle Matrix Composites," *Acta Metall. Mater.* **40** [8] 2033-2043 (1992).

REPORT DOCUMENTATION PAGE			Form Approved OMB No. 0704-0188	
Public reporting burden for this collection of information is estimated to average 1 hour per response, including the time for reviewing instructions, searching existing data sources, gathering and maintaining the data needed, and completing and reviewing the collection of information. Send comments regarding this burden estimate or any other aspect of this collection of information, including suggestions for reducing this burden, to Washington Headquarters Services, Directorate for Information Operations and Reports, 1215 Jefferson Davis Highway, Suite 1204, Arlington, VA 22202-4302, and to the Office of Management and Budget, Paperwork Reduction Project (0704-0188), Washington, DC 20503.				
1. AGENCY USE ONLY (Leave blank)	2. REPORT DATE April 2000	3. REPORT TYPE AND DATES COVERED Final Contractor Report		
4. TITLE AND SUBTITLE Intermediate Temperature Stress Rupture of Woven SiC Fiber, BN Interphase, SiC Matrix Composites in Air		5. FUNDING NUMBERS WU-714-04-30-00 NCC3-404		
6. AUTHOR(S) Gregory N. Morscher				
7. PERFORMING ORGANIZATION NAME(S) AND ADDRESS(ES) Case Western Reserve Cleveland, Ohio 44106		8. PERFORMING ORGANIZATION REPORT NUMBER E-12171		
9. SPONSORING/MONITORING AGENCY NAME(S) AND ADDRESS(ES) National Aeronautics and Space Administration John H. Glenn Research Center at Lewis Field Cleveland, Ohio 44135-3191		10. SPONSORING/MONITORING AGENCY REPORT NUMBER NASA CR-2000-209927		
11. SUPPLEMENTARY NOTES Project Manager, Stanley Levine, Materials Division, NASA Glenn Research Center, organization code 5130, (216) 433-3276.				
12a. DISTRIBUTION/AVAILABILITY STATEMENT Unclassified - Unlimited Subject Category: 27 This publication is available from the NASA Center for Aerospace Information, (301) 621-0390.			12b. DISTRIBUTION CODE Distribution: Nonstandard	
13. ABSTRACT (Maximum 200 words) Tensile stress-rupture experiments were performed on woven Hi-Nicalon reinforced SiC matrix composites with BN interphases in air. Modal acoustic emission (AE) was used to monitor the damage accumulation in the composites during the tests and microstructural analysis was performed to determine the amount of matrix cracking that occurred for each sample. Fiber fractography was also performed for individual fiber failures at the specimen fracture surface to determine the strengths at which fibers failed. The rupture strengths were significantly worse than what would have been expected from the inherent degradation of the fibers themselves when subjected to similar rupture conditions. At higher applied stresses the rate of rupture was larger than at lower applied stresses. It was observed that the change in rupture rate corresponded to the onset of through-thickness cracking in the composites themselves. The primary cause of the severe degradation was the ease with which fibers would bond to one another at their closest separation distances, less than 100 nanometers, when exposed to the environment. The near fiber-to-fiber contact in the woven tows enabled premature fiber failure over large areas of matrix cracks due to the stress-concentrations created by fibers bonded to one another after one or a few fibers fail, i.e. the loss of global load sharing. Any improvement in fiber-to-fiber separation of this composite system should result in improved stress-rupture properties. A model was developed in order to predict the rupture life-time for these composites based on the probabilistic nature of individual fiber failure at temperature, the matrix cracking state during the rupture test, and the rate of oxidation into a matrix crack. Also incorporated into the model were estimates of the stress-concentration that would occur between the outer rim of fibers in a load-bearing bundle and the unbridged region of a matrix crack after Xia et al. For the lower stresses, this source of stress-concentration was the likely cause for initial fiber failure that would trigger catastrophic failure of the composite.				
14. SUBJECT TERMS Ceramic matrix composites; Acoustic emission; Stress-rupture			15. NUMBER OF PAGES 127	
			16. PRICE CODE A07	
17. SECURITY CLASSIFICATION OF REPORT Unclassified	18. SECURITY CLASSIFICATION OF THIS PAGE Unclassified	19. SECURITY CLASSIFICATION OF ABSTRACT Unclassified	20. LIMITATION OF ABSTRACT	

